JETP Letters, Vol. 78, No. 6, 2003, pp. 343–346. Translated from Pis'ma v Zhurnal Éksperimental'noĭ i Teoreticheskoĭ Fiziki, Vol. 78, No. 6, 2003, pp. 795–798.
Original Russian Text Copyright © 2003 by Saperstein, Tolokonnikov.

Modification of the Energy Functional for Nuclei Near the Nucleon Stability Boundary

É. E. Saperstein and S. V. Tolokonnikov*

Russian Research Centre Kurchatov Institute, pl. Kurchatova 1, Moscow, 123182 Russia

** e-mail: tolkn@mbslab.kiae.ru*

Received August 11, 2003

The effective energy functional for nuclei near the nucleon stability boundary is modified by taking into account that the functional parameters corresponding to interaction in the surface region depend on the neutron and proton chemical potentials μ_n and μ_p, respectively, in a nucleus. By the example of several long isotope chains, it is shown that the μ dependence of the effective interaction results in shifting the neutron stability boundary toward large $N - Z$ values. © *2003 MAIK "Nauka/Interperiodica".*

PACS numbers: 21.60.–n; 21.65.+j

Nuclei near the nucleon stability boundary have been intensively studied experimentally in the last two decades. Until recently, the analysis of their properties, as well as the calculation of the position of this boundary, was exclusively based on phenomenological approaches, in which the parameters were determined from experiments. The Hartree–Fock method with effective forces [1, 2], self-consistent theory of finite Fermi systems [3, 4], and the energy functional method [5] are among these approaches. All these approaches, particularly the last one, describe stable nuclei quite well. However, the use of the parameters fitted to the properties of stable nuclei seems to be questionable for nuclides far from the β stability valley.

As was recently pointed out in [6, 7], the energy dependence (more precisely, dependence on, respectively, the chemical potentials μ_n and μ_p of the neutrons and protons in the nucleus under consideration) of the surface parts of those components of effective NN interaction which form the central part of the self-consistent nuclear field is substantial for the determination of the nucleon stability boundary. It is easy to illustrate the origin of the effect by the example of the self-consistency condition for the mass operator Σ, single-particle Green's function $\mathcal{G}$ and effective pair interaction $\mathcal{U}$ in the theory of finite Fermi systems [8]. This condition has the symbolic form

$$\left(\frac{\partial}{\partial \mathbf{r}_1} + \frac{\partial}{\partial \mathbf{r}_2}\right)\Sigma(\varepsilon) = \int \frac{d\varepsilon'}{2\pi i}\mathcal{U}(\varepsilon, \varepsilon')\left(\frac{\partial}{\partial \mathbf{r}_1'} + \frac{\partial}{\partial \mathbf{r}_2'}\right)\mathcal{G}(\varepsilon'), \quad (1)$$

where only the substantial energy variables are explicitly indicated. As usual, the symbolic multiplication in Eq. (1) implies the integration with respect to coordinates and summation over the spin and isospin indices.

In [9], Eq. (1) for $\varepsilon = \mu$ was renormalized by the Landau method [10]. As a result, the block $\mathcal{U}$ is replaced by the effective amplitude $F(\mu, \mu)$ of the Landau–Migdal interaction. The simplest Hartree–Fock-like version of the renormalized equation

$$\frac{\partial U}{\partial \mathbf{r}} = \int F(\mathbf{r}, \mathbf{r}')\frac{\partial \rho}{\partial \mathbf{r}'}d\mathbf{r}' \quad (2)$$

relates the mean field U, Landau–Migdal amplitude F, and the density ρ to each other. In the approximation of zeroth harmonics, which are principal for the Landau–Migdal amplitude [11], the central mean field U is generated by the following part of F:

$$F(\mathbf{r}, \mathbf{r}') = C_0[f_0(\mathbf{r}) + f_0'(\mathbf{r})\boldsymbol{\tau}_1\boldsymbol{\tau}_2]\delta(\mathbf{r} - \mathbf{r}'), \quad (3)$$

where the normalization factor $C_0 = (dn/d\varepsilon_F)^{-1}$ is the inverse density of states on the Fermi surface. In stable nuclei, $\mu_n = \mu_p = \mu \simeq -8$ MeV can be taken. In this case, the isotopic symmetry and the relations $f_{nn} = f_{pp} = f + f'$ and $f_{np} = f_{pn} = f - f'$ following from it are valid with a high accuracy.

The strong coordinate dependence of the scalar–isoscalar amplitude f_0 is of fundamental importance for the effect under discussion. Migdal [11] was the first to suggest for this amplitude in the theory of finite Fermi systems the following simplest interpolation from the internal value f^{in} to the external value f^{ex} with the linear density dependence:

$$f_0(\mathbf{r}) = f^{ex} + (f^{in} - f^{ex})\frac{\rho(\mathbf{r})}{\rho_0}, \quad (4)$$

where $\rho_0 = \rho(r = 0)$. It turned out that the external constant corresponds to strong attraction ($f^{ex} \simeq -3$) and

exceeds f^{in} in the absolute value by an order of magnitude. The effective forces used in [1–5] correspond to a more complex density dependence. However, $|f^{\text{ex}}|$ considerably exceeds $|f^{\text{in}}|$ for each of these forces. A coordinate dependence similar to Eq. (4) is also substantial for the scalar–isoscalar amplitude $f_0'(\mathbf{r})$ [12, 13], but the difference between the internal f'^{in} and external f'^{ex} constants is not too drastic.

As was shown in [14], the external constants f^{ex} and f'^{ex} (and corresponding spin amplitudes) can be expressed in terms of the off-shell T matrix of free NN scattering for negative total energy $E = 2\mu$. In the limit $r, r' \longrightarrow \infty$, $F \longrightarrow T\,(E = 2\mu)$. More precisely, the components of the Landau–Migdal amplitude are expressed in terms of the combinations of T matrices with isospins 0 and 1. This asymptotically exact relation is rapidly reached to provide the external Landau–Migdal constants close to the known empirical values. This equality is obviously approximate, because there are several different sets of these constants. The chemical potentials μ_n and μ_p are markedly different for nuclei near the stability boundary. In particular, μ_n is zero at the neutron stability boundary, while the absolute value of μ_p exceeds the value for stable nuclei. As a result, the isotopic symmetry is broken, and the above asymptotic relation for the Landau–Migdal amplitude takes the form

$$f_{nn}^{\text{ex}} = \frac{1}{C_0}T(E = 2\mu_n), \tag{5}$$

$$f_{pp}^{\text{ex}} = \frac{1}{C_0}T(E = 2\mu_p), \tag{6}$$

$$f_{np}^{\text{ex}} = f_{pn}^{\text{ex}} = \frac{1}{C_0}T(E = \mu_n + \mu_p). \tag{7}$$

Obviously, relations (5) and (6) involve the T matrix for the isospin $I = 1$, while relation (7) includes a combination of $T^{I=1}$ and $T^{I=0}$. Since $T^{I=1}(E)$ dependence is resonant for small E values, the parameters f_{nn}^{ex} and f_{pp}^{ex} can widely differ near the stability boundary. In particular, the absolute value of f_{nn}^{ex} increases strongly near the neutron stability boundary, and this behavior must be taken into account.

In [6, 7], the effect under discussion was taken into account by modifying the quasiparticle Lagrangian method [9, 15]. This method is a variant of the self-consistent theory of finite Fermi systems, where the quasiparticle Lagrangian is used to include the energy dependence for the interaction between quasiparticles, while the Hartree–Fock method with effective forces is based on the Hamiltonian formalism. By an example of tin isotopes, it was shown that the neutron stability boundary is shifted toward large $N - Z$ values.

In this work, we modify, in a similar way, the energy functional method with pairing in the coordinate representation, which was proposed in [16] and developed in detail by Fayans *et al.* (see, e.g., [5, 17]). This method is known as most accurately reproducing the masses and, particularly, radii of stable spherical nuclei. Moreover, it has an advantage over the quasiparticle Lagrangian method and Hartree–Fock method in that it accurately includes pairing effects in the coordinate representation. This feature is particularly important for nuclei near the stability boundary, because of the vicinity of continuous spectrum. For this reason, it is interesting to test whether the predictions made in [6, 7] are valid in this case.

The central part

$$\mathscr{E}_{\text{int}} = \frac{C_0}{4}\left[a_+\rho_+^2\frac{1 - h_1^+\rho_+/(2\rho_0)}{1 + h_2^+\rho_+/(2\rho_0)} + a_-\rho_-^2\frac{1 - h_1^-\rho_+/(2\rho_0)}{1 + h_2^-\rho_+/(2\rho_0)}\right] \tag{8}$$

of the energy functional is significant in the problem under consideration. Here, $\rho_{+,-} = \rho_n \pm \rho_p$ and $a_{+,-}$ and $h_{1,2}^{+,-}$ are dimensionless parameters. The total energy functional [5, 17] includes, in addition to central part (8), gradient terms, pairing term, spin–orbit term, and other spin-dependent components. According to the well-known Landau formula, the scalar part of the Landau–Migdal amplitude is equal to the second variation of expression (8) with respect to the density. In this procedure, the asymptotic ("external") values of the amplitudes f, f' are, obviously, obtained from those terms of expression (8) which depend most slightly (quadratically) on the density. This part of the functional has the form

$$\mathscr{E}_{\text{ex}} = \frac{C_0}{4}[a_+\rho_+^2 + a_-p_-^2]. \tag{9}$$

The relations $f^{\text{ex}} = a_+/2$ and $f'^{\text{ex}} = a_-/2$ are obviously valid. Modification of the functional by taking into account both the dependence of external constants (4)–(6) on chemical potentials and the corresponding breaking of the isotopic symmetry, we arrive at the simple generalization of Eq. (9)

$$\tilde{\mathscr{E}}_{\text{ex}}^{\text{I}} = \frac{C_0}{2}[f_{nn}^{\text{ex}}(E = 2\mu_n)\rho_n^2 + f_{pp}^{\text{ex}}(E = 2\mu_p)\rho_p^2 + 2f_{np}^{\text{ex}}(E = \mu_n + \mu_p)\rho_n\rho_p]. \tag{10}$$

For clarity, we explicitly present two-particle energies entering into expressions (4)–(6) for the external constants. According to interpolation (4), a change of functional (9) to functional (10) with the use of Eqs. (5)–(7) changes not only the external amplitudes (f_{nn}^{ex}, etc.) but

also their internal analogues (f_{nn}^{in}, etc.), while differences ($f_{nn}^{\text{in}} - f_{nn}^{\text{ex}}$, etc.) remain unchanged. The modification

$$\tilde{\mathscr{E}}_{\text{ex}}^{\text{II}} = \tilde{\mathscr{E}}_{\text{ex}}^{\text{I}}(1 - \rho(\mathbf{r})/\rho_0) \qquad (11)$$

of Eq. (10) with changing only the external amplitudes seems to be more reasonable.

The simplest method of including the dependence of the energy-functional parameters on chemical potentials is the replacement of Eq. (9) by Eq. (10) or (11). However, in this case, a new fit of all functional parameters is necessary, because external constants obtained from Eqs. (5)–(7) for $\mu_n = \mu_p = \mu_0 = -8$ MeV differ from the empirical parameters [5, 17]. Indeed, the constants obtained from Eqs. (5)–(7) are equal to $f^{\text{ex}} = -2.62$ and $f'^{\text{ex}} = 1.47$, while the respective parameters in Eq. (8) are $a_+/2 = -3.21$ and $a_-/2 = 2.71$. The difference in isovector constants is most pronounced. The difference is particularly due to the fact that the functional proposed in [5, 17] includes, in addition to the terms of form (8), pure surface terms involving density gradients. The addition of these terms is equivalent to a change in the parameters f_{nn}^{ex} and f_{pp}^{ex}. To minimize changes for stable nuclei without variation in other parameters of the functional, we take into account the dependence of the scalar Landau–Migdal amplitudes on μ_n and μ_p by changing total functional (8) to

$$\tilde{\mathscr{E}}_{\text{int}} = \mathscr{E}_{\text{int}} + \delta\mathscr{E}_{\text{int}}, \qquad (12)$$

where

$$\delta\mathscr{E}_{\text{int}} = \tilde{\mathscr{E}}_{\text{ex}}^{\text{I, II}}(\mu_n, \mu_p) - \tilde{\mathscr{E}}_{\text{ex}}^{\text{I, II}}(\mu_0, \mu_0). \qquad (13)$$

Obviously, the term $\delta\mathscr{E}_{\text{int}}$ is zero for $\mu_n = \mu_p = \mu_0$. Although it is difficult to *a priori* select variant I or II, the second variant is intuitively preferable. However, calculations were carried out for both models. All terms of the functional that are additional to Eq. (8), particularly its pairing part, were taken in the form given in [5, 17]. The same is true for the calculation procedure.

Figure 1 shows the neutron chemical potentials of a long chain of tin isotopes. Calculations for variants I and II are compared with the experimental data for $|\mu_n| = -S_{2n}$, where S_{2n} is the separation energy of two neutrons. Calculation [5] with the standard energy functional and the calculation made in [6], where the μ dependence of the Landau–Migdal amplitude was included by modifying the quasiparticle Lagrangian model, are also shown. The result of calculations made in [1–4] using other traditional approaches for the nuclei far from the β stability valley are close to the results obtained in [5]. In any case, all calculations predict a neutron stability boundary near the mass number $A = 176$, corresponding to the magic neutron number

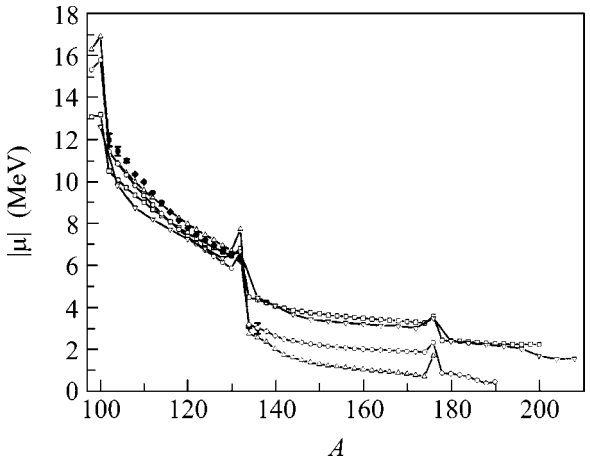

Fig. 1. Chemical potentials for even Sn isotopes. Lines with □, ○, △, and ▽ correspond to variants I, II, functional from [5], and quasiparticle Lagrangian method [6], respectively. Solid circles are experimental data taken from [18].

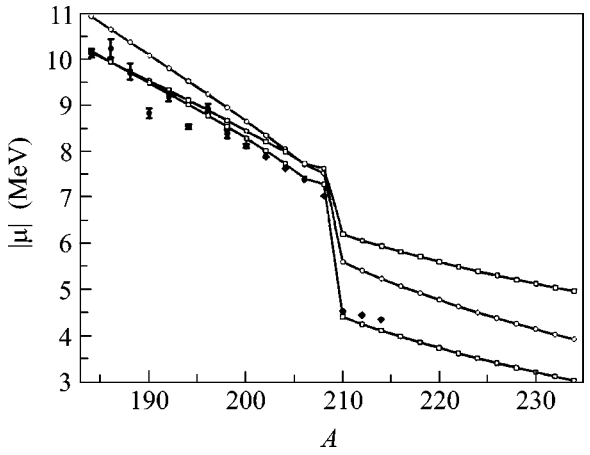

Fig. 2. The same as in Fig. 1, but for Pb isotopes.

$N = 126$. As is seen, the inclusion of the effect under consideration in our calculation, as in [6], strongly shifts the stability boundary. In the more realistic variant II, the μ effect is weaker but also allows overcoming the magic gap for $N = 126$.

Figures 2 and 3 show similar results for lead and calcium isotopes, respectively. These results are qualitatively similar to the results for tin; i.e., the μ effect is considerable and weaker for variant II.

Of course, this calculation cannot be treated as a numerical prediction. The point is that energy functional (8) and, particularly, identification of its coefficients with the invariant terms of the Landau–Migdal amplitude are directly associated with the Landau quasiparticle concept. In turn, this concept is based on the assumption that the mass operator $\Sigma(\varepsilon)$, as well as the

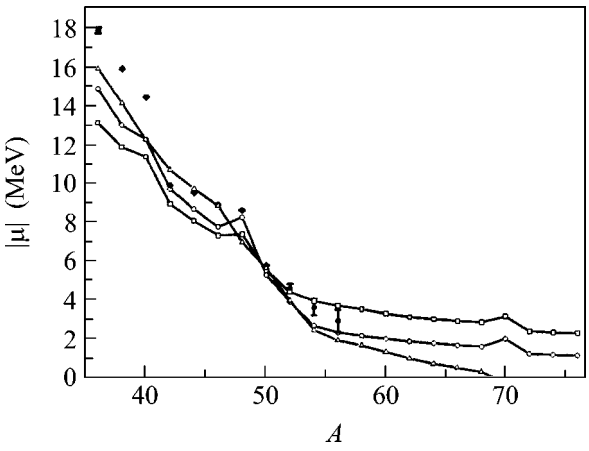

Fig. 3. The same as in Fig. 1, but for Ca isotopes.

corresponding effective interaction of fermions, has no singularities near $\varepsilon = \mu$. As a function of the total energy $E = 2\varepsilon$, the free T matrix determining interaction between quasiparticles near the surface has a singularity (virtual pole) near zero in the isovector channel. Because of proximity to this singularity, the neutron mean field becomes deeper and nuclei with low $|\mu_n|$ values become more stable. In the limit $\mu_n \longrightarrow 0$, the neutron mean field calculated in the proposed scheme can infinitely increase, and the scheme becomes inapplicable. Estimates show that the improvement of the scheme with a more correct inclusion of the ε dependence in Eq. (1) must weaken the effect under consideration. However, the enhancement of two-neutron interaction at the surface for low $|\mu_n|$ values, which was pointed out in [6, 7], as well as the necessity of including this effect as the neutron stability boundary is approached, is confirmed by this calculation and, in our opinion, is definite.

This work was supported by the Ministry of Industry and Science of the Russian Federation, project no. NSh 1885.2003.2.

REFERENCES

1. J. Dobaczewski, H. Flocard, and J. Treiner, Nucl. Phys. A **422**, 103 (1984).
2. J. Dobaczewski, W. Nazarewicz, T. R. Werner, *et al.*, Phys. Rev. C **53**, 2809 (1996).
3. M. V. Zverev and É. E. Sapershteĭn, Yad. Fiz. **39**, 1390 (1984) [Sov. J. Nucl. Phys. **39**, 878 (1984)].
4. M. V. Zverev and É. E. Sapershteĭn, Yad. Fiz. **42**, 1082 (1985) [Sov. J. Nucl. Phys. **42**, 683 (1985)].
5. S. A. Fayans, S. V. Tolokonnikov, E. L. Trykov, and D. Zawischa, Nucl. Phys. A **676**, 49 (2000).
6. M. Baldo, U. Lombardo, E. E. Saperstein, and M. V. Zverev, Phys. Lett. B **533**, 17 (2002).
7. M. Baldo, U. Lombardo, É. E. Sapershteĭn, and M. V. Zverev, Yad. Fiz. **66**, 257 (2003) [Phys. At. Nucl. **66**, 233 (2003)].
8. S. A. Fayans and V. A. Khodel', Pis'ma Zh. Éksp. Teor. Fiz. **17**, 633 (1973) [JETP Lett. **17**, 444 (1973)].
9. V. A. Khodel and E. E. Saperstein, Phys. Rep. **92**, 183 (1982).
10. L. D. Landau, Zh. Éksp. Teor. Fiz. **35**, 97 (1958) [Sov. Phys. JETP **8**, 70 (1958)].
11. A. B. Migdal, *Theory of Finite Fermi Systems and Applications to Atomic Nuclei* (Nauka, Moscow, 1965; Interscience, New York, 1967).
12. S. A. Fayans and D. Zawischa, Phys. Lett. B **363**, 12 (1995).
13. S. A. Fayans and D. Zawischa, Phys. Lett. B **383**, 19 (1996).
14. M. Baldo, U. Lombardo, E. E. Saperstein, and M. V. Zverev, Phys. Lett. B **421**, 8 (1998).
15. É. E. Sapershteĭn and V. A. Khodel', Zh. Éksp. Teor. Fiz. **81**, 22 (1981) [Sov. Phys. JETP **54**, 12 (1981)].
16. A. V. Smirnov, S. V. Tolokonnikov, and S. A. Fayans, Yad. Fiz. **48**, 1661 (1988) [Sov. J. Nucl. Phys. **48**, 995 (1988)].
17. S. A. Fayans, Pis'ma Zh. Éksp. Teor. Fiz. **68**, 161 (1998) [JETP Lett. **68**, 169 (1998)].
18. G. Audi and A. H. Wapstra, Nucl. Phys. A **565**, 66 (1993).

Translated by R. Tyapaev

JETP Letters, Vol. 78, No. 6, 2003, pp. 347–348. Translated from Pis'ma v Zhurnal Éksperimental'noĭ i Teoreticheskoĭ Fiziki, Vol. 78, No. 6, 2003, pp. 799–800.
Original Russian Text Copyright © 2003 by Alekseev, Bergman, Volkov, Goverdovskiĭ, Goncharenko, Perekrestenko, Samylin, Trufanov, Fursov.

Observation of Deep Subbarrier Resonances in ^{232}Th Fission

A. A. Alekseev[1], A. A. Bergman[1], A. N. Volkov[1], A. A. Goverdovskiĭ[2], O. N. Goncharenko[1, *], A. D. Perekrestenko[1], B. F. Samylin[2], A. M. Trufanov[2], and B. I. Fursov[2]

[1] *Institute for Nuclear Research, Russian Academy of Sciences, pr. Shestidesyatiletiya Oktyabrya 7a, Moscow, 117312 Russia*
** e-mail: oleggonchar@hotmail.com*
[2] *Institute of Physics and Power Engineering, pl. Bondarenko 1, Obninsk, Kaluga region, 249033 Russia*
Received August 14, 2003

Pronounced subbarrier ^{232}Th fission induced by resonance neutrons was observed. © *2003 MAIK "Nauka/Interperiodica".*

PACS numbers: 25.85.Ec

Thorium fission has attracted attention for more than five decades in view of the problem of self-consistent description of its properties, primarily, resonance effects near the top of the potential fission barrier. The probability of the process was measured with high energy resolution in the region of so-called beta vibration resonances excited by fast neutrons with energies E_n = 1.5–2.2 MeV. Based on these measurements, the existence of octupole hyperdeformed states in heavy nuclei, as well as the splitting of the outer barrier hump, can be hypothesized [1]. However, further observations of low-lying fission resonances (E_n = 0.8–1 MeV) [2] showed that the general pattern is much more complex. Indeed, the parameters of the so-called second and third barrier wells turned out to be virtually inconsistent with each other. In turn, this fact shows that the adequacy of the available theoretical concepts of the actinide cold fission on the whole and, in particular, of the arisen thorium anomaly is doubtful. Therefore, further experiments for gaining additional information are of current interest.

Study of deep subbarrier fission in the capture of resonance neutrons (E_n < 1 keV) by thorium nuclei is quite important. The cross section for the process is expected to be very small, about 1 μb [3]. The fission cross sections for impurity nuclei, such as ^{235}U that are inevitably present in any samples are equal to hundreds of barn. This circumstance imposes stringent requirements on a neutron beam and on the purity of irradiated targets.

The experiment was carried out on the SVZ-100 lead slowing-down 100-t high-transmission spectrometer at the Institute for Nuclear Research (INR), Russian Academy of Sciences. The extremely high flux density of resonance neutrons on the target position (~10^9 n/cm^2 s), energy selection of neutrons according to deceleration in lead, and targets from superpure materials (^{235}U admixture in ^{232}Th did not exceed 10^{-9}) provided the observation of effects reported below.

When interacting with a lead target in the SVZ-100 [4], a pulsed proton beam from the INR accelerator generates a pulsed neutron flux. We used the proton beam with an energy of 209 MeV, a pulse duration of 1–2 μs, and a pulse repetition frequency of 50 Hz. In this case, the intensity of the neutron source is equal to ~10^{13}–10^{14} n/s, which corresponds to the flux density 10^9–10^{10} n/cm^2 s of above-thermal neutrons in a moderator. The source is situated in the massive 100-t moderator made of superpure (99.99%) lead with measurement channels. The moderator is a 3.3 × 1.8 × 1.7-m elongated lead prism with a target constructed from lead blocks with a mass of about 1 t and displaced from the center. The measured resolution of the setup is equal to 30–31% for energies below 1 keV and to 28.5% for energies about 10 eV, which is the best resolution among the existing slowing-down spectrometers and is close to the theoretical limit (~26%). Since the measurement channels were far from the target, the background from γ rays and fast neutrons induced by a proton pulse was removed. A channel, where measurements were carried out, was placed near the prism center at a distance of 90 cm from the target. This arrangement provided the maximum neutron-flux intensities for energies below 10 keV and minimum flux-density gradients.

Fast ionization chambers, whose cathodes were covered with ^{232}Th (130 μg) and ^{235}U oxides, were used as fragment detectors. Test measurements showed that the fission detection efficiency is equal to 98%.

Figure 1 shows the measured results. A pronounced resonance structure of subbarrier ^{232}Th fission is observed almost over the entire neutron energy range studied. We emphasize that the subbarrier fission is particularly intense in the energy range E_n ~ 40 eV, which, as is known, contains a group of weak resonances corresponding to the neutron radiative capture, which competes with fission [5]. One can assume that a state or group of states responsible for the observed reso-

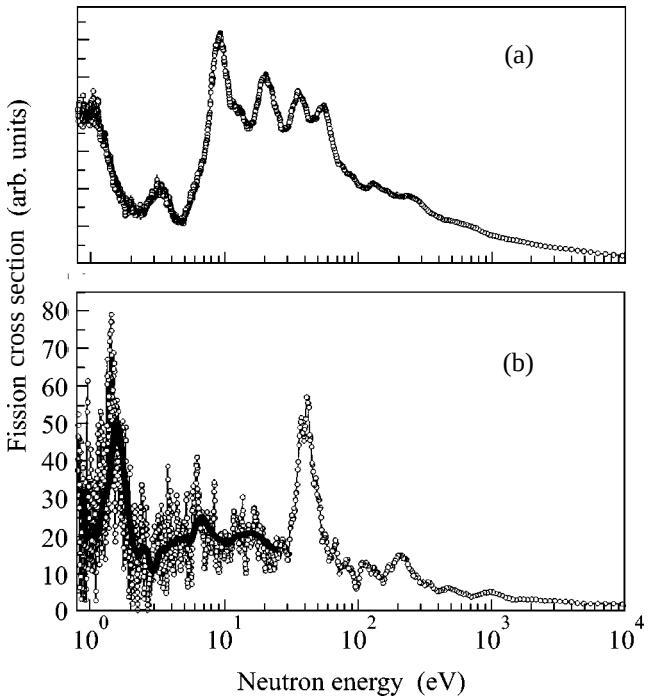

Fig. 1. Cross section for neutron-induced fission of (a) ^{235}U and (b) ^{232}Th nuclei vs. the neutron energy. The thick solid line below 25 eV is the least squares approximation of the spectrum.

nance is formed in the second well of the thorium fission barrier. This circumstance considerably increases the barrier penetrability. We call attention to the following implicit reason for this assumption. The width of the observed resonance structure slightly exceeds 27%, which, as was mentioned above, is close to the limiting resolution of the spectrometer. One real resonance, whose natural width must be equal to about 0.2%, is likely to effectively contribute to the pattern [1]. The amplitude of this resonance is easily estimated at about 0.4 mb. This is an enormous value for thorium. As is seen in Fig. 1, there is no correlation between the data for the ^{232}Th and ^{235}U samples. Therefore, the pattern observed in the ^{232}Th spectrum cannot be assigned to the ^{235}U admixture. The direct observation of the fission ^{232}Th resonances is important and provides information about the structure of this nucleus.

We emphasize that the high density of neutrons from SVZ-100 over the entire resonance energy range allows very important observations. In particular, the resonance structure detected in ^{232}Th subbarrier fission determines the investigation direction on high-resolution setups such as the *n*_TOF neutron source [6] at CERN, where similar experiments are planned in fall 2003.

We are grateful to the Administration of the Institute for Nuclear Research, Russian Academy of Sciences, for interest in this work, to Accelerator and Experimental Divisions for a successful run in May 2003, and to O.V. Karavichev and V.N. Marin for created fast electronics that facilitated observation of the results.

REFERENCES

1. S. Bornholm and J. E. Lynn, Rev. Mod. Phys. **52**, 725 (1980).
2. J. W. Behrens and J. C. Browne, Phys. Lett. B **69B**, 278 (1977).
3. Y. Nakagome *et al.*, Phys. Rev. C **43**, 1824 (1991).
4. A. A. Alexeev, A. A. Bergman, A. N. Volkov, *et al.*, in *Proceedings of IX International Seminar on Interaction on Neutrons with Nuclei, Dubna, Russia, 2001*, p. 11.
5. *Neutron Cross Sections*, BNL-325 (1965).
6. U. Abbondanno *et al.*, Technical Report CERN INTC 2000-018 (2000).

Translated by R. Tyapaev

JETP Letters, Vol. 78, No. 6, 2003, pp. 349–351. From Pis'ma v Zhurnal Éksperimental'noĭ i Teoreticheskoĭ Fiziki, Vol. 78, No. 6, 2003, pp. 801–803.
Original English Text Copyright © 2003 by Nefediev.

Comment on the Proper QCD String Dynamics in a Heavy–Light System¶

A. V. Nefediev

Institute of Theoretical and Experimental Physics, Moscow, 117218 Russia

e-mail: nefediev@heron.itep.ru

Received July 9, 2003

The string correction to the interquark interaction at large distances is derived using the field theory approach to a heavy–light quark–antiquark system in the modified Fock–Schwinger gauge. © *2003 MAIK "Nauka/Interperiodica".*

PACS numbers: 12.38.Aw; 12.39.Ki

Quantum chromodynamics at large distances is believed to be a string theory with the effective extended object—the QCD string—formed by nonperturbative gluons, which play an important role in hadronic phenomenology. It was demonstrated in a number of approaches that an account of the proper dynamics of the QCD string strongly affects hadronic spectra and is necessary to explain the correct Regge trajectory slopes [1–3], to resolve puzzles with the identification of new states [4], and so on. At large interquark distances, these dynamics can be encoded in the so-called string correction [2, 5], well known in the theory of the straight-line Nambu–Goto string with the tension σ and with massive quarks at the ends. The Lagrangian of this system is

$$L = -M\sqrt{\dot{x}_1^2} - m\sqrt{\dot{x}_2^2} - \sigma\int_0^1 d\beta\sqrt{(\dot{w}w')^2 - \dot{w}^2 w'^2}, \qquad (1)$$
$$w_\mu(t,\beta) = \beta x_{1\mu}(t) + (1-\beta)x_{2\mu}(t),$$

which leads to the center-of-mass. Hamiltonian, at large interquark distances $r = |\mathbf{x}_1 - \mathbf{x}_2|$, for $M \gg m$ [2],

$$H \approx M + m + \frac{\mathbf{p}^2}{2m} + \sigma r - \frac{\sigma\hat{L}^2}{6m^2 r} + \ldots, \qquad (2)$$

where, for the sake of convenience, we synchronize the quark times, $x_{10} = x_{20} \equiv x_0$, and fix the reparametrization invariance of the Lagrangian (1) by the laboratory frame condition $t = x_0$. The nonperturbative spin–orbit interaction comes from the area law for the Wilson loop [6],

$$V_{so} = -\boldsymbol{\sigma}\mathbf{L}/4m^2 r, \qquad (3)$$

and should be added to the Hamiltonian (2). The expansion in Eq. (2) is valid for $m \gg \sqrt{\sigma}$. Perturbative Coulomb interaction, as well as extra spin-dependent terms due to the latter, can be taken into account, and the resulting model appears rather successful in describing hadronic spectra (see, for example, [7], where the Hamiltonian (2) supplied by the perturbative interaction, but without the string correction, was used). A more sophisticated approach based on einbein field formalism [8] is also well known in the literature [2]. This method possesses several advantages as compared to the Hamiltonian (2) since, in this case, the corresponding Hamiltonian is given in terms of the effective dynamically generated quark masses μ's, given by the extremal values of the corresponding einbeins [9]. For light quarks, such a dynamical mass appears of order of the interaction scale, $\mu \sim \sqrt{\sigma}$, that is, much larger than the current quark mass—the latter can even be put to zero.

Recently, another approach to heavy–light systems was suggested, based on the Schwinger–Dyson series for a light quark in the presence of a static antiquark [10, 11]. Namely, the Schwinger–Dyson equation, in Euclidean spacetime,

$$(-i\hat{\partial}_x - im)S(x,y) - i\int d^4 z M(x,z)S(z,y) = \delta^{(4)}(x-y), \qquad (4)$$

was derived in the modified Fock–Schwinger gauge [12],

$$A_4(x_4, \mathbf{0}) = 0, \quad \mathbf{x}\mathbf{A}(x_4, \mathbf{x}) = 0, \qquad (5)$$

where the self-energy part $M(x, z)$ and the light-quark Green's function (also playing the role of the $q\bar{Q}$

¶ This article was submitted by the author in English.

Green's function) are given by [10]

$$-iM(x,z) = K_{\mu\nu}(x,z)\gamma_\mu S(x,z)\gamma_\nu,$$
$$S(x,y) = \frac{1}{N_C}\langle\psi^\beta(x)\psi^+_\beta(y)\rangle. \quad (6)$$

The interaction kernel $K_{\mu\nu}$ can be expressed in terms of the irreducible field strength correlator $\langle F^a_{\mu\nu}(x)F^b_{\lambda\rho}(y)\rangle$ [13],

$$\langle F^a_{\mu\nu}(x)F^b_{\lambda\rho}(y)\rangle = \delta^{ab}\frac{2N_C}{N_C^2-1} \times D(x_0-y_0,|\mathbf{x}-\mathbf{y}|)(\delta_{\mu\lambda}\delta_{\nu\rho}-\delta_{\mu\rho}\delta_{\nu\lambda})+\Delta^{(1)}, \quad (7)$$

where the second term $\Delta^{(1)}$ is a full derivative and does not contribute to confinement. As we are interested in the long-range force, we consider only the term proportional to $D(x-y)$ in (7) which, in contrast to $\Delta^{(1)}$, contributes to the area law with the string tension

$$\sigma = 2\int_0^\infty d\tau\int_0^\infty d\lambda D(\tau,\lambda). \quad (8)$$

Finally, for the kernel $K_{\mu\nu}$ in the gauge (5), one has ($\tau = x_4 - y_4$) [10, 11]:

$$K_{44}(\tau,\mathbf{x},\mathbf{y}) = (\mathbf{xy})\int_0^1 d\alpha\int_0^1 d\beta D(\tau,|\alpha\mathbf{x}-\beta\mathbf{y}|),$$
$$K_{i4}(\tau,\mathbf{x},\mathbf{y}) = K_{4i}(\tau,\mathbf{x},\mathbf{y}) = 0,$$
$$K_{ik}(\tau,\mathbf{x},\mathbf{y}) = ((\mathbf{xy})\delta_{ik}-y_ix_k)\int_0^1\alpha d\alpha\int_0^1\beta d\beta D(\tau,|\alpha\mathbf{x}-\beta\mathbf{y}|). \quad (9)$$

Using a consequent expansion of Eq. (4) for a large quark mass m ($m \gg \sqrt{\sigma}$ and $mT_g \gg 1$ [11, 14], where T_g is the gluonic correlation length), one can derive the interquark interaction, which is in agreement with the Eichten–Feinberg–Gromes results [15, 16]. Then, applying the Foldy–Wounthuysen (FW) transformation to the resulting interaction, it is easy to derive a Hamiltonian of the heavy–light system, at $r \gg T_g$, in the form [11, 14]:

$$H_{FW} = M + m + \frac{\mathbf{p}^2}{2m} + \sigma r - \frac{\boldsymbol{\sigma}\mathbf{L}}{4m^2 r} + \ldots, \quad (10)$$

where the ellipsis denotes terms $O(\sigma r/mT_g)$ suppressed in the limit $mT_g \gg 1$ [14, 17].

The Hamiltonian (10) coincides with the Hamiltonian of the quantum-mechanical quark–antiquark system connected by the Nambu–Goto string supplied by the nonperturbative spin-dependent interaction given by Eqs. (2), (3). In the meantime, an important ingredient mentioned above—the string correction—is still missing in the formula (10). The aim of the present paper is to resolve this inconsistency and, therefore, to complete matching of the two approaches: one, based on the quantum-mechanical string model, and the other, following from the field theoretical treatment of the heavy–light quark–antiquark system.

Following the path integral ideology, we consider the trajectory of the quark, $\mathbf{r}(t)$, such that the two consequent positions of the latter are $\mathbf{x} = \mathbf{r}(t_1)$ and $\mathbf{y} = \mathbf{r}(t_2)$. Therefore, for close t_1 and t_2, one can use the expansion

$$\mathbf{y} = \mathbf{r}(t_2) = \mathbf{r}(t_1+\tau) \approx \mathbf{r}(t_1) + \dot{\mathbf{r}}(t_1)\tau = \mathbf{x} + \frac{\mathbf{p}}{m}\tau, \quad (11)$$

where $\mathbf{p}$ is the momentum of the quark. Due to the rotational invariance, the function D from Eq. (7) actually depends on a certain combination of its arguments, $D(\tau,\lambda) = D(\tau^2+\lambda^2)$. In our case, $\tau = t_2 - t_1$ and $\lambda = |\alpha\mathbf{x} - \beta\mathbf{y}|$, so that, with the help of the expansion (11), one easily finds

$$\tau^2+\lambda^2 = \tau^2 + \left[(\alpha-\beta)\mathbf{r} + \alpha\tau\frac{\mathbf{p}}{m}\right]^2 = \left[1+\frac{\alpha^2p^2}{m^2}\right](\tau-\tau_0)^2 + \frac{(\alpha-\beta)^2}{1+\frac{\alpha^2p^2}{m^2}}\left[r^2+\alpha^2\frac{L^2}{m^2}\right], \quad (12)$$

where $\mathbf{r} \equiv \mathbf{x}$, $\mathbf{L}$ is the angular momentum, $\mathbf{L} = [\mathbf{r}\times\mathbf{p}]$, and the constant $\tau_0 = \alpha(\beta-\alpha)(\mathbf{rp})/m(1+\alpha^2p^2/m^2)$ can be excluded using an appropriate shift of the time variable τ, so we omit it below.

The confining spin-independent interaction, at large interquark distances and in the limit $mT_g \gg 1$, is given by the formula [10, 11, 14]:

$$V_{\rm conf}(r) = \gamma_\mu\frac{1+\gamma_0}{2}\gamma_\nu\int_0^\infty d\tau K_{\mu\nu}(\tau,\mathbf{x},\mathbf{y})|_{\mathbf{y}\to\mathbf{x}}. \quad (13)$$

Using the relations (9), one can easily calculate that

$$\int_0^\infty d\tau K_{00}(\tau,\mathbf{x},\mathbf{y})|_{\mathbf{y}\to\mathbf{x}} = r^2\int_0^\infty d\tau\int_0^1 d\alpha\int_0^1 d\beta \times D\left(\tau\sqrt{1+\frac{\alpha^2p^2}{m^2}}, (\alpha-\beta)\sqrt{\frac{r^2+\frac{\alpha^2L^2}{m^2}}{1+\frac{\alpha^2p^2}{m^2}}}\right) \quad (14)$$
$$\underset{r\gg T_g}{\approx} r\left(2\int_0^\infty d\tau'\int_0^\infty d\lambda D(\tau',\lambda)\right)$$

$$\times \int_0^1 \frac{d\alpha}{\sqrt{1+\frac{\alpha^2 L^2}{m^2 r^2}}} \approx \sigma r - \frac{\sigma L^2}{6m^2 r},$$

and, similarly,

$$\int_0^\infty d\tau K_{ik}(\tau, \mathbf{x}, \mathbf{y})|_{\mathbf{y}\to\mathbf{x}} \approx (\delta_{ik} - n_i n_k)\left(\frac{1}{3}\sigma r - \frac{\sigma L^2}{10m^2 r}\right), \quad (15)$$

where the definition of the string tension (8) was used, as well as the case $n = 0$ of the general formula

$$\int_0^1 d\alpha \int_0^1 d\beta f(\alpha, \beta)(\alpha-\beta)^n D(\tau, |\alpha-\beta|a)$$
$$\underset{a\gg 1}{\approx} \frac{2}{a^{n+1}} \int_0^\infty d\lambda D(\tau, \lambda) \int_0^1 d\alpha f(\alpha, \alpha),$$

which holds for an arbitrary function $f(\alpha, \beta)$, provided $f(\alpha, \alpha) \neq 0$.

Therefore, the confining interaction (13), in the limit $mT_g \gg 1$, becomes

$$V_{\text{conf}}(r) = \left(\frac{5}{6} + \frac{1}{6}\gamma_0\right)\sigma r - \left(\frac{11}{60} - \frac{1}{60}\gamma_0\right)\frac{\sigma L^2}{m^2 r}, \quad (16)$$

or, after the FW rotation, this corresponds to the confining potential

$$V_{\text{conf}}^{\text{FW}}(r) = \sigma r - \frac{\sigma L^2}{6m^2 r}. \quad (17)$$

The first term of the interaction (16), (17) was obtained in [10, 11, 14, 17], whereas the second term was missing due to the immediate substitution of $\mathbf{y} = \mathbf{x}$ in the formula (13), which holds up to the order $1/m$ but, as demonstrated above, fails in the next order, $1/m^2$. As a result, the string correction was lost, although a more accurate expansion of the correlator D, performed in this paper, allows one to reproduce the confining potential, including its part due to the proper string dynamics. Therefore, we conclude that, indeed, the string correction accompanies the linear confinement potential of whatever approach is used to derive the latter, provided the string picture of confinement is adopted. Meanwhile, the suggested approach is rather inconvenient for further investigations of the confining interaction in the approach of the Schwinger–Dyson nonlinear equation (4). On the other hand, a promising step is made in the paper [18] where a contour gauge is introduced which generalizes the gauge condition (5) for the case of an arbitrary trajectory of the heavy particle. Formally, Eqs. (4), (6) remain valid, though the kernel of the interaction becomes contour-dependent. In the meantime, the form of the contour depends on the heavy particle trajectory, that is, it is defined dynamically, and the problem becomes self-consistent. Consequent expansion of the aforementioned contour around the straight-line form may provide a way to systematically account for the $(1/m)^n$ and $(1/M)^n$ corrections in this approach.

The author would like to acknowledge Yu.A. Simonov and Yu.S. Kalashnikova for providing useful discussions.

This work is supported by INTAS, via grants OPEN no. 2000-110 and YSF no. 2002-49, by the grant no. NS-1774.2003.2, and by the Federal Program of the Russian Ministry of Industry, Science, and Technology (grant no. 40.052.1.1.1112).

REFERENCES

1. M. G. Olsson, Phys. Rev. D **55**, 5479 (1997).
2. A. Yu. Dubin, A. B. Kaidalov, and Yu. A. Simonov, Phys. Lett. B **323**, 41 (1994); Phys. Lett. B **343**, 310 (1995).
3. V. L. Morgunov, A. V. Nefediev, and Yu. A. Simonov, Phys. Lett. B **459**, 653 (1999).
4. A. V. Nefediev and Yu. S. Kalashnikova, Phys. Lett. B **492**, 91 (2000); Phys. Lett. B **530**, 117 (2002); A. V. Nefediev, Yu. S. Kalashnikova, and Yu. A. Simonov, Phys. Rev. D **64**, 014037 (2001).
5. J. Merlin and J. Paton, J. Phys. G **11**, 439 (1985).
6. Yu. A. Simonov, Nucl. Phys. B **324**, 67 (1989).
7. D. R. Stanley and D. Robson, Phys. Lett. B **45B**, 235 (1980); P. Cea, G. Nardulli, and G. Preparata, Z. Phys. C **16**, 135 (1982); Phys. Lett. B **115B**, 310 (1982); J. Carlson, J. B. Kogut, and V. R. Pandharipande, Phys. Rev. D **27**, 233 (1983); N. Isgur and S. Godfrey, Phys. Rev. D **32**, 189 (1985).
8. L. Brink, P. Di Vecchia, and P. Howe, Nucl. Phys. B **118**, 76 (1977); Yu. S. Kalashnikova and A. V. Nefediev, Yad. Fiz. **60**, 1529 (1997) [Phys. At. Nucl. **60**, 1389 (1997)].
9. Yu. A. Simonov, Nucl. Phys. B **307**, 512 (1988); Yu. A. Simonov and J. A. Tjon, Ann. Phys. (N.Y.) **228**, 1 (1993).
10. Yu. A. Simonov, Yad. Fiz. **60**, 2252 (1997) [Phys. At. Nucl. **60**, 2069 (1997)].
11. N. Brambilla and A. Vairo, Phys. Lett. B **407**, 167 (1997); P. Bicudo, N. Brambilla, E. Ribeiro, and A. Vairo, Phys. Lett. B **442**, 349 (1998).
12. I. I. Balitsky, Nucl. Phys. B **254**, 166 (1985).
13. H. G. Dosch and Yu. A. Simonov, Phys. Lett. B **205**, 339 (1988).
14. Yu. S. Kalashnikova and A. V. Nefediev, Phys. Lett. B **414**, 149 (1997).
15. E. Eichten and F. L. Feinberg, Phys. Rev. D **23**, 2724 (1981).
16. D. Gromes, Z. Phys. C **26**, 401 (1984).
17. Yu. A. Simonov and J. A. Tjon, Phys. Rev. D **62**, 094511 (2000).
18. V. I. Shevchenko and Yu. A. Simonov, Phys. Lett. B **437**, 146 (1998).

JETP Letters, Vol. 78, No. 6, 2003, pp. 352–357. Translated from Pis'ma v Zhurnal Éksperimental'noĭ i Teoreticheskoĭ Fiziki, Vol. 78, No. 6, 2003, pp. 804–809.
Original Russian Text Copyright © 2003 by Bogdanov, Krivitsky, Kulik.

Statistical Reconstruction of the Quantum States of Three-Level Optical Systems

Yu. I. Bogdanov[1, *], L. A. Krivitsky[2, **], and S. P. Kulik[2, **]

[1] *Russian Control System Agency, "Angstrem," Moscow, 124460 Russia*

**e-mail: bogdan@angstrem.ru*

[2] *Moscow State University, Vorob'evy gory, Moscow, 119992 Russia*

***e-mail: postmast@qopt.phys.msu.su*

Received July 24, 2003

The procedure of measurement followed by the reconstruction of the quantum state of a three-level optical system is implemented for a frequency- and spatially degenerate two-photon field. The method of statistical estimation of the quantum state from a solution to the likelihood equation and the analysis of the statistical properties of the obtained estimators is developed. Using the root method of estimating quantum states, the initial two-photon (qutrit) wave function is reconstructed from the measured fourth-order field moments. © *2003 MAIK "Nauka/Interperiodica".*

PACS numbers: 03.67.Hk; 42.50.Dv; 42.25.Ja

Introduction. The ability of measuring quantum states is no doubt of fundamental interest because it provides a tool for the analysis of basic concepts of quantum theory, such as the fundamentally statistical character of its predictions, the superposition principle, the Bohr's complementarity principle, etc. By the measurement of quantum state we will imply a two-step *measurement and computation procedure*. The first step is a genuine measurement consisting of a set of operations under the representatives of a quantum statistical (pure or mixed) ensemble, as a result of which the experimenter acquires a set of frequencies with which particular events occur. The second step consists of the mathematical procedure of reconstructing the quantum state of an object using the combination of the obtained statistical data.

This work is devoted to the state reconstruction for optical three-level systems. Such states are obtained, e.g., in the polarization representation of a frequency- and spatially degenerate biphoton field [1]. The necessity of properly measuring the states of such systems is dictated by the applied problems. For example, increase in the key distribution security in quantum cryptography is associated with the increase in the dimensionality of Hilbert space for the states in use [2]; in this respect, certain hopes are pinned on the three-level systems (qutrits) [3, 4].

1. Biphotons as three-level systems. A biphoton field is a coherent mixture of the biphoton Fock's states $|1_{\mathbf{k}}, 1_{\mathbf{k}'}\rangle$ and the vacuum state $|\mathrm{vac}\rangle$ [5]:

$$|\Psi\rangle = |\mathrm{vac}\rangle + \frac{1}{2}\sum_{\mathbf{k},\mathbf{k}'} F_{\mathbf{k},\mathbf{k}'}|1_{\mathbf{k}}, 1_{\mathbf{k}'}\rangle, \qquad (1)$$

where the coefficients $F_{\mathbf{k},\mathbf{k}'}$ are called biphoton amplitudes [6], and $|1_{\mathbf{k}}, 1_{\mathbf{k}'}\rangle$ denotes the state with one (signal) photon in the $\mathbf{k} \equiv \mathbf{k}_s$ mode and one (idler) photon in the $\mathbf{k}' \equiv \mathbf{k}_i$ mode. We will consider the collinear and degenerate regimes, for which $\mathbf{k}_s \approx \mathbf{k}_i$, $\omega_s \approx \omega_i \approx \omega_p/2$, and $\omega_s + \omega_i = \omega_p$, where ω_p is the laser pump frequency. The method of producing, transforming, and measuring these states is described in detail in [7–10]. The initial state to be measured and reconstructed has the following form:

$$|\Psi\rangle = c_1|2, 0\rangle + c_2|1, 1\rangle + c_3|0, 2\rangle. \qquad (2)$$

Here, we use the representation of a biphoton-light polarized state (1) in the Fock's basis. For example, the notation $|2, 0\rangle$ indicates that both photons are in the horizontal (H) polarization mode, while no photons are present in the vertical (V) mode.

The state of a three-level system in quantum information theory has come to be known as *qutrit*. The properties of biphoton qutrits and their mapping on the Poincaré sphere were described in [8].

The idea of producing and measuring state (2) was put forward in [9, 10]. The system for detecting biphoton qutrits includes a beam splitter and a pair of detectors whose outputs are connected to the photocount coincidence circuit (figure). An event is considered detected if a pulse appears at the output of the coincidence circuit. In approximately one half of all cases, one of the photons (signal, by convention) of a biphoton is led to one of the detectors, while another (idler photon) is led to the second detector. In the remaining cases, both photons occur in the same beam-splitter arm, and these events are not detected because they do

not coincide. The polarization transformations are accomplished using a quarter-wave plate and a polarizing prism placed ahead of each detector. It was shown in [9, 10] that, if the qutrit state is unknown, one is forced to make nine moment-projection measurements to reconstruct the initial mixed (in the general case) state. These moments have the form [11]:

$$R_{s,i} \sim \langle (b'_s)^\dagger (b'_i)^\dagger b'_s b'_i \rangle = R(\chi_s, \gamma_s, \chi_i, \gamma_i), \qquad (3)$$

where $(b'_j)^\dagger$ and b'_j are, respectively, the photon creation and annihilation operators for the signal and idler modes $j = s, i$ after the transformation and χ_j and γ_j are the setting parameters (plate and polarizing-prism orientation angles, respectively).

The time (as a rule, 100 ms) it took for measuring each of the nine moments was one of the experimental parameters. Each measurement was made in triplicate and consisted in the taking of 700–800 averages, whereupon the scheme was reset; namely, the χ_j and γ_j angles were set according to the tomographic protocol (Table 1), after which the cycle was repeated. Thus, the mean photocount coincidence rates $R_{1, 2, \ldots, 9}$ were the output data of the measuring setup. To compare the results of reconstruction with the parameters of the input states, which should be known with a high accuracy, we used the following method of state preparation. The biphotons were produced in the process of collinear frequency-degenerate spontaneous parametric down conversion in lithium iodate crystal. The polarization of both created photons was vertical; i.e., the state

$$|c'\rangle = |0, 2\rangle \qquad (4)$$

was generated. Next, this state was transformed using a quartz plate with a given thickness $h = 824 \pm 1$ μm. Upon turning this plate in the plane perpendicular to the incident biphoton beam (the plate optical axis lied in this plane), the state (2) transformed according to the rule

$$|c\rangle_{\text{in}} = G|c'\rangle, \qquad (5)$$

where the matrix

$$G = \begin{pmatrix} t^2 & \sqrt{2}tr & r^2 \\ -\sqrt{2}tr^* & |t|^2 - |r|^2 & \sqrt{2}t^*r \\ r^{*2} & -\sqrt{2}t^*r^* & t^{*2} \end{pmatrix} \qquad (6)$$

describes the action of a plate with effective transmittance t and reflectance r, $t = \cos\delta + i\sin\delta\cos 2\alpha$ and $r = i\sin\delta\sin 2\alpha$. In this expression, the optical thickness $\delta = \pi|n_o - n_e|h/\lambda$ and α is the angle between the plate optical axis and the vertical. For crystalline quartz, $|n_o - n_e| = 0.0089$ at the wavelength $\lambda = 702$ nm, whence it follows that $\delta = 32.82 \pm 0.04$.

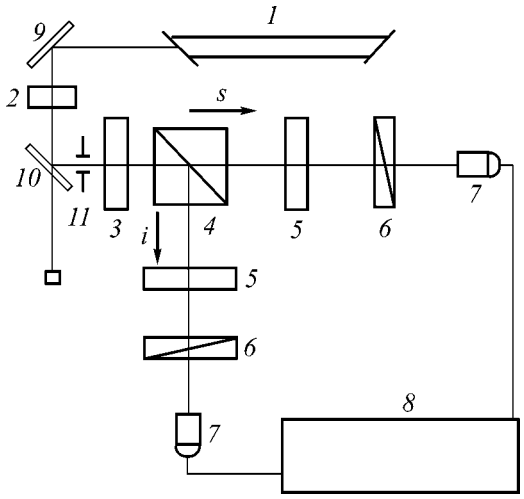

Schematic of experimental setup. (*1*) Argon laser (λ_p = 351 nm); (*2*) lithium iodate crystal in which the biphotons with a central wavelength of 702 nm are generated; (*3*) quartz phase plate with parameters (α, $\delta = 32.82$); (*4*) beam splitter directing (conventionally) the signal photons to the right and the idler photons downward; (*5*) quarter-wave plates ($\chi_{s,i}$, $\delta = \pi/4$); (*6*) polarizing prisms ($\gamma_{s,i}$); (*7*) detectors operating in the photon counting mode; (*8*) double coincidence circuit; (*9*) deflecting mirror; (*10*) mirror transmitting the radiation at a wavelength of 351 nm and reflecting at a wavelength of 702 nm; and (*11*) mode selection iris.

So, unitary transformation (5) gave a set of states $c_{\text{in}}(\alpha)$ that was fed into the measuring unit of the setup. The purpose of this work was to reproduce these states.

2. Statistical reconstruction of biphoton states from the results of mutually complementary measurements. When analyzing the experimental data, we will use the so-called root method of estimating quantum states [12–14]. This method is designed specially for the analysis of mutually complementary measurements.[1] The advantages of this method consist in the possibility of reconstructing states in a high-dimensional Hilbert space and posing fundamental limits on the accuracy of reconstruction of an unknown quantum state. The use of asymptotically efficient algorithms allow one to achieve a reconstruction accuracy close to its fundamental limit.

The set of mutually complementary measurements of a biphoton-field state was implemented in accordance with the tomographic protocol presented in Table 1. The event-generation intensity R_ν, $\nu = 1, 2, \ldots, 9$, is the main quantity accessible for the measurement. The moments R_ν are the coincidence frequencies measured in frequency units (Hz). The number of events occurring in any given time interval obeys the Poisson distribution. Therefore, the quantities R_ν specify the intensities of the corresponding mutually complementary Poisson processes and serve as estimators of the Poisson parameters λ_ν (see below).

[1] In the sense of the Bohr's complementarity principle.

Table 1

ν	Parameters of experimental setup				Amplitude of the process
	χ_s	γ_s	χ_i	γ_i	M_ν
1	0°	−90°	0°	−90°	$\frac{c_1}{\sqrt{2}}$
2	0°	−90°	0°	0°	$\frac{c_2}{2}$
3	0°	0°	0°	0°	$\frac{c_3}{\sqrt{2}}$
4	45°	0°	0°	0°	$\frac{1}{2\sqrt{2}}c_2 - \frac{i}{2}c_3$
5	45°	−45°	0°	0°	$\frac{1}{2\sqrt{2}}c_2 - \frac{1}{2}c_3$
6	45°	−45°	0°	−90°	$\frac{1}{2}c_1 - \frac{1}{2\sqrt{2}}c_2$
7	45°	0°	0°	−90°	$\frac{1}{2}c_1 - \frac{i}{2\sqrt{2}}c_2$
8	−45°	–22.5°	45°	–22.5°	$\frac{1}{2\sqrt{2}}c_1 + \frac{i}{2\sqrt{2}}c_3$
9	−45°	−45°	45°	45°	$\frac{1}{2\sqrt{2}}c_1 - \frac{1}{2\sqrt{2}}c_3$

For each process, the event-generation intensity can be represented as a squared absolute value of the corresponding amplitude:

$$R_\nu = M_\nu^* M_\nu, \quad \nu = 1, 2, \ldots, 9. \tag{7}$$

Although the amplitudes of the processes cannot be measured directly, they are of the greatest interest as quantities describing the fundamental relationships of quantum physics. From the superposition principle, it follows that the amplitudes are linearly related to the state-vector components. It is the purpose of quantum tomography to reconstruct the amplitudes and state vectors that are hidden from direct observation.

The linear transformation of the state vector c into the amplitude of the process M is described by a certain matrix X, which can easily be obtained from Table 1:

$$X = \begin{pmatrix} 1/\sqrt{2} & 0 & 0 \\ 0 & 1/2 & 0 \\ 0 & 0 & 1/\sqrt{2} \\ 0 & 1/(2\sqrt{2}) & -i/2 \\ 0 & 1/(2\sqrt{2}) & -1/2 \\ 1/2 & -1/(2\sqrt{2}) & 0 \\ 1/2 & -i/(2\sqrt{2}) & 0 \\ 1/(2\sqrt{2}) & 0 & i/(2\sqrt{2}) \\ 1/(2\sqrt{2}) & 0 & -1/(2\sqrt{2}) \end{pmatrix}. \tag{8}$$

Then the set of all nine amplitudes of the processes can be expressed by a single matrix equation

$$Xc = M. \tag{9}$$

We call matrix X the instrumental matrix of a set of mutually complementary measurements, by analogy with the conventional instrumental function. In statistical terms, Eq. (9) is the linear regression equation. A distinctive feature of the problem is that only the absolute value of the right-hand side of the equation is measured in the experiment. The estimate of the absolute value of the amplitude is given by the square root of the corresponding experimentally measured coincidence frequency:

$$|M_\nu|^{\exp} = \sqrt{k_\nu/t}, \tag{10}$$

where k_ν is the number of events detected in the νth process during exposure time t.

It is worth noting that, by the action of root-square procedure on a Poisson random value, one obtains the random variable with a uniform variance, i.e., at the variance stabilization [13, 15]. Note also that, since we deal not with event probabilities but with their frequencies or intensities, it is convenient to use nonnormalized state vectors. These vectors allow the coincidence counting rate (event-generation intensities) to be derived directly from the formulas given in Table 1, without introducing coefficients related to the biphoton generation rate, detector efficiencies, etc. The dimensionality of the vector state thus obtained is $1/\sqrt{\text{time}}$.

The final state vector obtained by the reconstruction procedure, nevertheless, will be normalized to unity.

Considering that the variances of different $|M_v|^{exp}$ are independent and identical, one can apply the standard least-squares estimator to Eq. (11) [16]:

$$\hat{c} = (X^+X)^{-1}X^+\hat{M}. \quad (11)$$

Contrary to the traditional least-squares method, the relation obtained cannot be used for explicit estimation of the state vector c, because it is to be solved by the iteration method. The absolute value of $\hat{M}$ is known from the experiment ($|\hat{M}_v| = |M_v|^{exp}$), and its phase is determined by the iteration procedure (it is assumed that the phase of vector Xc at the ith iteration step determines the phase of the vector $\hat{M}$ at the $(i + 1)$th step). It turns out that, in the Gaussian approximation for the Poisson's quantities, this least-squares estimator coincides with a more exact and rigorous maximum likelihood estimator considered below.

3. Maximum likelihood method. The likelihood function is defined by the product of Poisson probabilities:

$$L = \prod_i \frac{(\lambda_i t_i)^{k_i}}{k_i!} e^{-\lambda_i t_i}, \quad (12)$$

where k_i is the number of coincidences observed in the ith process during exposure time t_i, and λ_i ($i = 1, 2, \ldots, 9$) are the unknown theoretical event-generation intensities (photocurrent coincidences), whose estimation is the subject of this work.

The logarithmic likelihood (logarithm of the likelihood function) is, except for an insignificant constant,

$$\ln L = \sum_i (k_i \ln(\lambda_i t_i) - \lambda_i t_i). \quad (13)$$

We also introduce the matrices with elements defined by the following formulas:

$$I_{sj} = \sum_i t_i X_{is}^* X_{ij}, \quad (14)$$

$$J_{sj} = \sum_i \frac{k_i}{\lambda_i} X_{is}^* X_{ij}, \quad s, j = 1, 2, 3. \quad (15)$$

The matrix I is determined from the experimental protocol and, thus, is known *a priori* (before the experiment). It coincides with so-called Fisher information matrix (see below). On the contrary, the matrix J is determined by the experimental values of k_i and by the unknown event-generation intensities λ_i. In terms of these matrices, the condition for the extremum of function (13) can be written as

$$Ic = Jc, \quad (16)$$

whence it follows that

$$I^{-1}Jc = c. \quad (17)$$

We will call the latter relationship the likelihood equation. This is a nonlinear equation, because λ_i depends on the unknown state vector c. Because of the simple quasi-linear structure, this equation can easily be solved by the iteration method [12–14]. The operator $I^{-1}J$ can be called a quasi-identity operator. Note that it acts as the identical operator on only one vector in the Hilbert space, namely, on the vector corresponding to solution (17) and representing the maximum possible likelihood estimator for the state vector. The condition for existence of the matrix I^{-1} is a condition imposed on the initial experimental protocol.[2] The resulting set of equations automatically includes the normalization condition, which is written as

$$\sum_i k_i = \sum_i (\lambda_i t_i). \quad (18)$$

This condition implies that, for all processes, the total number of detected events is equal to the sum of the products of event detection rates into the exposure time.

The elements of Fisher information matrix are defined as the average products of the derivatives of the logarithmic likelihood function [12–14]

$$I_{sj} = \overline{\frac{\partial \ln L}{\partial c_j} \frac{\partial \ln L}{\partial c_s^*}}, \quad (19)$$

where $\ln L$ is given by Eq. (13). We will average in Eq. (19) on the assumption that the event detection obeys the Poisson law. Therefore,

$$I_{sj} = \sum_i \frac{t_i}{\lambda_i} \frac{\partial \lambda_i}{\partial c_j} \frac{\partial \lambda_i}{\partial c_s^*}. \quad (20)$$

After going, in accordance with Eq. (7), from the event-generation frequencies (intensities) to the amplitudes of the processes, the expression for the Fisher information matrix is greatly simplified and takes the form of Eq. (14).

If the exposure times for all processes are the same ($t = t_i = \text{const}$), then

$$I = t(X^+X). \quad (21)$$

Thus, the Fisher information matrix, in fact, is determined by the observation time for the statistical ensemble. In other words, time plays the role of the most fundamental measure of information.

[2] This theory is valid not only for an X matrix of the particular form (8) but also in the general case.

Table 2

No.	α angle, deg	Number of events $\sum_{\nu=1}^{9} k_\nu$	State vector		F	χ^2
			Theory c_1, c_2, c_3	Experiment c_1, c_2, c_3		
1	17.5	2012	0.3094, 0.6248 + 0.1921*i*, 0.5713 + 0.3880*i*	0.3549, 0.5620 + 0.2684*i*, 0.5467 + 0.4328*i*	0.9946	15.925*
2	22.5	1997	0.4702, 0.6649 + 0.2368*i*, 0.4105 + 0.3349*i*	0.4961, 0.6444 + 0.2486*i*, 0.4017 + 0.3399*i*	0.9990	3.6482
3	25	6119	0.5518, 0.6548 + 0.2566*i*, 0.3289 + 0.3045*i*	0.5234, 0.6637 + 0.2446*i*, 0.3687 + 0.2997*i*	0.9979	16.384*
4	27.5	1281	0.6310, 0.6248 + 0.2744*i*, 0.2497 + 0.2717*i*	0.6466, 0.6184 + 0.2897*i*, 0.2521 + 0.2281*i*	0.9976	7.4987
5	30	2245	0.7053, 0.5758 + 0.2901*i*, 0.1754 + 0.2368*i*	0.7266, 0.5890 + 0.1900*i*, 0.2224 + 0.1992*i*	0.9921	26.977*
6	32.5	2753	0.7724, 0.5094 + 0.3036*i*, 0.1083 + 0.2002*i*	0.7953, 0.5107 + 0.2519*i*, 0.1217 + 0.1685*i*	0.9967	11.239

4. Analysis of experimental data. The examples of reconstruction of the qutrit states by the maximum likelihood method are given in Table 2. In the next-to-last column, the values of the fidelity parameter F defined as

$$F = \langle c|\rho|c\rangle \xrightarrow{\text{pure state}} \left|\langle c_{\text{calc}}|c_{\text{exp}}\rangle\right|^2 \qquad (22)$$

and indicating, in our case, the measure of correspondence between the theoretical and experimental state vectors are presented. The asterisk (*) denotes the experimental χ^2 values that exceed the critical value 11.345 at a confidence level of 99%. For these experiments, one can state with a guarantee of 99% accuracy that the uncertainties in setting the measurement parameters and their instabilities are statistically significant. In other words, a comparison of the reconstruction results with the fundamental statistical level of accuracy can serve as a basis for some problems such as the setup adjustment, operation stability control, revelation of foreign interference in the system, etc. Thus, for a small sample size, statistical errors prevail, whereas for large sample sizes, the setting errors and the instability of protocol parameters dominate. In our case, the observation time was such that both these types of errors played a significant part. For some experiments, the χ^2 values were lower than the critical level, and for some other experiments, these values were higher than the critical level. The larger the sample size for which the setup operation errors and instabilities are as yet insignificant, the higher the quality of the experiment.[3] The process of quantum information accumulation is described by Eqs. (14) and (21); as the measurement time increases, the quantum states of the greater and greater number of ensemble representatives break and information about the object of interest progressively increases. Accordingly, the statistical error becomes more and more small. Therefore, only the errors of the first (statistical) type bear a fundamental quantum character. The errors of the second (setting error) type are, fundamentally, classical, because they are caused by the researcher's incomplete knowledge; i.e., a more exact information exists, in principle, but it is inaccessible to the experimenter.

The state-preparation procedure considered in Section 1 assumes that only pure states of the form (2) are fed into the measuring unit of the setup. The same conclusion can be drawn from the data analysis: a comparison of the results of reconstructing quantum state in the approximation of a pure ensemble with the results of the separation of a mixture into two components (so-called quasi-Bayes algorithm [14]) indicates that the estimator for a pure state vector is very close to the estimator for the major density-matrix component.

[3] The corresponding number of experiments can be called coherence volume.

Conclusions. The procedure of measuring the quantum state of a three-level optical system formed by a frequency- and spatially degenerate biphoton field has been considered in this work. The method of statistical estimation of the quantum state through solving the likelihood equation and examining the statistical properties of the resulting estimators has been developed. Based on the experimental data (fourth-order field moments) and the root method of estimating quantum states, the initial wave function has been reconstructed for biphoton qutrits. The inaccuracy in setting the measurement parameters are analyzed for the cases where their instability is statistically significant.

This work was supported in part by the Russian Foundation for Basic Research (project nos. 02-02-16843 and 03-02-16444) and INTAS (grant no. 2122-01).

REFERENCES

1. A. V. Burlakov and D. N. Klyshko, Pis'ma Zh. Éksp. Teor. Fiz. **69**, 795 (1999) [JETP Lett. **69**, 839 (1999)].
2. H. Bechmann-Pasquinucci and W. Tittel, Phys. Rev. A **61**, 062308 (2000).
3. H. Bechmann-Pasquinucci and A. Peres, Phys. Rev. Lett. **85**, 3313 (2000).
4. M. V. Chekhova, S. P. Kulik, G. A. Maslennikov, and A. A. Zhukov, quant-ph/0305115.
5. D. N. Klyshko, *Photons and Nonlinear Optics* (Nauka, Moscow, 1980), p. 256.
6. A. V. Belinsky and D. N. Klyshko, Laser Phys. **4**, 663 (1994).
7. A. V. Burlakov, M. V. Chekhova, D. N. Klyshko, *et al.*, Phys. Rev. A **60**, 4209 (1999).
8. A. V. Burlakov and M. V. Chekhova, Pis'ma Zh. Éksp. Teor. Fiz. **75**, 505 (2002) [JETP Lett. **75**, 432 (2002)].
9. A. V. Burlakov, L. A. Krivitskiĭ, S. P. Kulik, *et al.*, Opt. Spektrosk. **94**, 744 (2003) [Opt. Spectrosc. **94**, 684 (2003)].
10. L. A. Krivitskiĭ, S. P. Kulik, A. N. Penin, and M. V. Chekhova, Zh. Éksp. Teor. Fiz. **124** (4), 943 (2003) [JETP **97**, 846 (2003)].
11. D. N. Klyshko, Zh. Éksp. Teor. Fiz. **111**, 1955 (1997) [JETP **84**, 1065 (1997)].
12. Yu. I. Bogdanov, *Fundamental Problem of Statistical Data Analysis: Root Approach* (Mosk. Inst. Élektron. Tekh., Moscow, 2002); physics/0211109 (2002).
13. Yu. I. Bogdanov, Quantum Mechanical View of Mathematical Statistics, in *Progress in Quantum Physics Research* (Nova Science, New York, 2003); quant-ph/0303013 (2003).
14. Yu. I. Bogdanov, Root Estimator of Quantum States, in *Progress in Quantum Physics Research* (Nova Science, New York, 2003); quant-ph/0303014 (2003).
15. H. Cramer, *Mathematical Methods of Statistics* (Princeton Univ. Press, Princeton, N.J., 1946; Mir, Moscow, 1975).
16. M. G. Kendall and A. Stuart, *The Advanced Theory of Statistics*, 4th ed. (Griffin, London, 1977; Nauka, Moscow, 1973).
17. *Optical Materials for Infrared Engineering* (Mir, Moscow, 1965).

Translated by V. Sakun

JETP Letters, Vol. 78, No. 6, 2003, pp. 358–362. Translated from Pis'ma v Zhurnal Éksperimental'noĭ i Teoreticheskoĭ Fiziki, Vol. 78, No. 6, 2003, pp. 810–815.
Original Russian Text Copyright © 2003 by Vshivkov, Nikitin, Snytnikov.

Study of the Instabilities of Collisionless Systems on the Basis of Stochastic Trajectories

V. A. Vshivkov[1], S. A. Nikitin[2], and V. N. Snytnikov[3, *]

[1] *Institute of Computer Technologies, Siberian Division, Russian Academy of Sciences, Novosibirsk, 630090 Russia*

[2] *Budker Institute of Nuclear Physics, Siberian Division, Russian Academy of Sciences, Novosibirsk, 630090 Russia*

[3] *Novosibirsk State University, Novosibirsk, 630090 Russia*

**e-mail: snyt@catalysis.nsk.su*

Received May 28, 2003; in final form, August 11, 2003

We propose a practical method for distinguishing stochastic and regular subsystems in the entire set of particles for numerical modeling of the development of physical instabilities in collisionless systems with self-consistent fields. The method of subdividing the phase space into subsystems is based on the comparison of the results of two computational experiments with identical initial conditions but different realizations of rounding errors. An example of establishing the spatial and temporal domains of the development of collective instability and determining the instability increments is offered by a gravitating disk. *© 2003 MAIK "Nauka/Interperiodica".*

PACS numbers: 95.10.Ce; 04.40.-b

Collisionless gravitational and plasma systems can exhibit self-organization, in the course of which the system passes from the initial unstable state to a new state which is stable under given conditions. Investigations of the instability of such systems are performed, in particular, in terms of the equation of conservation of the phase volume (the Vlasov–Lioville equation) and the equation of long-range self-consistent field (the Poisson equation) [1]:

$$\frac{\partial f}{\partial t} + \mathbf{v}\nabla f + \mathbf{a}\frac{\partial f}{\partial \mathbf{v}} = 0,$$

$$\Delta\Phi = 4\pi G\rho.$$

This system of equations is usually numerically solved by particle techniques [2, 3] based on the calculation of self-consistent dynamics of a finite but very large number of particles. The particle trajectories are determined by a computational code even in cases of modeling self-organization and dynamical chaos. This situation differs from that of experiments under real conditions, where random perturbations additionally contribute to the dynamics. For this reason, calculations involved in the analysis of collective particle dynamics encounter a problem recognizing physical instabilities on the background of nonstationary stable solutions. Attempts to impose additional finite perturbations on the particle trajectories for checking their stability encounter questions concerning multiplicity of the solutions of initial equations and the dependence of solutions on the initial data.

This paper describes a new method intended for the investigation of instabilities. The proposed method neither involves additional perturbations, nor depends on the form of initial conditions, nor requires theoretical analysis of increments in a many-body system. This method distinguishes the elements of regular motions from stochastic and subdivides particles into regular and stochastic subsystems within the same computer realization of the process of instability development. In the course of computational experiments involving up to 10^9 more particles [4], our approach consists in the possibility and necessity of analyzing the dynamics of all particles. For the comparison, the number of stars in galaxies reaches 10^{10} and above.

According to the idea of the proposed method, a computer is considered as a physical experimental setup. In this setup, the phase coordinates of particles involve rounding errors in the form of physical fluctuations. The fluctuations are deterministically set by the computational code and the computer type in the form of a particular random sequence. For a regular stable trajectory, the accumulation of such errors is determined by a stable (in the computational sense) algorithm. These errors appear in the last, lowest decimal digits of the mantissa. The error magnitudes depend primarily on the number of operations, while particular values are still retained in the lowest digits. If the motion of a particle for some reason becomes unstable, the accumulation of rounding errors in the values of coordinates is determined by increments of instability development. For particles involved in the unstable motion, the algorithm transfers random rounding errors of the phase coordinates to the higher digits of the mantissa determining the main part of a value. By virtue of instability, the phase trajectories of particles acquire

0021-3640/03/7806-0358$24.00 © 2003 MAIK "Nauka/Interperiodica"

stochasticity. It is possible to separate the accumulated random parts of values and, hence, to distinguish stable regular and unstable stochastic trajectories by performing and comparing two identical calculations with different realizations of rounding errors. The stable trajectories of particles in the two calculations will coincide, whereas the unstable trajectories will exhibit recession (in configuration space as well). The rounding errors can be changed on a program level. However, most simple and physically clear calculations of this kind are performed using the same program with equal word lengths and identical initial data on computers with principally different processors (e.g., AMD vs. Intel or Intel vs. Alpha 21264). The results of calculations performed by different processors will coincide for problems of searching for stable solutions and will differ for simulations involving physical instability development.

For implementing the approach outlined above, it is necessary for a numerical model to satisfy certain requirements, such that physical instabilities will be distinguished from various numerical instabilities of algorithms deprived of any physical sense. First, a numerical model intended for studying physical instabilities has to meet the condition of approximation for the initial equations of mathematical physics. Second, the model must obey the condition of convergence for the solutions obtained on refined calculation grids. Third, the model should retain sensitivity to variation of the initial data. Fourth, the condition of stability of a numerical method in the linear approximation must be violated at least locally. Evidently, the above requirements differ from the conditions of approximation and stability of the Lax theorem [5], which are necessary for ensuring convergence of a numerical solution to the solution of the initial problem. The Lax theorem underlying the numerical methods of solution of many problems in mathematical physics and separating numerical instabilities from nonstationary solutions is inapplicable to the calculations of physical instabilities. This leads to the fifth requirement, according to which computational experiments involved in the investigation of instability in many-body systems must obey all the laws of conservation (for mass, momentum, moment momentum, and energy). From the standpoint of computational physics, violation of the laws of conservation in a collisionless method of coarse particles presents a serious problem [6]. An analysis of this problem allowed us to find approaches to the solution [7–9] based on the creation of codes meeting the aforementioned requirements [10].

As an example of self-organization, we have calculated the scenarios of instability development for a gravitating disk with the central body. A nonstationary process in this system is modeled in numerical experiments involving 10^7 or a greater number of particles. The problem is solved in a thin disk approximation [1], whereby the particles are characterized by polar coordinates and two velocity projections, without motion along the axis. The Poisson equation is solved in D space. The initial nonequilibrium condition corresponds to solid-state rotation with a power density profile. The distribution of particle velocities did not obey the Tumre stability criterion [1]. The variables were rendered dimensionless using a certain mass, the initial disk radium R, and the constant of gravitation. In these units, the initial mass of the central body is 0.4, the disk mass is 1.0 for particles and the same for the gas, the disk rotation speed is 1.0, and the velocity dispersion is 1.0. For a disk without central body, one turn would take 4.0 units of time. The spatial grid has $120 \times 256 \times 101$ cells with dimensions $0.075 \times (2\pi/256) \times 0.1$. The time step τ was selected so as not to exceed the average time required for the particles to travel through the calculation cell. This time is significantly smaller than 1/50 of the period of rotation about the central body. This condition is sufficient to avoid separatrix stochastization due to a discrete procedure of trajectory calculation [11]. The number of steps required for a particle on a stable trajectory to lose memory about the initial position as a result of rounding errors for an 8-byte value is estimated at 10^{19} [12]. The Jeans instability with respect to initial conditions must be manifested for a cold disk without central body during the first turn, which corresponds to 10^3 calculation steps.

The comparative calculations were performed on AMD and Intel processors using a program with 1.2×10^6 particles at an 8-byte length of values, and using a parallel program for MPI run on two Intel or Alpha 21264 processors. A pseudorandom number generator was incorporated into the program. The initial conditions were strictly identical. The results of self-organization proceeding from a nonequilibrium state are presented in Fig. 1 showing the particle number density at $T = 0$ (initial moment) and at $T = 7.5$. The gray scale gradation is logarithmic, with white differing from black by five orders of magnitude. The density distribution reveals dynamically stable filament-like structures with bent ends approaching a rapidly rotating compact disk surrounding the central body. In addition, the bottom right corner diagonal exhibits a stable soliton-like density wave formed as a result of interaction of several like waves appearing at earlier moments of time.

Figures 2 and 3 present the results of analysis of the regular (a) and stochastic (b) trajectories for the moments of $T = 2.5$ and 5.0. Square areas with a side length of $6R$ show the densities constructed for the corresponding subsystems of particles. Regular and stochastic motions are distinguished based on the criterion of trajectory recession for each jth particle by more than 0.1 of the cell size:

$$\left\|\mathbf{r}_j'(t) - \mathbf{r}_j''(t)\right\| \geq 0.1\min(h_r, h_\varphi).$$

As can be seen from Fig. 2, both regular and stochastic particles at $T = 2.5$ occupy the same region of the configuration space (in the disk plane). For the stochastic particles, Fig. 2 reveals the main spatial zone in which the trajectories become unstable. This zone is sur-

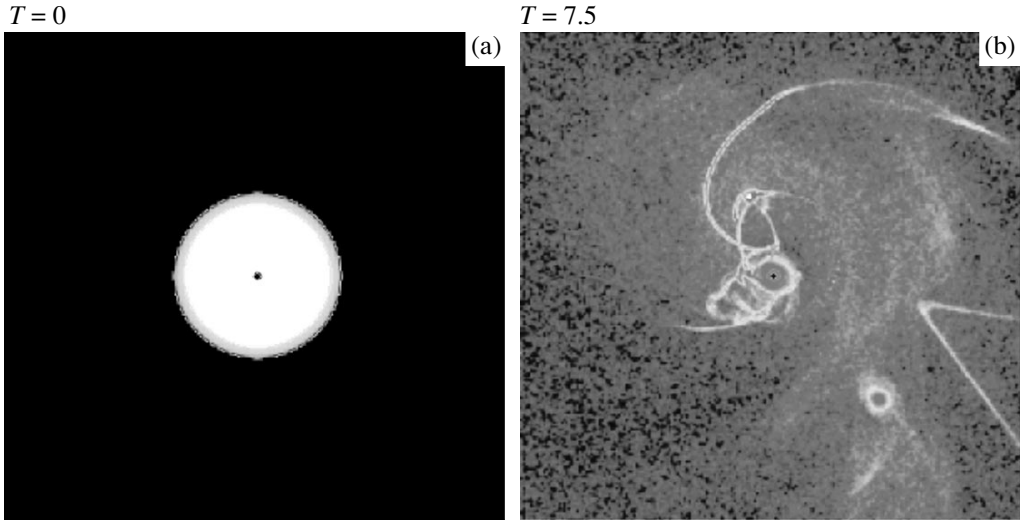

Fig. 1. Diagrams of (a) initial ($T = 0$) and (b) new ($T = 7.5$) particle density in the disk.

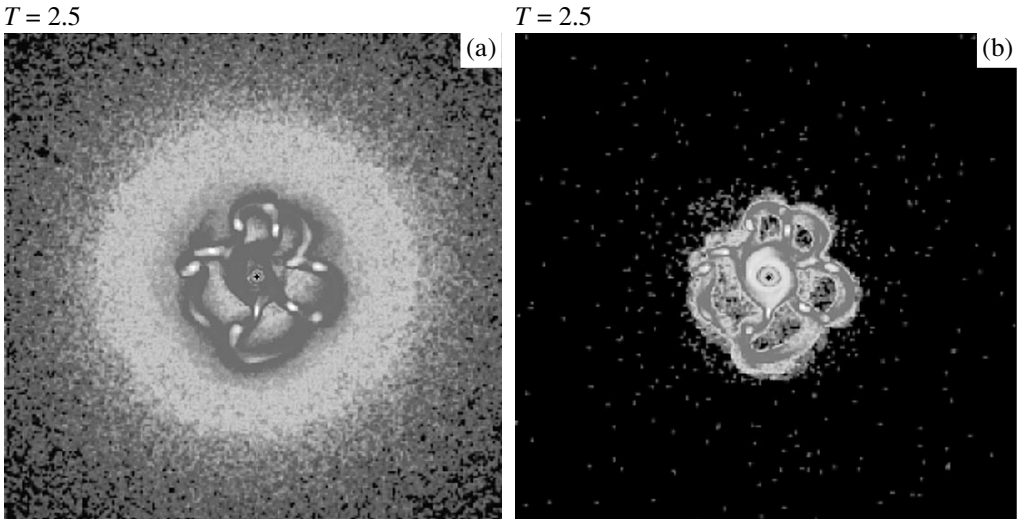

Fig. 2. Particle density distribution in the disk at $T = 2.5$: (a) regular particles; (b) stochastic particles.

rounded by "evaporated" particles. By the moment of $T = 5.0$ (Fig. 3), the influence of stochastic particles spreads over almost the whole density pattern. These particles form new stable soliton-like structures (Fig. 3b). Particles with the regular trajectories are retained on the periphery and in a narrow zone surrounding the central body (Fig. 3a). By the moment of $T = 7.5$ (Fig. 1b), there are almost no regular particles in the system.

Figure 4 illustrates the time variation of the absolute value of the difference between densities n' and n'' for the two calculations, summed over the entire region of calculation:

$$\Delta(t) = \int_S |n'(\mathbf{r}, t) - n''(\mathbf{r}, t)|\, dxdy.$$

As can be seen from this plot, the instability in the linear stage develops with an exponent of $\gamma \sim 9.57$ (with a characteristic time amounting to approximately 0.03 of the disk rotation time indicated above) up to a time of $T \approx 2.3$. The density fluctuations increase by nine orders in magnitude relative to the initial level, reaching 10^{-6}. After that, spreading of the trajectories of unstable particles begins, accompanied by accumulation of the density difference and by modification of the fields. Until $T \approx 3.1$, new particles are brought into stochastic motion and the regular particles pass to new trajectories. Subsequently (until $T \approx 6$), the system exhibits a nonlinear stage of instability saturation and the formation of a new solution. Beginning at approximately this time, the solutions begin to diverge, demonstrating the appearance of a new dynamical state (Fig. 1, $T = 7.5$).

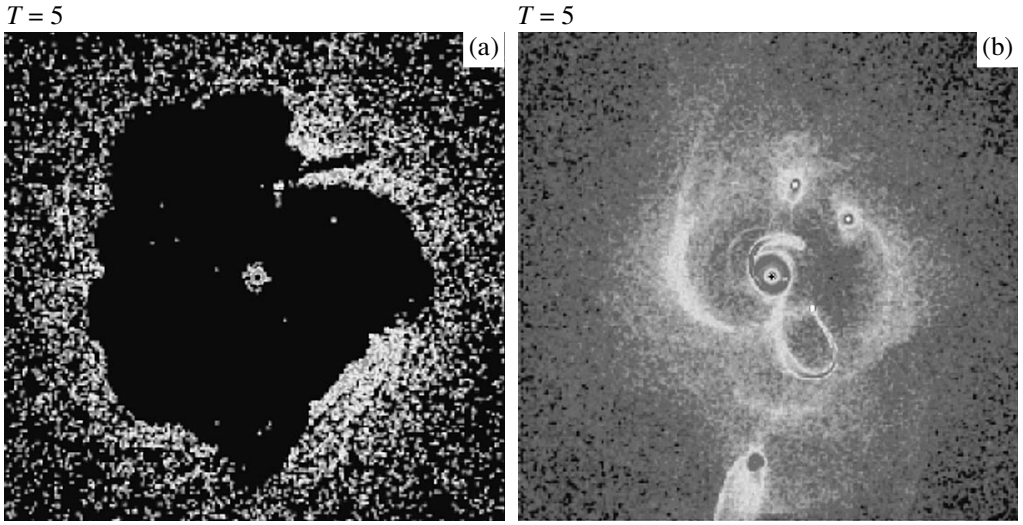

Fig. 3. Particle density distribution in the disk at $T = 5$: (a) regular particles; (b) stochastic particles.

The results of control calculations using the same processor (AMD) with various operational systems and a translator (UNIX + GNU Fortran and Windows 2000 + Watcom Fortran) showed the trajectories to be perfectly identical in all temporal stages, despite different computation speeds. Analogous identical results were obtained with various AMD processors (Duron, 800 MHz and Athlon, 1600 MHz). The results of calculations using a parallel variant of the program appeared as if corresponding to a new particle velocity distribution (that is, to different particle trajectories) realized by a qualitatively different computational algorithm. At the same time, a comparison of the results of calculations obtained using two Intel or Alpha 21264 processors showed a dynamical pattern that allowed particles involved in the regular and stochastic motions to be distinguished.

Summarizing the results of computational experiments, we may conclude that the possibility of dividing particles into regular and stochastic for the given program is determined by the processor. For the other algorithms, the properties of the compiler may also influence realizations of the rounding errors and provide a means of distinguishing the trajectories calculated using processors of the same type.

Numerous calculations using variable parameters showed that, in the course of instability development, deviations from the initial state as a result of random fluctuations exhibit exponential initial growth. The growth of deviations is accompanied by change of the self-consistent fields acting upon particles. Some particles pass from regular to stochastic trajectories. As the instability develops, the number of such particles increases. Thus, fluctuations (usually small) become enhanced to a nonequilibrium level. Among these, some are selected to form a new state in the stage of instability saturation. Collisionless damping and weak collisions decrease the remaining fluctuations to a thermodynamically equilibrium level of random noise in the new state. In the new established self-consistent field potential, particles occur in the regimes of either regular motion or a dynamic chaos.

For the computer calculations in the stage of a physical instability development, the random rounding errors significantly influence realizations of the particle trajectories. Outside the framework of the instability development in time and space, these errors are not manifested for a given numerical criterion. A physical instability is manifested through local accumulation of stochastic particles. Regions of the phase space containing such particles are essentially the zones of instability. Using a change in the density of stochastic particles (in our example, in projection of the phase space

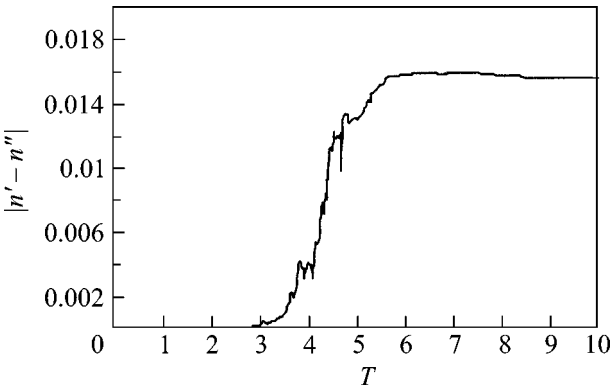

Fig. 4. Time variation of the total difference between particle densities in the two calculations.

onto the configuration space), it is possible to calculate a local value of the instability increment $\gamma(\mathbf{r}, t)$:

$$\sum_{i=t_0/\tau}^{i=t/\tau} [n_s(\mathbf{r}, t_0)\exp(\gamma(\mathbf{r})(t_i - t_0)) - n_s(\mathbf{r}, t_i)]^2 \longrightarrow \min.$$

The time during which the particles may become stochastic can be defined as the time of instability development. This time is determined in computational experiments by transfer of the coordinates and velocities from one computer to another, modeling the initial data for the given time, followed by the discrimination of stochastic particles. In this way, the stability of trajectories is established for real physical problems involving arbitrary numbers of particles.

Thus, we have propose a practical method for studying instabilities, based on the determination of recessing stochastic trajectories (RSTs). Using this method, it is possible to establish both spatial and temporal limits of instability and determine increments averaged over all particles and over separate spatial groups, including a single particle. It is also possible to determine average macroscopic functions of a given system at the instability onset time. This method allows the "conditions of transition to stochasticity" to be studied without limitations inherent in the well-known criteria formulated for the systems with two degrees of freedom [12]. Since the motion of particles in a self-consistent gravitational field of the central body with rotation coincides to within a transformation with the motion in electromagnetic fields [13], the proposed approach can be applied to the analysis of instabilities in electrodynamics as well. It would also be of interest to use this approach for the analysis of the hypothesis concerning the possible transient nature of spiral structures in galactic disks [14]. Here, it is important to establish whether the stellar spirals can appear in a fast sequence of particular evolutionary cycles, each including the development of instability followed by dissipation in the interstellar gas. Another important example is offered by a mechanism responsible for self-sustaining stellar disks of real galaxies occurring in a quasistationary equilibrium state with slow dynamical evolution [15]. In modeling substantially unstable structures such as protoplanet disks, the proposed method can help finding generalized parameters of the process of gas–dust bunch formation [16].

We are grateful to V.N. Parmon for support, to A.V. Snytnikov for the development of a parallel program version, and to E.A. Kuksheva for assistance in calculations and graphics. This work was supported by the Integration Project of the Siberian Division of the Russian Academy of Sciences (no. 148 of 2003), the Presidium of the Russian Academy of Sciences (program 2003, Part 4. "Nonstationary Processes in Astronomy" and Part 6.6. "Problems of the Earth's Biosphere Initiation and Evolution"), the Russian Foundation for Basic Research (project no. 02-01-00864), and the "Super Computer 2003" Project of the Siberian Division of the Russian Academy of Sciences.

REFERENCES

1. F. M. Fridman and V. L. Polyachenko, *Physics of Gravitating Systems* (Nauka, Moscow, 1976; Springer, New York, 1984).
2. R. Hockney and J. Eastwood, *Computer Simulation Using Particles* (McGraw-Hill, New York, 1984; Mir, Moscow, 1987).
3. Yu. N. Grigorjev, M. P. Fedoruk, and V. A. Vshivkov, *Numerical "Particle-in-Cell" Methods* (Nauka, Novosibirsk, 2000; VSP, Utrecht, 2002).
4. V. A. Vshivkov, É. A. Kuksheva, S. A. Nikitin, *et al.*, Avtometriya **39** (in press).
5. P. J. Roach, *Computational Fluid Dynamics* (Hermosa, Albuquerque, 1976; Mir, Moscow, 1980).
6. Yu. A. Berezin and V. A. Vshivkov, *Method of Particles in Dynamics of the Rarefied Plasma* (Nauka, Novosibirsk, 1980).
7. V. N. Snytnikov, Candidate's Dissertation in Physics and Mathematics (Novosibirsk, 1990).
8. V. A. Vshivkov, Doctoral Dissertation in Physics and Mathematics (Novosibirsk, 1996).
9. V. A. Vshivkov and V. N. Snytnikov, Zh. Vychisl. Mat. Mat. Fiz. **38**, 1877 (1998).
10. V. N. Snytnikov, V. N. Parmon, V. A. Vshivkov, *et al.*, Vychisl. Tekhnol. **7**, 72 (2002).
11. G. M. Zaslavskiĭ, R. Z. Sagdeev, D. A. Usikov, and A. A. Chernikov, *Weak Chaos and Quasi-Regular Structures* (Nauka, Moscow, 1991).
12. A. J. Lichtenberg and M. A. Lieberman, *Regular and Stochastic Motion* (Springer, New York, 1982; Mir, Moscow, 1984).
13. A. M. Fridman and N. N. Gor'kavyi, *Physics of Planetary Rings: Celestial Mechanics of Continuous Media* (Nauka, Moscow, 1994; Springer, New York, 1999).
14. J. A. Sellwood, Rutgers Astrophysics Preprint No. 256 (1999).
15. A. V. Khoperskov, A. V. Zasov, and N. V. Tyurina, Astron. Vest. (in press).
16. V. N. Snytnikov, G. I. Dudnikova, J. T. Gleaves, *et al.*, Adv. Space Res. **30**, 1461 (2002).

Translated by P. Pozdeev

JETP Letters, Vol. 78, No. 6, 2003, pp. 363–368. Translated from Pis'ma v Zhurnal Éksperimental'noĭ i Teoreticheskoĭ Fiziki, Vol. 78, No. 6, 2003, pp. 816–821.
Original Russian Text Copyright © 2003 by Goryaev, Urnov, Bertschinger, Marchuk, Kunze, Dubau.

On $K\beta$ Radiation of Ar^{16+} Ions in Coronal Plasma

F. F. Goryaev*, A. M. Urnov*, G. Bertschinger, A. G. Marchuk**, H.- J. Kunze***, and J. Dubau******

**Lebedev Physical Institute, Russian Academy of Sciences, Leninskiĭ pr. 53, Moscow, 117924 Russia*

***Institut fur Plasmaphysik, Forschungszentrum, Julich GmbH, Association Euratom-KFA, 52425 Julich, Germany*

****Institut fur Experimentalphysik V, Ruhr-Universitat Bochum, 44780 Bochum, Germany*

***** 176 CNRS, Observatoire de Paris, 92190 Meudon, Paris, France*

Received June 11, 2003; in final form, August 13, 2003

The measured and calculated data obtained in this and earlier works for the intensity ratio $G_3 = I[K\beta_2]/I[K\beta_1]$ of the intercombination and resonance $K\beta$ lines corresponding to the $1s3p^3P_1 \longrightarrow 1s^2{}^1S_0$ ($K\beta_2$) and $1s3p^1P_1 \longrightarrow 1s^2{}^1S_0$ ($K\beta_1$) transitions in the coronal plasma spectrum of Ar^{16+} ions were compared with each other. In this work, the G_3 ratio was measured on the TEXTOR (Julich, Germany) tokamak equipped with high-resolution Bragg spectrometers and other diagnostic instruments. The calculations carried out within the framework of the radiative-collision model using the ATOM, MZ, and GKU programs developed in the Lebedev Physical Institute, Russian Academy of Sciences, are in agreement, to the experimental accuracy, with all the data obtained on the PLT (Princeton, USA), ALCATOR-C (Cambridge, USA), and TEXTOR tokamaks. It is shown that the previously observed factor of 1.3–2 discrepancies between the measured and G_3 values calculated using the HULLAC code and appreciably exceeding the experimental error are caused by the use of inaccurate atomic data and simplified atomic kinetics in those works. The results presented in this work are evidence for the high accuracy of our atomic data (transition rates) and for the possibility of effectively using, on their basis, the K_β lines of multicharged ions in X-ray spectrum diagnostics of electron temperature and density in laboratory and astrophysical coronal plasma sources. © *2003 MAIK "Nauka/Interperiodica".*

PACS numbers: 52.25.Os; 52.70.La; 52.80.Hc

1. The *K*-emission spectra caused by the *nl*–1*s* transitions of an optical electron filling a vacancy in the 1*s* shell of a multicharged ion are widely used in the study of high-temperature plasmas. The X-ray spectroscopy methods based on the analysis of relative intensities in the measured *K*-emission spectra allow one to determine the electron temperature and density, the distribution over ionization steps, and other parameters that are necessary for studying the fundamental and applied problems of plasma physics. In some cases, e.g., for astrophysical objects, X-ray spectra prove to be the only sources of information on the structure and dynamics of plasma formations. However, in spite of the fact that the first works devoted to the $K\alpha$ emission from the $n = 2$ levels (see, e.g., [1–3]) appeared more than a quarter of century ago, the error in the measured parameters still remains a quite topical problem.

The accuracy of the spectroscopic diagnostic techniques and even the very possibility of their use depend on the accuracy of the atomic data and the plasma-radiation models based on the equations of atomic kinetics and plasma dynamics. For multicharged ions with charge $z > 10$, the direct (beam) measurements of the collisional and radiative characteristics necessary for the calculation and interpretation of the *K* spectra are now practically absent. The only information sources on both binary and hydrodynamic processes are, thus, provided by the spectra of rarefied (coronal) plasmas in the devices of the EBIT type and tokamaks. Due to the narrow spectral lines, a plasma-beam EBIT source is traditionally used for the measurement and verification of the methods of calculating the electron–ion cross sections, the lifetimes of metastable states, and the wavelengths (see, e.g., [4, 5]). The TEXTOR studies of the $K\alpha$ radiation showed that the tokamak spectra can be efficiently used not only for the diagnostic purposes but also for verification of the data on the Maxwellian-averaged rates of elementary processes in plasmas. The spectra of the He-like argon ions ($z = 16$) calculated using, on the one hand, the ATOM and MZ program packages [6] and, on the other, the SUPERSTRUCTURE and DW programs [7] proved to be in agreement with the measured spectra to within an experimental error of ~10%. The accuracy of R-matrix calculation of the collisional characteristics of the He-like argon and iron ions was estimated in [8] at ~20%. A similar accuracy of ~10–20% was reported in [9] for the excitation cross sections of the $n = 2$ levels of ions with charge $z = 22$–26 calculated by the DW method on the basis of EBIT measurements (Livermore, USA). At the same

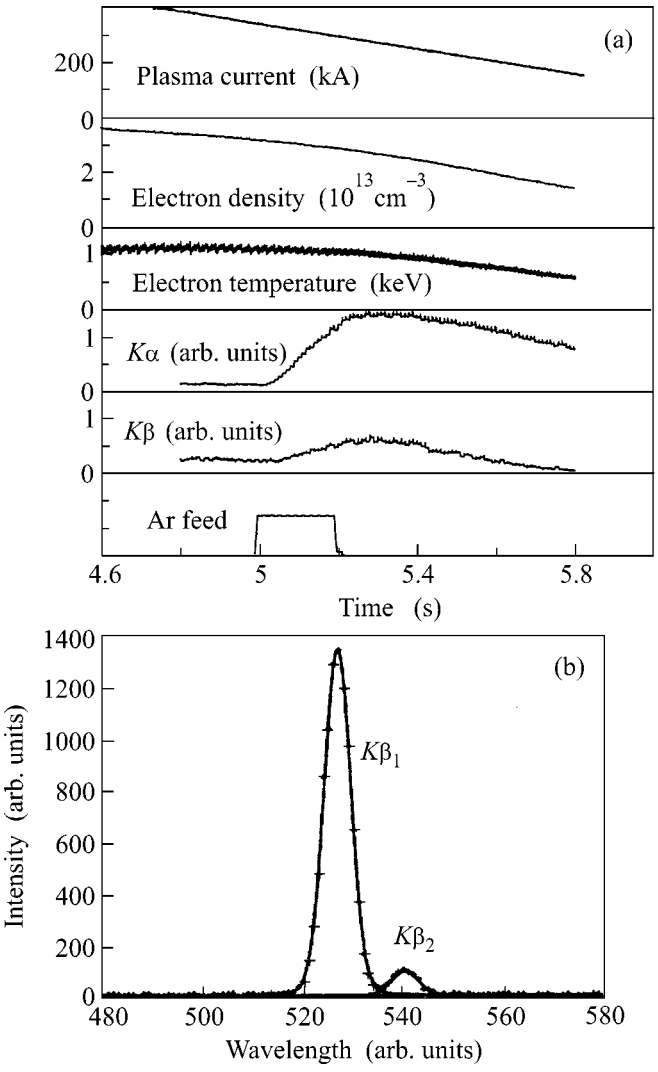

Fig. 1. (a) Time dependences of the plasma parameters and integrated $K\alpha$ and $K\beta$ intensities of argon ions in the appropriate spectral intervals. Argon atoms were ejected into plasma during 5–5.2 s, and the $K\alpha$- and $K\beta$-emission spectra of argon ions were observed in the time interval between 5.2 and 5.6 s. (b) Measured (crosses) Ar^{16+} $K\beta$-emission spectrum and its approximation by the Voigt curves (solid line).

time, the intensity ratios $G_3 = I[K\beta_2]/I[K\beta_1]$ of the intercombination and resonance lines, calculated for the transitions from $n = 3$ using the numerical HULLAC code and measured for the argon ions on the PLT tokamak [10] and the Livermore EBIT device [9] and for the argon and chlorine ions on the ALCATOR-C tokamak [11], differ from one another by approximately a factor of two. It is also worthy of note that the *ab initio* HULLAC calculations of the G_3 ratio are at variance, to within a factor of 1.3–2, with the experimental data reported in [12] for dense (laser) plasma. Such a discrepancy between the theory and experiment appreciably exceeds the measurement error and, thereby, casts doubt on the accuracy of the calculated atomic data underlying the high-temperature plasma diagnostic techniques based on the plasma *K* spectra.

This work is devoted to analysis of the reasons for the above-mentioned discrepancies between the theory and the experiment. To this end, the Ar^{16+} $K\beta$-line intensities were measured with a high accuracy (~10%) at low temperatures (~1 keV) on the TEXTOR tokamak simultaneously with the Ar^{16+} $K\alpha$ spectra, and the processes responsible for their formation in the tokamak plasmas were analyzed in detail. It is shown below that the results obtained within the framework of the radiative-collision model using the ATOM and MZ codes are in agreement, to within the error of measurements, with all the experimental data obtained on the PLT, ALCATOR-C, and TEXTOR tokamaks. The possible explanations for the discrepancies in the interpretation of the EBIT [9] and laser-plasma experiments [12] are also given.

2. The argon *K* spectra were studied on the TEXTOR tokamak equipped with a high-resolution X-ray spectrometer/polarimeter [13] incorporating two (horizontal and vertical) Bragg spectrometers designed for making polarization measurements of the radiation from the same central region of the tokamak plasma in the Johann scheme. The horizontal instrument, whose dispersion spanned the tokamak equatorial plane, was used to measure the $K\alpha$ spectra, while the vertical (perpendicularly arranged) instrument was used in our experiment for recording the $K\beta$-emission lines. The radius of curvature, the Bragg angle, and the spectral resolution $\lambda/\Delta\lambda$ were, respectively, 3850 mm, 54°, and 5000 for the horizontal and, respectively, 4630 mm, 43.3°, and 2000 for the vertical spectrometer. In both channels, the radiation was recorded using proportional counters. The electron temperature in the plasma core region was derived both from the $K\alpha$ spectra and, independently, from the Thomson scattering. The results of both measurements agree to within 5–10%. The $K\beta$ data obtained on the TEXTOR tokamak at temperatures $T_e \sim 1$ keV, in conjunction with the PLT measurements at $T_e \sim 2.3$ keV [10], made it possible to study the temperature dependence of the above-mentioned G_3 ratios.

The time evolution of plasma parameters and the total Ar^{16+} $K\alpha$- and $K\beta$-emission intensities in the TEXTOR experiment are presented in Fig. 1 together with an example of a measured contour covering the Ar^{16+} $K\beta_1$ and $K\beta_2$ lines. The experimental points in Fig. 1b were approximated by two Voigt contours with allowance for the instrumental function and the radial distribution of ion temperature.

3. The observed line intensities I_{if} of an optically thin plasma are expressed in terms of the luminosity function $\varepsilon_{if}(T_e, N_e)$ (in cm^{-3} s^{-1}) as

$$\varepsilon_{if} = N_i A^r_{if}, \quad (1)$$

where N_i [cm^{-3}] is the population density of the upper (i) level of the emitting ion; in the general case, it is determined from the system of rate equations

$$\frac{dN_i}{dt} = \sum_{m \neq i} N_m W_{mn} - N_i \sum_{n \neq i} W_{in}, \quad (2)$$

where A^r_{if} is the probability of spontaneous radiative $i \longrightarrow f$ transition; $W_{mn} = N_e C_{mn} + A^r_{mn}$ is the total $m \longrightarrow n$ transition probability; N_e is the electron density; $C_{mn} = \langle v\sigma_{mn} \rangle$ [$cm^3\ s^{-1}$] is the collision-induced $m \longrightarrow n$ transition rate equal to the cross section σ_{mn} averaged over the electron distribution in velocity v; and the integer indices n, m, i, etc. number the energy levels of an ion with charge z and quantum-number set α.

In this work, the relative $K\beta$-line intensities of Ar^{16+} ions were determined through the calculation of line luminosities as functions of electron temperature and density in equilibrium plasma ($dN_i/dt = 0$) with Maxwellian electron velocity distribution. The radiative-collision model allowed for electron-impact excitation and ionization, as well as for dielectronic and radiative recombinations. The energy-level system used in the calculations for the Ar^{16+} ion included 53 1snl states with $n \leq 6$ and $l \leq 5$. The first 41 levels with $n \leq 4$ were described using quantum numbers $\alpha = 1snl$ (LSJ), and the levels with principal quantum numbers $n = 5$ and $n = 6$ were grouped into LS terms. The high-lying Rydberg states with $n > 6$ were taken into account by extrapolating the rates of elementary processes to the large quantum numbers n.

The excited-level populations were calculated using the GKU program [14], which was designed for numerically solving the set of Eqs. (2). The atomic characteristics (level energies, radiative transition probabilities, and the appropriate cross sections and rates) necessary for modeling the $K\beta$-emission spectra of the argon ions were obtained using the ATOM and MZ programs.

The MZ program is based on the perturbation theory with a small parameter $1/Z$ (Z is the nuclear charge) and the hydrogen-like basis set including all configurations (the complex) of the same parity for a given set of principal quantum numbers. This program was used to calculate the energy levels and the (radiative and autoionization) decay probabilities that are necessary for determining the dielectronic recombination rates of an He-like ion. The ion level energies E_J and the eigenvectors C_J are determined by diagonalizing the total Hamiltonian of the system with the relativistic corrections taken in the form of the Breit Hamiltonian. The coefficients C_J thus obtained correspond to the intermediate coupling scheme with allowance for the interconfiguration interaction.

In the ATOM calculations of the electron-impact-induced transitions between the levels of He-like argon, the Coulomb–Born exchange approximation modified by the additional orthogonalization of the continuum and bound-state wave functions for the exchange amplitude was used. The configuration interaction between the target states was taken into account by using the coefficients C_J obtained with the MZ program. The resonance contribution to the rates of transition to the $n = 2$ levels was taken into account within the framework of the rate Eqs. (2). The ATOM program was also used to calculate the radiative transition probabilities between the Ar^{16+} levels and the radiative recombination rates of the He-like 1snl levels. A more detailed description of the radiative-collision model and the above-mentioned methods of atomic data calculation, as well as the discussion of the possible errors in determining the luminosity functions will be given elsewhere. Note that the collisional characteristics obtained in this work are in agreement with the results obtained by the other (DW, R-matrix [8], etc.) methods to within 10%.

4. In the tokamak spectrum, the ratio of radiation fluxes L and L' of two characteristic peaks corresponding, respectively, to the l and l' lines in the spectral intervals [L] and [L'] including these lines can conveniently be written as

$$i^{L'}_L(T) = i^{l'}_l(T)\phi\gamma^{L'}_L, \quad (3)$$

where $i^{l'}_l(T)$ is the relative intensity of the lines l and l' making the major contribution to L and L':

$$i^{l'}_l(T) = \varepsilon_{l'}(T)/\varepsilon_l(T). \quad (4)$$

Here, ε_l is the lth-line luminosity defined by Eq. (1) and taken as a function of the electron temperature $T = T_e(0)$ in the tokamak central zone ($r = 0$); the correction coefficient ϕ accounts for the contribution from the blending lines falling within the intervals [L] and [L']; and $\gamma^{L'}_L$ is the factor depending on the radial distributions of electron density $N_e(r)$ and temperature $T_e(r)$.

The temperature dependences calculated for the ratio $G_3(T_e)$ in equilibrium plasma with electron density $N_e \approx 10^{13}$–10^{14} cm^{-3}, for which the coronal approximation is true and which corresponds to the densities in the TEXTOR plasma, are shown in Fig. 2 for the case where the contributions from the complete recombination and upper-level cascades were ignored. From the results presented in Fig. 2 it is seen that the direct excitation makes the main contribution (≈85%) in the range of electron temperatures $T_e \sim 1$ keV, while the 1$s3p$ recombination and the radiation cascades comprise, respectively, ≈10% and ≈5%. At higher temperatures where $T_e \sim 2$ keV, the contribution from the direct excitation, recombination, and cascades is distributed in the ratio of ≈70%, 20%, and 10%, respectively.

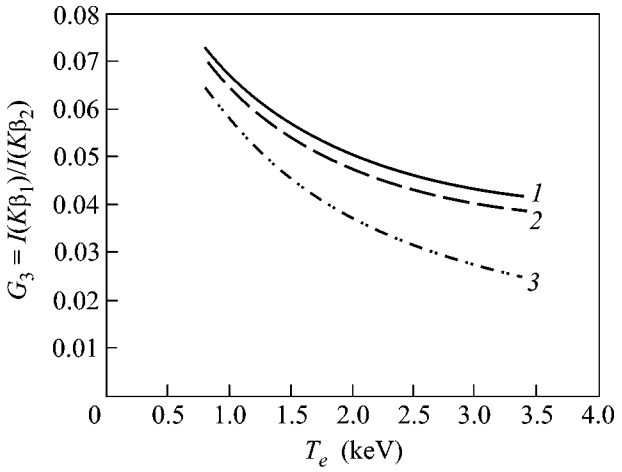

Fig. 2. Illustration of the contributions of various processes to the T_e dependence of the intensity ratio $G_3 = I[K\beta_2]/I[K\beta_1]$: (*1*) full calculation; (*2*) calculation without taking into account the cascades from the upper levels 1*snl* with $n \geq 4$; and (*3*) the same as in (*2*) but without taking into account the recombination of the He-like 1*s*3*l* ion levels.

Expressions (3) and (4) and the $K\beta_1$- and $K\beta_2$-line luminosities calculated using the equilibrium plasma model gave the ratio $G_3 = i_l^{l'}(T)$ as a function of temperature. The temperature dependences of the ratio G_3 calculated in this work and in [10] and [5] are presented in Fig. 3a. The ratio G_3 obtained in this work is close to the results obtained in [15] and is at variance with the latter to within 10% in the temperature range considered. Note that the atomic characteristics were obtained in [15] also using the ATOM program. The observed discrepancies are, likely, due to the fact that the contribution from the $K\beta$ dielectronic recombination was not taken into account in that work.

The results of calculations carried out in [10] using the numerical HULLAC package differ appreciably (by approximately a factor of two) from the other results presented in Fig. 3a. This discrepancy (≈50%) is explained in part by the fact that the contributions from the upper-level radiation cascades and Ar^{16+} excited-level recombination were not taken into account in [10]. The remaining discrepancy is caused by the difference between the direct excitation rates of the $K\beta_1$ line (≈10%) and between the branching ratios of the $K\beta_2$ line (0.22 in this work and 0.17 in [10]).

5. The results of the TEXTOR and PLT measurements of the ratios $i_L^{L'}$ defined in Eq. (3) are also presented in Fig. 3a for the temperatures $T_e \sim 1$ keV and $T_e \sim 2.3$ keV [10], respectively. Curve *4* in this figure is for the theoretical ratio with allowance made for the coefficient ϕ including a contribution from the dielectronic satellites due to the transitions of the 1*s*3*pnl* ⟶

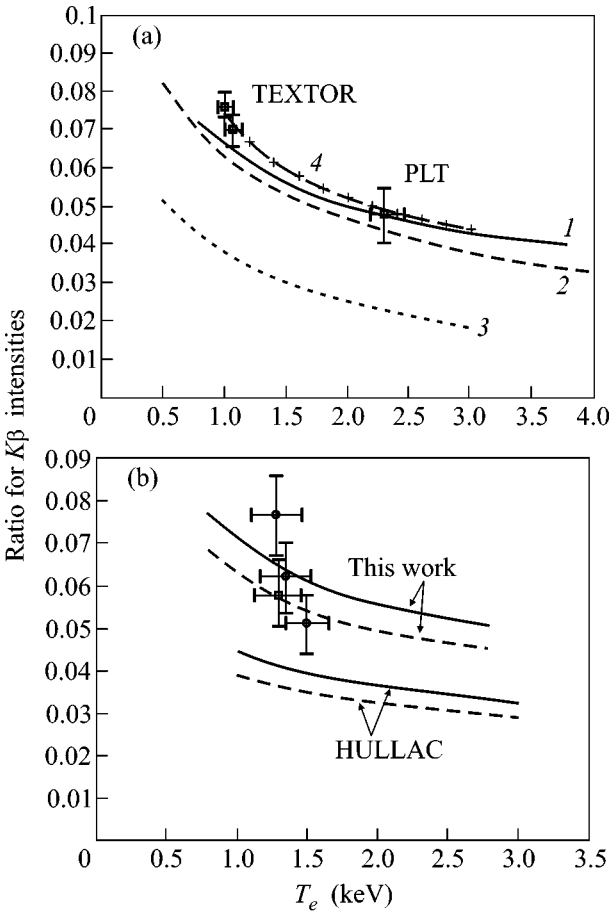

Fig. 3. (a) Comparison of the theoretical ratios $G_3(T_e)$ obtained by different authors for the Ar^{16+} $K\beta$ lines in low-density plasmas and the results of the TEXTOR measurements at temperatures $T_e \sim 1$ keV (this work) and the PLT measurements at $T_e \sim 2.3$ keV [10]: (*1*) this work; (*2*) calculations in [15]; (*3*) HULLAC calculation [10]; (*4*) the same as in curve *1*, but with allowance for the contribution from the blending dielectronic satellites. (■) The experimental data. (b) The G_3 ratio in a dense plasma; ● and ■ are the experimental points for the densities $N_e = 6 \times 10^{20}$ cm^{-3} and $N_e = 1.1 \times 10^{21}$ cm^{-3} [12], respectively; the solid line corresponds to the calculations with $N_e = 6 \times 10^{20}$ cm^{-3} and the dashed line is for $N_e = 1.1 \times 10^{21}$ cm^{-3}.

$1s^2nl$ type with $n \geq 4$ and converging to the $K\beta_1$ and $K\beta_2$ lines as n increases. The contribution of satellites to the G_3 ratio was obtained on the basis of the results reported in [5], where the spectra of these satellites were directly measured on an EBIT device. One can see from this figure that the inclusion of blending satellites enhances the G_3 ratio by approximately 10% at temperature $T_e \sim 1$ keV and makes virtually no contribution to this ratio at $T_e \geq 2$ keV. Analysis of the experimental conditions show that the factor $\gamma_L^{L'}$ has no effect on the

G_3 ratio to within a few percent and, thus, is disregarded in this work. It should be noted that the possible deviation from the equilibrium conditions as a result of ion transport and charge exchange on neutrals in plasma, as observed in the $K\alpha$ spectra of argon ions, introduces an error of about 5% when measuring on the TEXTOR tokamak in a temperature range of 1–2.5 keV. Therefore, the comparison shows that the model used in our work allows the measured ratio $i_L^{L'}$ to be described within the experimental accuracy. A more detailed discussion of the transport effects in the K spectra is beyond the framework of this study and will be given elsewhere.

One should also note the work [11], where the chlorine and argon He-like K spectra were measured on the ALCATOR-C tokamak, while the theoretical interpretation of the experimental results was carried out using the HULLAC code. In that work, the Cl^{15+} G_3 ratio was measured at the temperature $T_e \approx 1.2$ keV and the electron density $N_e \approx 1.8 \times 10^{14}$ cm^{-3} to give a value of ~0.05, whereas the theoretically predicted value is $G_3 \sim 0.03$. For the Ar^{16+} ions, the ratio $G_4 = I[K\gamma_2]/I[K\gamma_1]$ of the $K\gamma$-lines corresponding to the $1s4p\,^3P_1$–$1s^2$ ($K\gamma_2$ line) and $1s4p\,^1P_1$–$1s^2$ ($K\gamma_1$ line) transitions was also observed in [11] for the plasma parameters $T_e \approx 2.05$ keV and $N_e \approx 1.1 \times 10^{14}$ cm^{-3}. The measured value was $G_4^{\exp} \approx 0.05$, whereas the HULLAC calculations gave $G_4 \approx 0.029$. Our calculations and estimates of the G_3 ratio for chlorine ions and the G_4 ratio for argon ions give, respectively, ≈0.048 and ≈0.045, in agreement with the measured values to within an experimental error. A systematic underestimate of the theoretical results for the Ar^{16+} and Cl^{15+} G_3 ratios and the Ar^{16+} G_4 ratio, as compared to the results of the PLT, ALCATOR-C, and TEXTOR measurements, probably indicates that the numerical HULLAC code is a common source of these errors.

The G_3 values calculated for the densities $N_e = 6 \times 10^{20}$ cm^{-3} and $N_e = 1.1 \times 10^{21}$ cm^{-3} are presented in Fig. 3b, where they are compared with the theoretical and experimental data reported in [12]. In [12], the corresponding ratios were measured in laser plasma with gaseous targets, for which the C_3H_8 and C_5H_{12} compounds were used. The calculations in [12] were performed using the HULLAC code, and the theory also showed a sizable discrepancy (up to a factor of two) with the experiment. One can see in Fig. 3b that the G_3 ratio calculated in our work for the electron density $N_e = 1.1 \times 10^{21}$ cm^{-3} with inclusion of the contribution from the dielectronic satellites (ϕ factor) agrees well with the measurements in [12] to within the experimental error. The presence of three experimental points with a rather large scatter in a narrow temperature interval at $N_e = 6 \times 10^{20}$ cm^{-3} impedes the interpretation of these experiments. Nevertheless, our calculations are, on average, in good agreement with the experiment.

The atomic data obtained in this work were also used to compare the theoretical ratio G_3 with its experimental value measured in the beam experiment on an EBIT device [9]. The cited experiment gave the value $G_3^{\exp} = 0.161$ for the Ar^{16+} ion. The electron-beam energy $E_b = 3800$ eV was chosen to be near the excitation threshold of the resonance $K\beta_1$ line to avoid the occupation of the $n = 3$ levels through the radiation cascades from the $n \geq 4$ levels. In this case, the line luminosities can be represented as

$$\varepsilon_{if} = N_e N_f K_r(i) C_{if}, \quad (5)$$

where N_f is the ground-state population of the He-like ions; $K_r(i)$ is the branching ratio for the ith level; and C_{if} is the $f \longrightarrow i$ excitation rate. The HULLAC calculations made in [9] gave a value of 0.071 for the ratio G_3, and $G_3 = 0.085$ was obtained in [16]. The ratio $G_3 = 0.11$ obtained in our work is in better agreement with the experiment than the above-mentioned results. A discrepancy of ≈30% between the results of this work and the experiment is likely explained by the fact that the contributions from the resonances of the $1s4l'nl$ ($n \geq 4$) types to the excitation cross sections near the subsequent reaction thresholds were not taken into account.

Note, in conclusion, that the results presented in this work are evidence both of a high accuracy of the atomic data calculated using the above-mentioned methods and corresponding program packages (ATOM and MZ; SUPERSTRUCTURE and DW; R-matrix method) and of the possibility of efficiently using, within the framework of a comprehensive atomic model, the relative $K\beta$-line intensities of the He-like ions for X-ray spectral diagnostics of the laboratory and astrophysical plasma sources.

This work was supported by the Russian Foundation for Basic Research (project nos. 03-02-16053 and 02-02-16613) and by the program of the Section of Physical Sciences of the Russian Academy of Sciences "Optical Spectroscopy and Frequency Standards."

REFERENCES

1. A. H. Gabriel and C. Jordan, Mon. Not. R. Astron. Soc. **145**, 241 (1969).
2. L. P. Presnyakov and A. M. Urnov, J. Phys. C **40**, 279 (1979).
3. V. A. Boĭko, A. V. Vinogradov, S. A. Pikuz, *et al.*, *X-Ray Spectroscopy of Laser Plasma* (VINITI, Moscow, 1980), Vol. 27.
4. A. J. Smith, M. Bitter, H. Hsuan, *et al.*, Phys. Rev. A **47**, 3073 (1993).
5. A. J. Smith, P. Beiersdorfer, V. Decaux, *et al.*, Phys. Rev. A **54**, 462 (1996).

6. V. P. Shevelko and L. A. Vainshtein, *Atomic Physics for Hot Plasmas* (Inst. of Physics, Bristol and Philadelphia, 1993).
7. W. Eissner and M. J. Seaton, J. Phys. B **5**, 2187 (1972).
8. A. D. Whiteford, N. R. Badnell, C. P. Ballance, *et al.*, J. Phys. B **34**, 3179 (2001).
9. A. J. Smith, P. Beiersdorfer, K. J. Reed, *et al.*, Phys. Rev. A **62**, 012704 (2000).
10. P. Beiersdorfer, A. L. Osterheld, T. W. Phillips, *et al.*, Phys. Rev. E **52**, 1980 (1995).
11. J. E. Rice, K. B. Fournier, U. I. Safronova, *et al.*, New J. Phys. **1**, 19.1 (1999).
12. S. H. Glenzer, K. B. Fournier, C. Decker, *et al.*, Phys. Rev. E **62**, 2728 (2000).
13. J. Weinheimer, I. Ahmad, O. Herzog, *et al.*, Rev. Sci. Instrum. **72**, 2566 (2001).
14. I. L. Beĭgman, Preprint No. 2, FIAN SSSR (Physical Inst., USSR Academy of Sciences, Moscow, 1989).
15. F. B. Rosmej, Phys. Rev. E **58**, R32 (1998).
16. H. L. Zhang, D. H. Sampson, and R. E. H. Clark, Phys. Rev. A **41**, 198 (1990).

Translated by V. Sakun

JETP Letters, Vol. 78, No. 6, 2003, pp. 369–373. Translated from Pis'ma v Zhurnal Éksperimental'noĭ i Teoreticheskoĭ Fiziki, Vol. 78, No. 6, 2003, pp. 822–826.
Original Russian Text Copyright © 2003 by Samokhvalov.

Maximal Supercurrent of a Josephson Junction in a Field of Magnetic Particles

A. V. Samokhvalov

Institute of Physics of Microstructures, Russian Academy of Sciences, Nizhni Novgorod, 603950 Russia

e-mail: samokh@ipm.sci-nnov.ru

Received May 5, 2003; in final form, July 22, 2003

The maximal supercurrent I_m of a short Josephson junction formed by an edge contact of two superconducting films is calculated for the case where the junction is placed in a periodic field produced by a chain of magnetic nanoparticles. The commensurability effects occurring when the magnetic flux of a homogeneous external field H_0 through an elementary cell is equal to an integral number of magnetic flux quanta Φ_0 are considered. The effects give rise to additional maxima in the $I_m(H_0)$ dependence. *© 2003 MAIK "Nauka/Interperiodica".*

PACS numbers: 74.50.+r; 74.78.-w

Studies of magnetic nanostructures (arrays of magnetic dots [1] or thin ferromagnetic layers [2]) interacting with a superconductor show that such hybrid systems exhibit some interesting phenomena due to the interaction of the magnetic and superconducting subsystems. If no proximity effect occurs between ferromagnet and superconductor, the interaction between the subsystems proceeds through slowly decaying stray fields [3]. A highly inhomogeneous magnetic field produced by magnetic dots partially penetrates into the superconductor to induce Meissner screening currents in it. In turn, these currents affect the magnetization distribution and can form different types of magnetic ordering [2] or cause the transformation of the domain structure in a ferromagnet [4].

A strong effect of the preliminary magnetization of Co particles on the maximal current of an edge Josephson junction was observed in [5], which allowed us to propose a new interference method for determining the local parameters of the nanoparticle magnetization distribution. The method is based on one of the properties of Josephson junctions, namely, on the appearance of the magnetic-field-induced diffraction and interference caused by the wave properties of Cooper pairs and the phase coherence of order parameter on both sides of the junction [6]. Note that the extremely high sensitivity of the Josephson current to magnetic field provides the basis for the most important applications of the Josephson effect and also allows one to study in detail the properties of the junction itself [7].

This paper presents a theoretical study of the influence of a chain of magnetic particles on the dependence of the critical current of an edge Josephson junction on the external magnetic field for different orientations of the particle magnetic moments.

Consider a short Josephson junction ($W \ll \lambda_J = \sqrt{c\Phi_0/16\pi^2\lambda j_c}$) formed at the edge contact of two thin superconducting (SC) films whose thickness d is much smaller than the London penetration depth λ (Fig. 1). In the above expression, j_c is the critical current density of the junction. Let a chain of point magnetic dipoles be placed at a height h above the SC film and at a distance b from the junction plane $y = 0$. The dipole magnetic moment **M** is assumed to lie in the plane parallel to the SC films. First of all, we determine the magnetic field of the dipoles in the junction plane and the gauge-invariant phase difference φ^M produced by this field at the junction.

Taking into account that, when $d \ll \lambda$, the distributions of the vector potential **A** and the current **j** throughout the SC film do not depend on the transverse coordi-

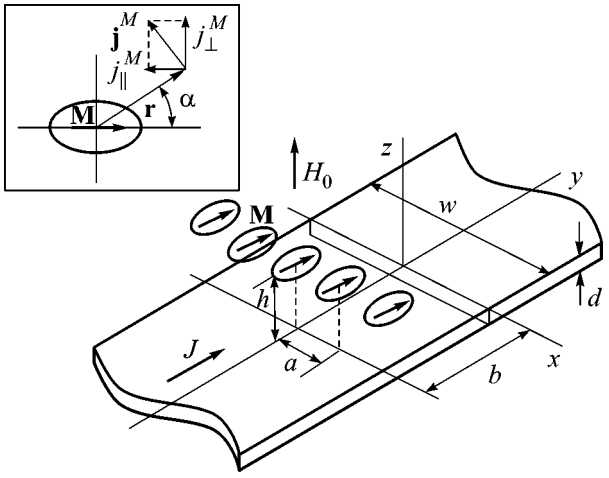

Fig. 1. Schematic diagram of a Josephson junction with a chain of magnetic dipoles **M**.

0021-3640/03/7806-0369$24.00 © 2003 MAIK "Nauka/Interperiodica"

nate z, let us consider the screening of the dipole magnetic field by the SC plane $z = 0$. The screening current density $\mathbf{g} = \mathbf{j}d$ is expressed through the vector potential $\mathbf{A}$ as

$$\mathbf{g} = (g_x, g_y) = \frac{c}{4\pi\Lambda}(\mathbf{S} - \mathbf{A})\delta(z), \quad (1)$$

and the vector potential, in its turn, satisfies the following equation over all space:

$$\nabla \times \nabla \times \mathbf{A} + \frac{1}{\Lambda}\mathbf{A}\delta(z) = 4\pi\nabla \times \sum_m \mathbf{M}_m + \frac{1}{\Lambda}\mathbf{S}\delta(z). \quad (2)$$

Here, $\mathbf{M}_m = \mathbf{M}\delta(\mathbf{R} - \mathbf{R}_m)$ is the magnetic moment of a dipole positioned at point $\mathbf{R}_m$, and $\Lambda = \lambda^2/d$ is the effective penetration depth determining the screening properties of thin superconducting film [8]. The vortex source $\mathbf{S}$ in Eq. (2) depends on the gradient of phase difference at the junction $\varphi^M(x)$ [9]:

$$\nabla \times \mathbf{S} = \frac{\Phi_0}{2\pi}\frac{d\varphi^M}{dx}\delta(y)\mathbf{z}_0, \quad \nabla \cdot \mathbf{S} = 0. \quad (3)$$

Since the magnetic dipole field decreases relatively fast with distance, the effect of film edges can be ignored [10].

Equations (1)–(3) should be complemented with a boundary condition in the Josephson junction plane. If the supercurrent through the junction depends on the phase difference in the simplest harmonic manner as $j = j_c\sin(\varphi)$, the component of the current $\mathbf{g}$ along the normal to the junction should satisfy the following condition in the plane $y = 0$:

$$g_y(x, 0) = j_c d\sin(\varphi^M(x)). \quad (4)$$

Assuming that critical current j_c is small, we seek the distributions of phase difference φ^M and vector potential $\mathbf{A}$ on the assumption that the junction is fully impenetrable, so that it can be replaced by an infinitely narrow discontinuity of the SC film. In this approximation, the screening current cannot flow through the surface $y = 0$, and boundary condition (4) is simplified:

$$g_y(x, 0) = 0. \quad (5)$$

By virtue of the linearity of Eqs. (1)–(3) and (5), the desired distribution of vector potential A can be represented as the sum

$$\mathbf{A} = \mathbf{A}^M + \mathbf{A}^\varphi, \quad (6)$$

where $\mathbf{A}^M$ describes the vector potential of a system of point magnetic dipoles positioned near the infinite thin SC film and $\mathbf{A}^\varphi$ describes the distortions caused by the film discontinuity at the Josephson junction plane. Using Eqs. (1) and (6), the corresponding distribution of screening current $\mathbf{g}$ can be represented in the form

$$\mathbf{g} = \mathbf{g}^M + \mathbf{g}^\varphi,$$
$$\mathbf{g}^M = -\frac{c}{4\pi\Lambda}\mathbf{A}^M; \quad \mathbf{g}^\varphi = \frac{c}{4\pi\Lambda}(\mathbf{S} - \mathbf{A}^\varphi). \quad (7)$$

In the absence of magnetic dipoles, initial equation (2) can be reduced to the equation for the magnetic-field projection $B_z^\varphi = \{\nabla \times \mathbf{A}^\varphi\}_z$ onto the normal to the SC film:

$$B_z^\varphi - 2\Lambda\frac{\partial B_z^\varphi}{\partial z} = \frac{\Phi_0}{2\pi}\frac{d\varphi^M}{dx}\delta(y), \quad (8)$$

where the source on the right-hand side is determined by the desired phase-difference distribution $\varphi^M(x)$. Note that Eq. (8) describes the distribution of magnetic field in a long Josephson junction ($W \gg \lambda_J$) between two thin SC films contacting along the edge [9, 11]. Using the solutions obtained in the cited publications, we can express the y component $J^\varphi = g_y^\varphi(x, 0)$ of the current $\mathbf{g}^\varphi$ at the discontinuity surface through the Fourier spectrum

$$\phi^M(q) = \Lambda^{-1}\int dx\varphi^M(x)\exp(\imath qx/\Lambda)$$

of the phase difference $\varphi^M(x)$ at the junction:

$$J^\varphi = \frac{c\Phi_0}{4\pi^4\Lambda^2}\int dq e^{-\imath qx/\Lambda}q^2\phi^M(q)Q(q), \quad (9)$$

$$Q(q) = \frac{\arctan(\sqrt{4q^2 - 1}/(1 + 2|q|))}{\sqrt{4q^2 - 1}}. \quad (10)$$

The relation between the current J^φ and the phase difference φ^M proves to be of the integral type, which reflects the strong influence of slowly decaying stray fields [9].

The distribution of the vector potential $\mathbf{A}^M$ of magnetic dipoles in the presence of the SC film can be determined by setting $\mathbf{S} = 0$ on the right-hand side of Eq. (2). Let us first consider a single magnetic dipole $\mathbf{M}$ positioned at a height h above the film surface. Using the Fourier transformation, we obtain the following expressions for the screening current components longitudinal ($\|$) and transverse ($\perp$) with respect to the magnetic moment $\mathbf{M}$ at an arbitrary point of the film; i.e., $\mathbf{g}^M = \mathbf{g}_\|^M + \mathbf{g}_\perp^M$ (see inset in Fig. 1):

$$g_\|^M = -\frac{cM}{4\pi\Lambda^3}\sin(2\alpha)\int_0^\infty du\frac{u^2J_2(ur/\Lambda)}{1 + 2u}e^{-uh/\Lambda}, \quad (11)$$

$$g_{\perp}^{M} = \frac{cM}{4\pi\Lambda^3}\left\{\cos(2\alpha)\int_0^\infty du\frac{u^2 J_2(ur/\Lambda)}{1+2u}e^{-uh/\Lambda} + \int_0^\infty du\frac{u(1+u)J_0(ur/\Lambda)}{1+2u}e^{-uh/\Lambda} - \frac{h\Lambda^2}{[r^2+h^2]^{3/2}}\right\}, \quad (12)$$

where $J_{0,2}$ are the zero-order and second-order Bessel functions, respectively, and α is the angle between the direction of the dipole moment **M** and the radius vector **r** in the film plane.

This solution can easily be generalized to the case of an infinite chain of point magnetic dipoles $\mathbf{M} = M_x\mathbf{x}_0 + M_y\mathbf{y}_0$ spaced at a distance a and oriented in the same (but arbitrarily chosen) direction in the film plane, as shown in Fig. 1. For convenience, the subsequent calculations are performed with dimensionless quantities and the distances are expressed in units of effective penetration depth Λ: $x, y, a, b, h, R \longrightarrow x/\Lambda, y/\Lambda, a/\Lambda, b/\Lambda, h/\Lambda, R/\Lambda$. Taking into account the periodicity and choosing the origin of coordinates at one of the dipoles, we represent the distribution of the screening current component perpendicular to the junction, $J^M = g_y^M(x, 0)$, as a Fourier series in spatial harmonics $q_a = 2\pi/a$:

$$J^M(x) = -\frac{cM}{4\pi\Lambda^3}\sum_{n=1}^{\infty}[\mu_x G_x^n\cos(nq_a x) - \mu_y G_y^n\sin(nq_a x)], \quad (13)$$

where $\mu_x = M_x/M$, $\mu_y = M_y/M$, $M = \sqrt{M_x^2 + M_y^2}$, and the amplitudes of the spatial harmonics $G_{x,y}^n$ can be expressed as

$$G_x^n = \frac{4hq_a n}{a\sqrt{h^2+b^2}}K_1(nq_a\sqrt{h^2+b^2}) - \frac{4}{a}\int_{nq_a}^{\infty}dq\left[\frac{q\cos(b\sqrt{q^2-n^2q_a^2})}{(1+2q)\sqrt{q^2-n^2q_a^2}} + \frac{2\sin(b\sqrt{q^2-n^2q_a^2})}{b(1+2q)}\right]e^{-qh} + \frac{8b^2}{a}\int_0^\infty dv\frac{\cos(nq_a v)}{v^2+b^2}\int_0^\infty dq\frac{q^2 J_2(q\sqrt{v^2+b^2})}{1+2q}e^{-qh}, \quad (14)$$

$$G_y^n = \frac{8b}{a}\int_0^\infty dv\frac{v\sin(nq_a v)}{v^2+b^2}\times\int_0^\infty dq\frac{q^2 J_2(q\sqrt{v^2+b^2})}{1+2q}e^{-qh}. \quad (15)$$

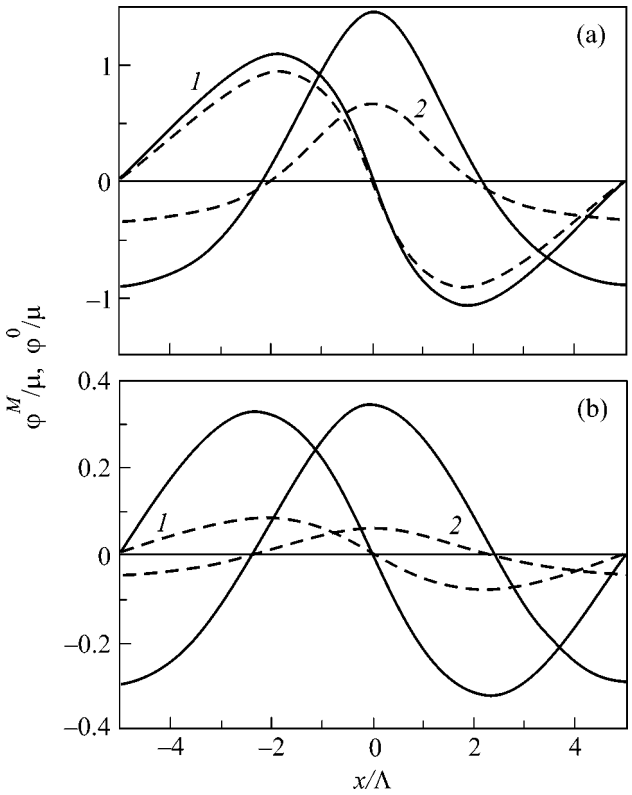

Fig. 2. Phase-difference distribution $\varphi^M(x)$ in the junction for two orthogonal directions of the magnetic moment of particles ((*1*) $\mathbf{M} \perp \mathbf{x}_0$ and (*2*) $\mathbf{M} \parallel \mathbf{x}_0$) and different distances between the particles and the junction: b = (a) 0.2 and (b) 0.4 μm. For comparison, the dashed lines show the phase-difference distribution $\varphi^0(x)$ (Λ = 0.1 μm, W = 5 μm, a = 1 μm, and h = 0.1 μm).

The corresponding distribution of the phase difference $\varphi^M(x)$ induced at the junction by the chain of magnetic dipoles can be obtained from boundary condition (5) at the discontinuity surface,

$$q_y(x, 0) = J^{\varphi}(x) + J^M(x) = 0,$$

and, in turn, can also be represented as a Fourier series expansion:

$$\varphi^M(x) = \frac{M}{\Phi_0\Lambda}\sum_{n=1}^{\infty}[\mu_x P_x^n\cos(nq_a x) - \mu_y P_y^n\sin(nq_a x)], \quad (16)$$

$$P_{x,y}^n = \frac{\pi^2}{2n^2q_a^2Q(nq_a)}G_{x,y}^n. \quad (17)$$

Formulas (14)–(17) obtained above determine the gauge-invariant phase-difference φ^M caused by an infinite chain of point magnetic dipoles **M** at the Josephson junction formed between two thin SC films. Figure 2 shows the phase-difference distributions $\varphi^M(x)$ calcu-

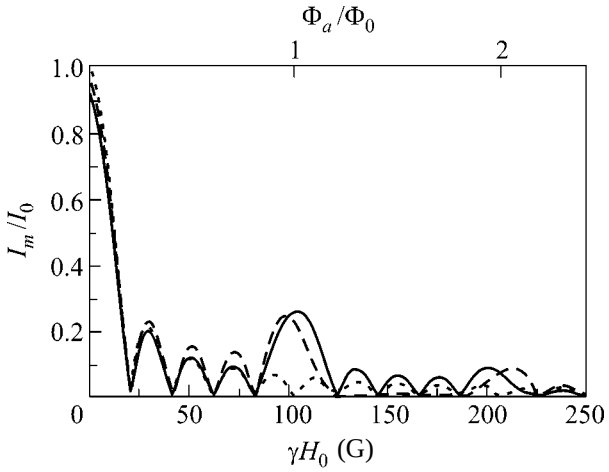

Fig. 3. Dependence of the maximal current I_m through the junction on the effective external field γH_0 for two orthogonal directions of the magnetic moment $\mathbf{M}$ of the infinite chain of particles; the solid line refers to $\mathbf{M} \parallel \mathbf{x}_0$ and the dashed line, to $\mathbf{M} \perp \mathbf{x}_0$. The dotted line represents the maximal supercurrent in the absence of magnetic particles. $I_0 = j_c d\Lambda$, $M = 10^{-10}$ erg/G, $\Lambda = 0.1$ μm, $W = 5$ μm, $a = 1$ μm, $b = 0.2$ μm, and $h = 0.1$ μm.

lated from Eqs. (14)–(17) for two orthogonal directions of magnetic dipole moment, $\mathbf{M} \parallel \mathbf{x}_0$ ($\mu_x = 1$, $\mu_y = 0$) and $\mathbf{M} \perp \mathbf{x}_0$ ($\mu_x = 0$, $\mu_y = 1$), and for different distances b between the magnetic particles and the junction. For comparison, the dashed curves present the phase distributions $\varphi^0(x)$:

$$\frac{d\varphi^0}{dx} = \frac{4\pi\Lambda^2}{\Phi_0} B_z^0(x, 0, 0), \tag{18}$$

where the dipole magnetic field $\mathbf{B}^0 = \nabla \times \mathbf{A}^0$ in the junction region is calculated without taking into account the screening currents in the superconductor:

$$\mathbf{A}^0 = \sum_m \frac{\mathbf{M} \times (\mathbf{R} - \mathbf{R}_m)}{\Lambda^2 |\mathbf{R} - \mathbf{R}_m|^3}. \tag{19}$$

One can readily see that the distribution $\varphi^M(x)$ noticeably differs from $\varphi^0(x)$ and that a considerable influence of magnetic particles on the junction is retained at distances $r = \sqrt{b^2 + h^2}$ much greater than those predicted by simple estimates (18) and (19). This result is explained by the fact that the screening current density in the superconductor and the magnetic field component tangential to the SC film surface decrease slowly with increasing distance from a magnetic dipole. The difference between the distributions φ^M and φ^0 is particularly large if the distance between the magnetic particles and the junction is great ($r \gg \Lambda$).

The current through the Josephson junction depends both on the phase difference φ^M caused by the magnetic field of the particles and on the strength H_0 of the external magnetic field applied normally to the SC film surface. If we assume that the external field inside the junction is homogeneous and equal to γH_0, where γ is the dimensionless demagnetizing factor [12, 13], the phase-difference distribution in the junction can be represented as

$$\varphi(x) = \varphi^M(x) + hx, \quad h = \frac{2\pi\Lambda^2}{\Phi_0}\gamma H_0. \tag{20}$$

Assuming that the Josephson current density j_c is uniform throughout the cross section, the total current I through the junction of width $W = w\Lambda$ is determined by the expression

$$I = j_c d\Lambda \int_{-w/2}^{w/2} dx \sin(\varphi(x) + \varphi_0), \tag{21}$$

where the parameter φ_0 depends on the bias current through the junction. The determination of the maximal current through the Josephson junction is reduced to finding the value of parameter φ_0 at which integral (21) reaches its maximum. Figure 3 shows the dependences of the maximal Josephson current I_m through the junction on the field γH_0 for two orthogonal directions of the dipole moment $\mathbf{M}$ of the infinite chain of particles. For comparison, the dotted curve represents the dependence of the maximal supercurrent through the Josephson junction on the external field in the absence of magnetic particles. The magnetic field ΔH_0 corresponding to the period of "diffraction structure" is determined by the junction width W [7]:

$$\Delta H_0 = \Phi_0/2\pi\gamma\Lambda W.$$

In the case that the Josephson junction is placed in the periodic field of magnetic particles, the dependence $I_m(\gamma H_0)$ changes qualitatively. It exhibits additional maxima whose widths are equal to the width of the main maximum and positions are determined by the resonance condition for the spatial Josephson current wave $j \sim \sin(hx)$ and the periodic distribution of the phase difference $\varphi^M(x)$ produced at the junction by the magnetic particles—$h = q_a n$, where n is an integer. From the latter equality, it follows that the additional maxima arise when the magnetic flux Φ_a of effective field γH_0 through a elementary cell $S_a = 2\Lambda \times a$ is equal to integral number of magnetic flux quanta Φ_0:

$$\Phi_a = n\Phi_0, \quad \Phi_a = \gamma H_0 S_a. \tag{22}$$

Similar commensurability effects were observed in the experimental study of the influence of periodic defects on the critical current of a long Josephson junction in an external magnetic field [14].

In closing, it should be noted that the assumption about the homogeneity of the external field H_0 inside the junction does not always apply to the film geometry

under consideration with a large demagnetizing factor [15]. The inhomogeneity of an external field in the junction region primarily manifests itself near the points where $I_m(H_0)$ becomes zero and can noticeably distort the field dependence for the maximal current of the junction. However, the commensurability effects, resulting in the appearance of additional maxima, will occur in this case as well.

I am grateful to A.A. Fraerman and A.S. Mel'nikov for useful discussions. This work was supported by the Russian Foundation for Basic Research (project no. 03-02-16774) and the program "Quantum Macrophysics" of the Russian Academy of Sciences.

REFERENCES

1. J. I. Martin, M. Velez, J. Nogues, and I. K. Schuller, Phys. Rev. Lett. **79**, 1929 (1997); D. J. Morgan and J. B. Ketterson, Phys. Rev. Lett. **80**, 3614 (1998).
2. L. N. Bulaevskii, E. M. Chudnovsky, and M. P. Maley, Appl. Phys. Lett. **76**, 2594 (2000); M. Lange, M. J. Van Bael, V. V. Moshchalkov, and Y. Bruynseraede, cond-mat/0205470; S. Erdin, I. F. Lyuksyutov, V. Pokrovsky, and V. M. Vinokur, Phys. Rev. Lett. **88**, 017001 (2002).
3. I. F. Lyuksyutov and V. Pokrovsky, Phys. Rev. Lett. **81**, 2344 (1998).
4. L. E. Helseth, P. E. Goa, H. Hauglin, *et al.*, Phys. Rev. B **65**, 132 514 (2002).
5. A. Y. Aladyshkin, A. A. Fraerman, S. A. Gusev, *et al.*, J. Magn. Magn. Mater. **258–259**, 406 (2003).
6. B. D. Josephson, Adv. Phys. **14**, 419 (1965).
7. A. Barone and G. Paterno, *Physics and Applications of the Josephson Effect* (Wiley, New York, 1982; Mir, Moscow, 1984).
8. J. Pearl, J. Appl. Phys. **5**, 65 (1964).
9. Yu. M. Ivanchenko and T. K. Soboleva, Fiz. Tverd. Tela (Leningrad) **32**, 2029 (1990) [Sov. Phys. Solid State **32**, 1181 (1990)].
10. A. S. Mel'nikov, Yu. N. Nozdrin, I. D. Tokman, *et al.*, Phys. Rev. B **58**, 11672 (1998).
11. V. G. Kogan, V. V. Dobrovitskii, J. R. Clem, *et al.*, Phys. Rev. B **63**, 144501 (2001).
12. J. Gu, W. Cha, K. Gamo, and S. Namba, J. Appl. Phys. **50**, 6437 (1979).
13. R. G. Humphreys and J. A. Edwards, Physica C (Amsterdam) **210**, 42 (1993).
14. M. A. Itzler and M. Tinkham, Phys. Rev. B **51**, 435 (1995).
15. K. L. Likharev, Izv. Vyssh. Uchebn. Zaved., Radiofiz. **14**, 909 (1971).

Translated by E. Golyamina

JETP Letters, Vol. 78, No. 6, 2003, pp. 374–378. Translated from Pis'ma v Zhurnal Éksperimental'noĭ i Teoreticheskoĭ Fiziki, Vol. 78, No. 6, 2003, pp. 827–831.
Original Russian Text Copyright © 2003 by Rosmej, S. Pikuz, Jr., Magnitskii, Faenov, T. Pikuz, Efremov, Blazevic, Hoffmann.

X-Ray Spectroscopic Study of Stopping Dynamics for Ca^{6+} Ion in an Aerogel Target

O. N. Rosmej[1], S. A. Pikuz, Jr.[2, *], S. A. Magnitskii[2], A. Ya. Faenov[3], T. A. Pikuz[3], V. P. Efremov[4], A. Blazevic[5], and D. H. H. Hoffmann[1, 5]

[1] *Gesellschaft für Schwerionenforschung (GSI), Plasmaphysik, D-64291 Darmstadt, Germany*

[2] *Department of Physics, Moscow State University, Moscow, 117822 Russia*

**e-mail: pikuz@mem3.phys.msu.su*

[3] *All-Russia Research Institute of Physicotechnical and Radioelectronic Measurements, Mendeleevo, Moscow region, 141570 Russia*

[4] *Associated Institute for High Temperatures, Russian Academy of Sciences, Moscow, 127412 Russia*

[5] *TU-Darmstadt, Institut für Kernphysik, 64289 Darmstadt, Germany*

Received August 5, 2003

Variation of the velocity of Ca^{6+} ions with initial energies of 5.9 and 11.4 MeV/nucleon has been experimentally studied in the course of ion stopping in a solid aerogel target. The method is based on measuring the Doppler shift in the *K*-shell spectrum of decelerated Ca^{19+} and Ca^{18+} ions. High spatial resolution (30–50 μm) in the direction of the ion beam propagation achieved simultaneously with high spectral resolution ($\lambda/\Delta\lambda$ = 1000–3000) in the X-ray wavelength interval of 2–4 Å allowed the ion beam dynamics in the solid target to be directly measured. By measuring variations in the relative intensity of spectral lines, it is possible to monitor the redistribution of the ions over charged states during their motion in the target. *© 2003 MAIK "Nauka/Interperiodica".*

PACS numbers: 79.20.Rf; 32.30.Rj; 34.50.Bw

1. Investigation of the process of interaction between heavy multicharge ions and solid targets or biological objects is currently an important task. The exact knowledge of characteristics such as the general stopping range and the ion velocity distribution at any point of the interaction volume is necessary both for better understanding of the physics of this process and for ion beam applications in thermonuclear synthesis [1], cancer therapy [2, 3], etc.

The time-of-flight methods used so far [4, 5] do not allow the dynamics of the process of ion stopping in a solid target to be directly observed. In order to solve this problem, we propose a new X-ray technique [6, 7] based on measuring the Doppler shift in the *K*-shell spectrum of ions decelerated in the target under conditions of high spatial resolution in the direction of ion beam propagation.

It should be noted that the effective charge of ions in the beam, which is an important basic characteristic, as well as the dynamics of variation of this quantity in the course of beam–solid interaction, can be calculated using the experimental data on the ion distribution over charged states and velocities in the target [1, 8].

A principal difficulty encountered in the investigation of ion beam stopping dynamics in solids is a very small stopping range (~50 μm) of ions in such targets, which poses strict requirements on the spatial resolution of the method and instrumentation. In connection with this, we suggest using aerogel targets—solids possessing extremely low density, which increases the ion stopping range and, hence, decreases the spatial resolution requirements to an acceptable limit.

2. Application of the proposed method to the investigation of solid aerogel targets has became possible due to the use of focusing X-ray spectrometers with spatial resolution, employing spherically bent crystals as X-ray dispersive elements [9]. These devices combine the geometric properties of a usual spherical mirror with the Bragg reflection properties of a crystal surface.

Based on focusing X-ray spectrometers with spatial resolution, we implemented a dispersion scheme successfully combining high spatial resolution ($\lambda/\Delta\lambda$ = 1000–3000) with high spatial resolution (30–50 μm) in the direction of the ion beam propagation. In addition, a high aperture ratio (brightness) of these spectrometers allowed variations in the relative intensity of spectral lines and, hence in the ion distribution over charged states in the course of stopping to be monitored during ion beam propagation in the target.

In order to calculate the ion velocity using the measured spectral shift, we used the well-known relation

taking into account both longitudinal and transverse Doppler effects:

$$\lambda_D = \lambda_0\left(\frac{1}{\sqrt{1-(v/c)^2}} + \frac{(v/c)\sin\varphi}{\sqrt{1-(v/c)^2}}\right) = \lambda_0(\Delta^t + \Delta^d). \quad (1)$$

Here, λ_D is the wavelength measured, λ_0 is the true wavelength of the ion transition, v is the velocity of impinging ions, c is the velocity of light, φ is the angle between the normal to the beam and the direction of observation, and Δ^t and Δ^d are the contributions of the transverse and longitudinal Doppler effects to the total line shift, respectively. The latter contributions vary depending on the position of the spectrometer, which noticeably modifies the shape of the spectrum measured. This technique is described in more detail elsewhere [6].

The proposed method provides data on relative ion velocities. Absolute values are obtained by calibrating to the beam velocity at the entrance of the radiating volume, which is assumed to be equal to the ion velocity in the beam extracted from an accelerator.

3. The experiments were performed on the UNILAC (GSI) linear accelerator of heavy ions (Darmstadt, Germany). The stopping dynamics were observed during the interaction of Ca^{6+} ions with SiO_2 (aerogel targets possessing a density of 0.15 g/cm^3 [10]) in a vacuum chamber at a pressure of 10^{-6} mbar. The incident ions with an energy of 5.9 or 11.4 MeV/nucleon were focused into a spot with a diameter of 1–2 mm on the edge face of a target positioned with a high-precision manipulator. Beam pulses had a duration of 1–3 ms, a current of 0.1–0.5e^- μA, and a repetition rate of ~3 Hz. The exposure time amounted to 5–7 h, during time which the X-ray radiation from the target was detected by a film (Kodak DEF). The film in the cassette was protected from UV radiation and visible light by two layers of 1-μm-thick polypropylene film with a 0.2-μm-thick aluminum metallization layer.

Figure 1 presents the experimental arrangement for observations in the direction perpendicular to the beam. These measurements were performed with a quartz crystal 11(–2)0 ($2d$ = 4.92 Å) with a curvature radius of R = 150 mm and a working area of 14 × 48 mm. The dispersion scheme was adjusted to operate in the first order of reflection for the measurement of $Ca^{19+}Ly_\alpha$ and $Ca^{18+}He_\alpha$ lines in a wavelength interval of 2.9–3.5 Å. The beam propagation direction x occurs in the plane of spatial resolution. Dashed contours in Fig. 1 indicate various possible positions of the spectrometers arranged at various angles relative to the ion beam.

4. We present the results of measurements of the velocity and charge redistribution between XX and XIX states for calcium ions in the beam stopped in the aerogel target. The observations were performed perpendicularly to the beam, in which case only the Δ^t component is nonvanishing in formula (1) and the line shape is influenced only by the transverse component of the Doppler shift.

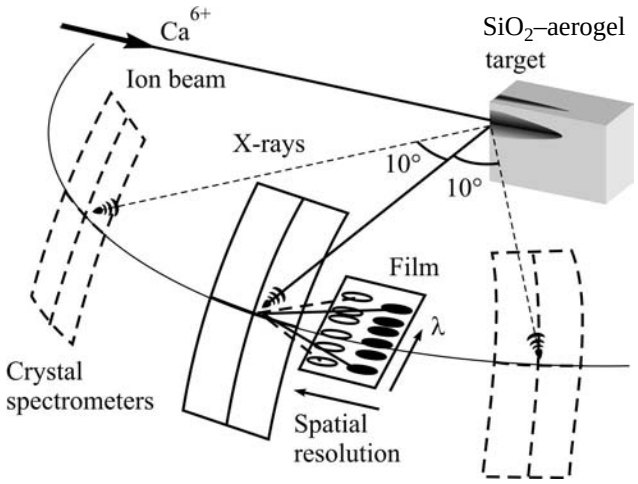

Fig. 1. The arrangement of the X-ray spectrometer for observations of the transverse Doppler shift. Dashed contours indicate the positions of spectrometers for the measurements with allowance of the longitudinal Doppler shift component.

Figure 2a illustrates the line shape formation and position. Being decelerated in the target, ions lose energy and this is reflected by a decrease in the Doppler shift with increasing depth of ion penetration into the target. Then, a sloped line is registered, provided that the spectrometer ensures spatial resolution in the ion beam propagation direction. It is known that a transverse shift accounts for the line shift toward increasing wavelength. In Fig. 2, the values of the Δ^t component and the corresponding wavelength characteristic of the beginning (input surface) and end of the radiating volume are indicated by subscripts 1 and 2, respectively.

Figure 2b shows the experimental results. The spectra display $CaLy_\alpha$ and $CaHe_\alpha$ transition lines to the K-shell, shifted toward longer wavelengths. The positions of nonshifted lines correspond to 3.0239 and 3.1769 Å, respectively. Switching the ion beam energy from 5.9 to 11.4 MeV/nucleon significantly changed the spectrum. An increase in the initial energy resulted in a greater wavelength shift and in a greater X-ray source size in the sagittal plane, which corresponds to an increase in the ion stopping range.

The measured part of the ion stopping range, during which the K-shell emission takes place, was 1.2 and 1.8 mm long (measured at 0.1 peak intensity level) for the incident ion energies of 5.9 and 11.4 MeV/nucleon, respectively. The accuracy of measuring these values, as determined by spatial resolution, falls within 50 μm.

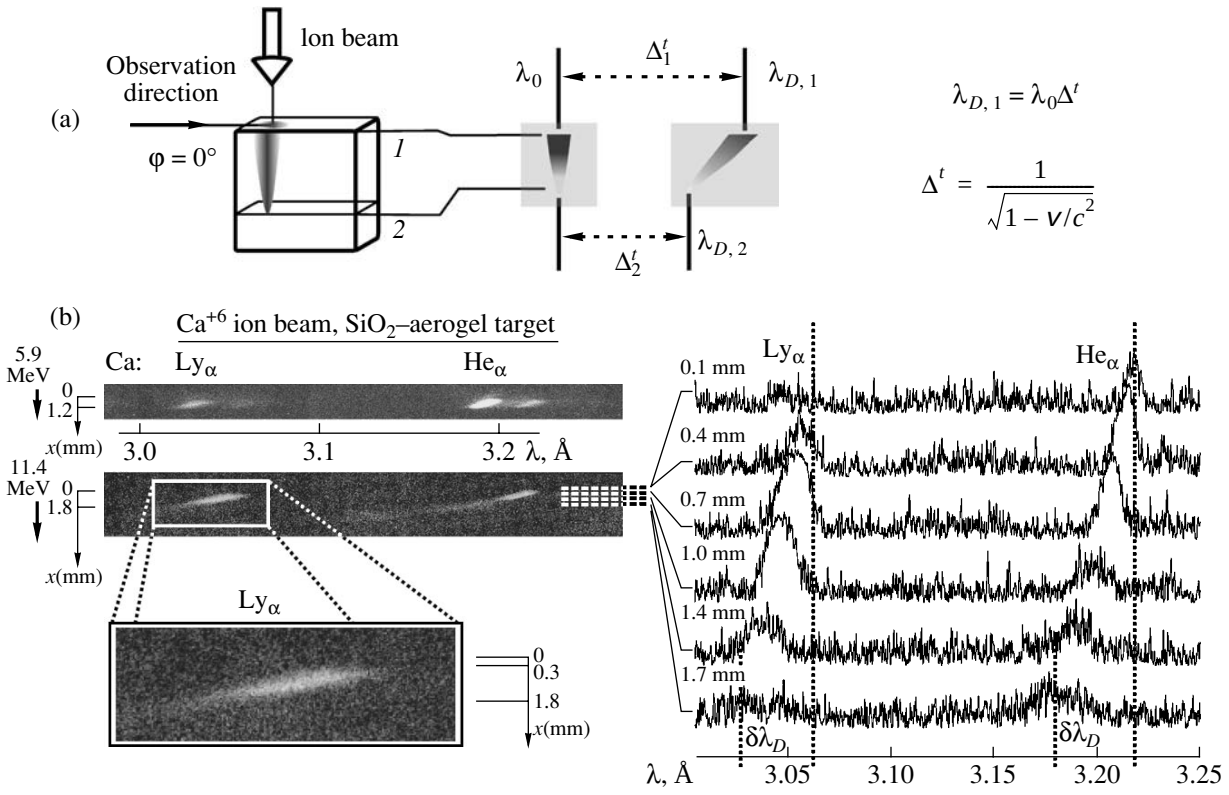

Fig. 2. Observations of the transverse Doppler shift: (a) a scheme illustrating the formation of shape and position of a spectral line with allowance of the Doppler effect; (b) the typical spectra and densitograms of the emission due to *K*-shell transitions in stopped Ca^{19+} and Ca^{18+} ions with the initial energies 5.9 and 11.4 MeV/nucleon.

Densitograms corresponding to various depths reflect the dynamics of the ion velocity variation in the course of stopping. Measuring the Doppler shift $\delta\lambda_D$ of the spectral line maximum at the observation point relative to that at the input surface and using formula (2), we calculate a change in the ion velocity relative to the initial value. Dashed lines in Fig. 2 indicate the total interval of observed shifts of the spectral lines. For calibrating the absolute values of ion velocities, it is assumed that the position of the He_α line peak in the densitogram of a 100-μm-thick surface layer corresponds to the emission from ions possessing an energy provided by the particle accelerator. This assumption is based on the fact that a 100-μm-thick layer of the aerogel target is equivalent in density to a 6-μm-thick layer of a continuous solid.

The accuracy of the ion velocity measurements, as determined by the spectral resolution, varies from 2 to 25% when the velocity changes from 0.16 to 0.06 of the velocity of light. Based on these considerations, we plotted experimental profiles of the velocity of H- and He-like calcium ions versus the depth of ion penetration into a target for the incident beam energy of 11.4 MeV/nucleon (Fig. 3a). From here, a velocity at which ions in the observed charged states cease to radiate amounts approximately equal to 6% of the velocity of light (which corresponds to 2.0 MeV/nucleon) can be determined. The results of numerical calculations for a continuous SiO_2 target [11] show that the electron cross section exhibits a sharp drop for an ion energy of 1.5–2.0 MeV/nucleon.

The results obtained in our experiments demonstrate that, owing to the high aperture ratio (brightness) of the spectrometers employed, it is possible to analyze the redistribution of ions over charged states by measuring relative intensities of the *K*-shell transitions in the spectra of differently charged ions.

Figure 3b shows variation of the relative intensity of Ly_α and He_α lines for Ca^{18+} and Ca^{19+} ions propagating in the target. As can be seen, the maximum concentrations of these ions are observed at a depth of 0.4 and 0.9 mm, respectively.

According to theoretical predictions, the maximum concentrations of high charged states must be observed in the initial subsurface region of the stopping range. The discrepancy that can be explained by the influence of internal boundaries present in the aerogel structure requires further investigations of related processes in model structured media. Further experimental investigation of the ion velocity and charge redistribution as functions of the penetration depth, supplemented with

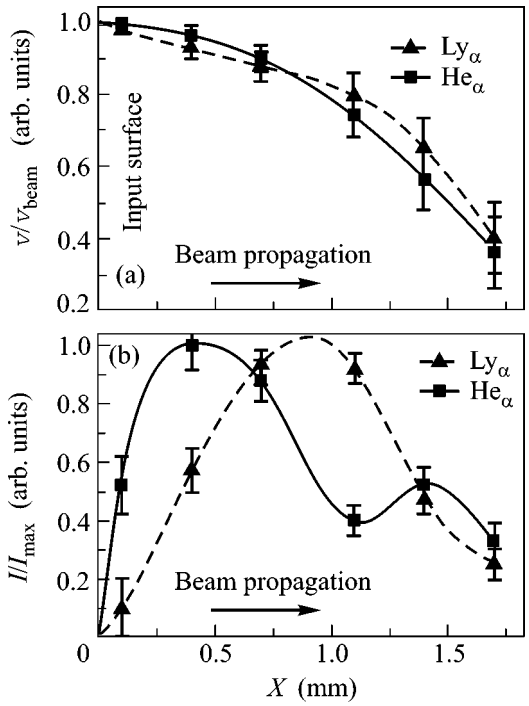

Fig. 3. Ion stopping dynamics in the aerogel target, showing (a) variation of the velocities and (b) redistribution over charged states for the Ca^{19+} and Ca^{18+} depending on the penetration depth.

theoretical description of these processes, are important tasks for future research.

In order to provide for a more precise calibration, we suggest introducing reference lines in the spectrum by irradiating specially selected targets with electron beams generated by electron guns. The targets should be selected so that the emission from ionized ions would fall within the wavelength range of stopped ions. Another variant is offered by an experimental geometry implementing two identical spectrometers arranged at various observation angles, with comparative analysis of the results of simultaneous measurements. The pattern of characteristic spectra measured in such a configuration is depicted in Fig. 4. The value of 5.6 MeV per nucleon obtained from these data coincides to within 5% with the beam energy measured by the standard method.

5. To summarize, we have directly measured the variation of velocity and redistribution over charged states in an ion beam stopped inside a solid target. The dynamics of ion stopping were observed due to the implementation of high-brightness X-ray diagnostics at high spectral and spatial resolution and due to the use of solid aerogel (SiO_2) targets of low density (0.15 g/cm^3).

We determined the velocity profiles of Ca^{19+} and Ca^{18+} ions at target depth in the velocity interval from 0.16 to 0.06 of the velocity of light. The dynamics of ion stopping for both charged states coincide to within the experimental error. For a Ca^{6+} ion beam with the initial energies 5.9 and 11.4 MeV per nucleon, the experimentally determined ion stopping range is 1.2 and 1.8 mm, respectively.

We have detected a redistribution of charged states by measuring relative intensities of the corresponding spectral lines. The maximum concentrations of H- and He-like calcium ions are observed at a depth of 0.9 and 0.4 mm, respectively, which indicates that the process

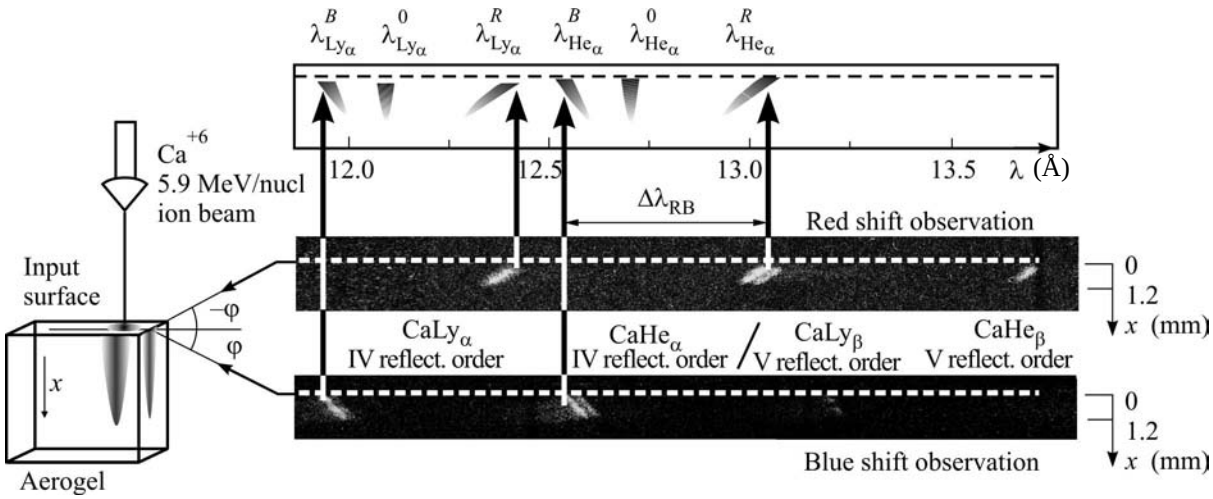

Fig. 4. The results of measurements with allowance of the longitudinal Doppler shift component for two identical spectrometers arranged symmetrically (±10°) relative to the normal to the ion beam. The ion velocities were determined using a difference $\Delta\lambda_{RB}$ between the results of the red and blue shift observations.

of ionization for ions stopped in the aerogel target continues up to a depth of about 1 mm.

REFERENCES

1. S. P. Ahlen, Rev. Mod. Phys. **52**, 121 (1980).
2. G. Kraft, Prog. Part. Nucl. Phys. **45**, 473 (2000).
3. N. O. Lassen, K. Dan. Vidensk. Selsk. Mat. Fys. Medd. **28**, 7 (1954).
4. A. Golubev, V. Turtikov, A. Fertman, *et al.*, Nucl. Instrum. Methods Phys. Res. A **464**, 247 (2001).
5. N. Shiomi-Tsuda, N. Sakamoto, H. Ogawa, *et al.*, Nucl. Instrum. Methods Phys. Res. B **135**, 118 (1998).
6. O. N. Rosmej, S. A. Pikuz, Jr., J. Wieser, *et al.*, Rev. Sci. Instrum. (in press).
7. O. N. Rosmej, J. Wieser, M. Geissel, *et al.*, Nucl. Instrum. Methods Phys. Res. A **495**, 219 (2002).
8. H. D. Betz, Appl. At. Collision Phys. **4**, 1 (1983).
9. A. Ya. Faenov, S. A. Pikuz, A. I. Erko, *et al.*, Phys. Scr. **50**, 333 (1994).
10. N. G. Borisenko and Ya. A. Merkuliev, Proc. P.N. Lebedev Phys. Inst. **221** (1996).
11. O. Rosmej, Th. Stohlker, V. P. Shevelko, and I. Yu. Tolstikhina, GSI Annual Report (2001), p. 125.

Translated by P. Pozdeev

JETP Letters, Vol. 78, No. 6, 2003, pp. 379–383. Translated from Pis'ma v Zhurnal Éksperimental'noĭ i Teoreticheskoĭ Fiziki, Vol. 78, No. 6, 2003, pp. 832–836.
Original Russian Text Copyright © 2003 by Kosse, Kuzovlev, Levchenko, Medvedev, Prokhorov, Khokhlov, Mikheenko.

Geometrical Surface Vortex Pinning in Superconducting Films

A. I. Kosse[1], Yu. E. Kuzovlev[1]*, G. G. Levchenko[1], Yu. V. Medvedev[1], A. Yu. Prokhorov[1], V. A. Khokhlov[1], and P. N. Mikheenko[2]

[1] *Galkin Physics and Technology Institute, Donetsk, National Academy of Sciences of Ukraine, Donetsk, 83114 Ukraine*
**e-mail: kuzovlev@kinetic.ac.donetsk.ua*
[2] *School of Physics and Astronomy, University of Birmingham, Edgbaston, Birmingham B152TT, UK*
Received July 23, 2003; in final form, August 12, 2003

A model is proposed for vortex pinning in a superconducting film with a rough surface. The model relates the critical current to the steepness of the surface relief and, at a high vortex concentration, to the distance between neighboring steepness maxima on the paths of vortex motion. The dependence of the critical current density on the thickness of a high-T_c superconducting film is measured in a weak magnetic field. Its behavior can be explained by the pinning at the stepped surface relief. © *2003 MAIK "Nauka/Interperiodica".*

PACS numbers: 74.78.-w; 74.25.Sv; 74.25.Qt

1. It is well known that, in good (continuous) superconducting films, the critical current density decreases as the film thickness increases (see, e.g., [1]). There is reason to assign this effect to the surface pinning (see, e.g., [2, 3]). Namely, if the latter predominates over the bulk pinning, it should balance the Lorentz force, which acts over the entire length of the vortex line, i.e., is proportional to the integral of the current density over the thickness. As a result, the effective (mean) critical current density J_c is inversely proportional to the film thickness D. However, there is no theoretical model that accounts for the value of the critical current and the character of its decrease with increasing vortex concentration (approximately, as the inverse square root of the concentration [4]). The existing theory [2] provides no estimate for the critical current level and, in addition, it assumes that the vortex concentration is high (so that the distance between vortices is much smaller than D).

This paper reports the results of measuring the dependence $J_c(D)$ for high-T_c superconducting films in magnetic fields below 1 Oe, i.e., in the conditions of a sparse vortex system, to which the formulas derived in [2] do not apply. The studies of the film surface showed that it consists of terraces whose heights are multiples of the unit-cell height.

A model proposed in this work for the vortex pinning by the surface roughness is the simplest in the sense that the vortices are described in the London approximation and the superconductor is assumed to be isotropic and homogeneous (the latter means that the bulk pinning by the random potential of structural inhomogeneities is ignored). The interpretation of the experimental results in terms of our model shows that the measured critical current corresponds to the pinning at the edges of the surface terraces.

2. In Fig. 1, the empty circles correspond to the critical current density at a temperature of 77 K for four YBaCu films of different thickness. The films belong to the same series grown on the $SrTiO_3$ substrates by laser ablation. The critical temperatures of the films were close to 86 K. The value of J_c was obtained from the complex susceptibility of the films, which was measured in an alternating field $H_{ac} \leq 0.8$ Oe with a frequency of 10 kHz in the absence of a bias field (more precisely, in the terrestrial magnetic field). The experimental technique and the method of determining J_c were described in [5, 6]. The curve shown in Fig. 1 represents the theoretical dependence $J_c(D)$ derived below.

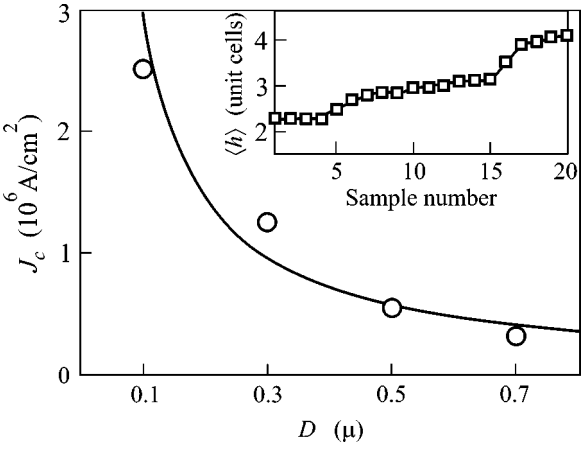

Fig. 1. Experimental (empty circles) and theoretical (solid line) dependences of the critical current density J_c of YBaCu films on their thickness D. The inset is explained in the main body of the paper (Section 2).

0021-3640/03/7806-0379$24.00 © 2003 MAIK "Nauka/Interperiodica"

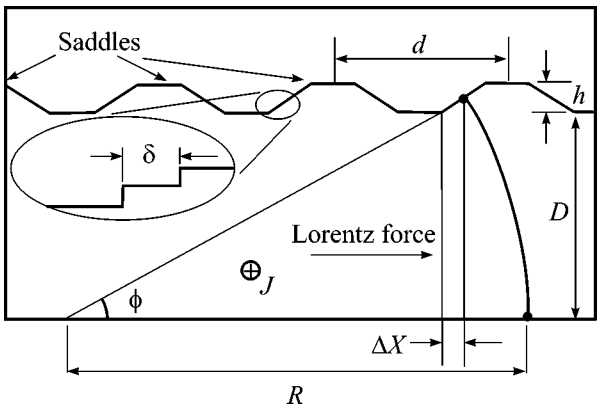

Fig. 2. Schematic representation of the film cross section along a chain of minima and saddles of the surface relief by the *XZ* plane that is perpendicular to the current direction. The thick line represents the configuration of a vortex core ascending the saddle.

Using atomic force microscopy, we studied the surfaces of 20 films which had the same thickness of 100 nm and were grown under similar conditions. The inset in Fig. 1 shows the average step height $\langle h \rangle$ of the surface relief in units of unit-cell height versus the sample number in order of increasing $\langle h \rangle$. Despite averaging, these data clearly demonstrate the stepped structure of the surface relief (also observed in, e.g., [4, 7]).

3. A simple surface pinning mechanism is quite evident. Vortices intersecting the surface roughness are forced to locally increase their length and, hence, their energy. As a result, the surface roughness gives rise to a potential barrier network. Let us analyze the efficiency of this mechanism.

Let the film lie in the *XY* plane and let a (transport or Meissner) supercurrent flow through the film along the *Y* axis, so that it moves the vortices (which "pierce" the film) in the *X* direction. Surface corrugation transverse to the current would not lead to the vortex pinning. For this reason, we consider a film with a surface corrugated transverse to the vortex motion, as shown in Fig. 2. Evidently, the maxima of the model relief shown in Fig. 2 must be identified not with the maxima of the actual two-dimensional roughness but with its saddle points (maxima in *X* for the minima in *Y*). Correspondingly, ϕ is the characteristic angle of ascending to the saddles. Further, we assume that the condition $h \ll \lambda$ is satisfied, where λ is the penetration depth and *h* is the saddle height. The ratio of *h* to the minimal thickness *D* (see Fig. 2) is not necessarily small, and, therefore, we introduce the mean thickness $\bar{D} = D + h/2$. In the case of a layered high-T_c superconductor film with the axis $C \parallel Z$, the quantity λ should be interpreted as $\lambda_{a,b}$.

Since vortex bending in the *YZ* plane is energetically unfavorable, the vortex core lies in the *XZ* plane; i.e., it can be parametrized by a certain function $x = X(z)$. If the surface relief is given by the function $z = Z(x)$ and the current density is denoted as $J = J(x, z)$, the vortex–current interaction energy is expressed as

$$E_i = -\frac{\Phi_0}{c} \iint\limits_{\substack{x < X(z) \\ 0 < z < Z(x)}} J(x, z)\,dx\,dz + \text{const} \qquad (1)$$

(the general expression for E_i was discussed in [8, 9]). Under the condition $h \ll \lambda$, the current is virtually independent of *x* and remains constant in the roughness region:

$$J(x, z) \approx \bar{J}\cosh\left(\frac{z - \bar{D}/2}{\lambda}\right)\left[\frac{2\lambda}{\bar{D}}\sinh\frac{\bar{D}}{2\lambda}\right]^{-1}, \qquad (2)$$

where $\bar{J}$ is the mean current density (the relative correction to Eq. (2) caused by the roughness does not exceed $\sim h\min(D, \lambda)/4\lambda^2$).

Exact expressions for the self-energy E_s of Abrikosov vortex in a film (plate) of an arbitrary thickness can be obtained from the formulas presented in [10, 8]. We use the "local approximation" for the self-action of a bent vortex. Within the framework of this approximation, the energy E_s is proportional to the vortex core length *L*:

$$E_s \approx \epsilon L + E_e, \quad \epsilon \approx \frac{\Phi_0 H_{c1}}{4\pi} \approx \left(\frac{\Phi_0}{4\pi\lambda}\right)^2 \ln\frac{\lambda}{\xi}. \qquad (3)$$

Here, ϵ is the vortex elasticity (energy per unit core length); E_e is the energy of vortex ends [8], i.e., the energy of the vortex magnetic field outside the superconductor (its value is approximately constant); and other notation is standard. This approximation was used (see, e.g., [2, 8, 9, 11, 12]) starting at least with [13]. Computer calculations confirm that its error does not exceed a few percent even when the core curvature radius is small, $R \sim 0.1\lambda$ [9].

Equations describing the evolution of curved vortices were considered in [9]. We are interested only in the stationary states of a plane-curved vortex. In such a state, the sum of all forces acting on the core is zero, $\delta E/\delta X = 0$, where $E = E_s + E_i$ is the total vortex energy. Let us introduce the characteristic current-density scale:

$$J_{c1} = cH_{c1}/4\pi\lambda = c\epsilon/\Phi_0\lambda.$$

In approximation (3), we obtain

$$\frac{\delta E}{\delta X} = \frac{\epsilon}{\lambda}\left(\frac{\lambda}{R} - \frac{J}{J_{c1}}\right), \quad \frac{1}{R} \equiv -\frac{X''}{(1 + X'^2)^{3/2}}. \qquad (4)$$

Here, $R = R(t, z)$ is the local curvature radius of the core (its positive values correspond to the rightward convex of the core) and the prime denotes differentiation with respect to *z*: $X' \equiv \partial X/\partial z$, $X'' \equiv \partial^2 X/\partial z^2$. The boundary conditions to the equation $\delta E/\delta X = 0$ consist in that the core be perpendicular to the surface at the points where it reaches the surface [13] (this is a result of the interac-

tion of the core ends with their reflections in the superconductor boundary, i.e., with the deformation of the vortex self-current lines near the boundary [9]).

For the stationary configuration, Eq. (4) with the substitution of Eq. (2) and integration with respect to z yields

$$-\frac{X'(Z)}{\sqrt{1+X'^2(Z)}} = \frac{\bar{J}}{J_{c1}}\frac{\bar{D}}{\lambda}\left[1+\frac{Z-\bar{D}}{2\lambda}\tanh^{-1}\left(\frac{\bar{D}}{2\lambda}\right)\right]. \quad (5)$$

Here, Z is the z coordinate of the core intersection with the upper (corrugated) surface. The expression takes into account that $|Z - \bar{D}| \ll \lambda$, because h is small. By virtue of the aforementioned boundary conditions, we have $X'(0) = 0$ at the lower (flat) surface. As for the upper surface, the left-hand side of Eq. (5) can be reduced to the form:

$$-X'(Z)/\sqrt{1+X'^2(Z)} = \sin\phi(Z), \quad (6)$$

where $\phi(Z)$ is the roughness slope at the point of core intersection with the surface. Equation (5) has solutions only when the mean current density is sufficiently small: $\bar{J} < J_c$. If the relief of saddle chain is described by a smooth function $Z(x)$, the desired root of Eq. (5) lies between the levels D and $z_0 = Z(x_0)$, where x_0 is the inflection point of $Z(x)$. From Eqs. (5) and (6), we obtain the following estimate of the critical current density J_c for both thick ($\bar{D} \gtrsim \lambda$) and thin ($\bar{D} \ll \lambda$) films:

$$J_c \approx \frac{\lambda J_{c1}}{\bar{D}}\sin\phi_{\max}, \quad (7)$$

where $\phi_{\max}$ is the maximal saddle slope (at the inflection point).

4. For illustration, we consider a piecewise linear relief shown in Fig. 2 for the case of a thin film ($D \lesssim \lambda$), where $J \approx$ const. Then, the equality $\delta E/\delta X = 0$ means that the core of a pinned vortex has the form of a segment of a circle with radius

$$R = R_{\text{stac}} \equiv \lambda J_{c1}/J. \quad (8)$$

The upper end of the core is exactly at the base of the slope, i.e., $\Delta X = 0$ in Fig. 2. In fact, from the orthogonality of the core to the surface and from simple geometric considerations (see Fig. 2), it follows that, in the case of a displacement $\Delta X > 0$, the curvature radius of the core should be equal to

$$R = R_c + \frac{\Delta X}{\cos\phi}, \quad R_c \equiv \frac{D}{\sin\phi}, \quad (9)$$

i.e., it should differ from radius (8). One can readily see that vortex pinning becomes impossible if the radius R_{stac}, when decreasing with growing J, becomes equal to R_c. Then, for the critical current density, we obtain

$$J_c = \frac{\lambda J_{c1}}{R_c} = \frac{\epsilon c}{\Phi_0 D}\sin\phi. \quad (10)$$

To verify the above statements, we calculate the energy difference ΔE between the pinning state characterized by radius (8) and zero displacement $\Delta X = 0$ and the depinning state with radius (9) and a small positive displacement $\Delta X > 0$. Simple calculations give

$$\Delta E = \frac{\epsilon D}{2}\left[(2-j)\frac{\phi}{\sin\phi} - \frac{\arcsin(j\sin\phi)}{j\sin\phi} + j\cos\phi - (1-j^2\sin^2\phi)^{1/2}\right] + \epsilon\phi(1-j)\frac{\Delta X}{\cos\phi} + O(\Delta X^2), \quad j \equiv \frac{J}{J_c}, \quad (11)$$

where J_c is given by Eq. (10). The ΔX-independent part of ΔE (two first lines in Eq. (11)) represents the potential barrier between the pinning state and the critical state with the radius of curvature R_c and zero displacement (in the case of a smooth relief, the critical state corresponds to the situation where the core intersects the surface at the inflection point of $Z(x)$). The ΔX-dependent part of ΔE represents the barrier between the critical state and the depinning state. Both ΔE components are positive if the current density is smaller than its critical value given by Eq. (10), and they become equal to zero at $J = J_c$. Hence, when $J < J_c$, state (8) corresponds to the local minimum of the total energy functional and, therefore, is stable.

The application of Eq. (5) to the given relief shows that Eq. (10) is also valid for a thick film. In any case, one can see that the critical current density is inversely proportional to the effective thickness. The latter may take on any value between D and $D + h$, depending on the type of roughness.

5. The interaction of vortices is essential if their number is greater than the number of valleys in the surface relief, i.e., if

$$N \equiv nd^2 = B_z d^2/\Phi_0 \gtrsim 1, \quad (12)$$

where n is the vortex concentration and B_z is the corresponding magnetic induction. The problem of collective pinning by real roughnesses is nontrivial, because the vortex lattice is inhomogeneous in all three coordinates. Here, we only consider the following estimate.

We assume that the film is divided into cells with length d and area d^2, which are bounded along the X axis by the neighboring saddles (see Fig. 2), along the Y axis, by similar saddles, while the corners of the cells correspond to the relief peaks. Evidently, $\sim N$ vortices occurring in the cell form $\sim\sqrt{N}$ rows with $\sim\sqrt{N}$ vortices in each of them. In the presence of pinning, only the extreme (right-most) vortex of each row is pinned to the potential barrier (saddle), while the inner vortices are held by it. The latter means that the force with which the extreme vortices act on the inner ones compensates the transport current force. If the extreme vortices had the same configuration as the inner ones, they would

have experienced a counteracting force of approximately the same magnitude. Consequently, in the vicinity of the extreme vortex core, in addition to the current J, an extra current whose average value is about $J\sqrt{N}$ flows in the same direction. Therefore, the configuration of the extreme vortex is determined by the total current $J_{\text{sum}} \approx J + J\sqrt{N}$ (as well as by the geometry of the obstacle). The pinning is possible unless the Lorentz force caused by this current is smaller than the elastic force due to the distortion and stretching of the core.

Thus, to estimate the critical current, we return to the previous consideration by replacing J by J_{sum}. As a result, we obtain

$$J_c \approx \frac{\epsilon c}{\Phi_0 D}\frac{\sin\phi}{1 + d\sqrt{B_z/\Phi_0}}. \qquad (13)$$

Here, we ignored the effect of the vortices from other cells, which is possible when the distribution of B_z is macroscopically homogeneous and the currents of these vortices in a given cell compensate each other. If the homogeneity is violated, the local pinning condition will have the form

$$|J + J_{nu}| < J_c, \quad J_{nu} \approx -(c/4\pi)\partial B_z/\partial x,$$

where J_{nu} is the inhomogeneity-caused addition to the local current density.

6. The situation becomes different when the steepness of the relief has several maxima, e.g., when the ascent to a saddle consists of several steps (see the inset in Fig. 2). Then, a vortex row may fall into several trains, each of which is pinned by one of the steps. In this case, the angle determining the pinning force is actually close to 90°. Correspondingly, in estimates (13), (7), and (10), $\sin\phi$ should be replaced by unity and the length scale d should be replaced by the typical step width δ (see the inset in Fig. 2). The average slope of the ascent will be indirectly included in the result through δ.

Strictly speaking, real steps (see above) are too small to trust the London approximation. However, one can expect that, in any more adequate theory, the possibility of an easy exit of the vortex magnetic flux through the gap between an undistorted superconducting plane and a plane interrupted by a step will cause the vortex line (the phase singularity line of the order parameter) to bend approximately in the same way as in the situation considered above. Then, the estimates given above should remain valid.

It is important to note that a small step height does not lead to a smallness of the depinning potential barrier, because the process is determined by the interplay of the whole core length and the whole film thickness. For a step, according to Eq. (11), we can write

$$\Delta E(\phi = 90°) > (\pi/2 - 1)\epsilon D(1 - J/J_c)^{3/2}, \qquad (14)$$

i.e., the barrier height is determined by an energy scale that is giant in terms of temperature units: $\epsilon D \sim 10^4$–10^7 K. The quantity given by formula (14) may even exceed the barrier of the bulk pinning by line defects threading the film (see, e.g., [12]).

At the same time, unlike the bulk pinning, surface pinning does not require any rigid fixation of the core. The amplitude of core deformations that may occur at pinning by steps is comparable with D, i.e., almost always much greater than the amplitude of thermal fluctuations of the core, $\delta X \sim \sqrt{TD/\epsilon}$, where T is temperature (this estimate can easily be obtained in terms of approximation (3)). This means that the difference between the configuration entropies of the core in the states under the barrier and beyond the barrier is not as great as in the case of the pinning by line defects. Hence, the surface pinning must be less affected by depinning due to thermal fluctuations (the entropy instability [12]).

7. Comparing the theory and the experiment, it is worthwhile to take into account the possibility of one or another correlation between the film thickness and the film surface structure, specifically, between the parameters d and ϕ or δ. Otherwise (without information on the steepness of the surface relief) an unambiguous comparison of the theoretical and experimental dependences of J_c on D is impossible. Since the actual relief is random, a question arises: what statistical meaning should be ascribed to the aforementioned parameters? The most suitable answer seems to be one in terms of the percolation theory: ϕ is the minimal angle (d or δ is the maximal width) such that the saddles with smaller slope angles (greater widths) form a continuous network of paths (an infinite cluster).

One should also take into account violations of film continuity, which are possible in thin films with $D <$ 100 nm (see [1]) and may cause changes in the effective values of d or δ. In addition, if the bulk pinning is considerable (e.g., pinning by dislocations or pores), its contribution should be included in the theoretical estimates of J_c when comparing them with the experiment. According to Eq. (10), if J_c is much greater than $\epsilon c/\Phi_0 D$, such a contribution must be present.

In our case (see Section 2), the parameters d and/or δ drop out of consideration. Judging from the microscopy data, thin and thick films had approximately the same structure and surface quality. Hence, we can use formula (10). The solid line in Fig. 1 showing the theoretical dependence of J_c on D was plotted using this formula at $\lambda/\xi = 90°$ and $\sin\phi/\lambda^2 = 4.8$, where λ is in microns. From the latter equality, substituting the estimate of the penetration depth $\lambda \approx 0.45$ μm at $T = 77$ K and $T_c = 86$ K, we obtain $\sin\phi \approx 1$.

8. Thus, we showed that the critical current of an individual surface pinning is determined by the elasticity of the vortex line and the angle of ascent of the elevations (saddles) of the surface relief. For collective

pinning in a dense vortex system, the number of vortices in a train pinned by one elevation is also essential. The maximal effect is achieved at a stepped relief, while the potential barrier of depinning is governed by the film thickness and is independent of the step height.

The comparison of theory and experiment (illustrated in Fig. 1) and the above discussion suggest the following conclusions: first, the theory and the experiment prove to be in good agreement, and, second, the level of the measured critical current can be understood in terms of the geometric surface pinning by stepped relief without considering the bulk pinning.

This result justifies the neglect of the internal inhomogeneity of the film in our consideration. At the same time, it underlines the topicality of studying the interaction of surface and bulk pinning mechanisms (in this connection, see, e.g., [3]).

REFERENCES

1. E. Sheriff, R. Prozorov, Y. Yeshurun, *et al.*, J. Appl. Phys. **82**, 4417 (1997).
2. R. Prozorov, E. B. Sonin, E. Sheriff, *et al.*, Phys. Rev. B **57**, 13845 (1998).
3. M. V. Indenbom, M. Konczykowski, C. J. van der Beek, and F. Holtzberg, Physica C (Amsterdam) **341–348**, 1251 (2000).
4. B. Dam, J. M. Huijbregtse, F. C. Klaassen, *et al.*, Nature **399**, 439 (1999).
5. A. M. Grishin, V. F. Drobot'ko, V. D. Stasovskiĭ, and V. A. Khokhlov, Zh. Tekh. Fiz. **63** (8), 190 (1993) [Tech. Phys. **38**, 730 (1993)].
6. V. A. Khokhlov, V. V. Krzhizhanovskiĭ, A. Yu. Prokhorov, *et al.*, Fiz. Tverd. Tela (St. Petersburg) **43**, 1541 (2001) [Phys. Solid State **43**, 1603 (2001)].
7. J. Summhammer, K. Kundzins, G. S. Hosseinali, *et al.*, Physica C (Amsterdam) **242**, 127 (1995).
8. Yu. E. Kuzovlev, Physica C (Amsterdam) **292**, 117 (1997).
9. Yu. E. Kuzovlev, cond-mat/9904012.
10. Yu. E. Kuzovlev and A. I. Lomtev, Zh. Éksp. Teor. Fiz. **111**, 1803 (1997) [JETP **84**, 986 (1997)].
11. L. P. Gor'kov and N. B. Kopnin, Usp. Fiz. Nauk **116**, 413 (1975) [Sov. Phys. Usp. **18**, 496 (1975)].
12. A. Kramer and M. L. Kulic, Phys. Rev. B **48**, 9673 (1993).
13. V. P. Galaĭko, Zh. Éksp. Teor. Fiz. **50**, 1322 (1966) [Sov. Phys. JETP **23**, 878 (1966)].

Translated by E. Golyamina

JETP Letters, Vol. 78, No. 6, 2003, pp. 384–388. From Pis'ma v Zhurnal Éksperimental'noĭ i Teoreticheskoĭ Fiziki, Vol. 78, No. 6, 2003, pp. 837–840.
Original English Text Copyright © 2003 by Matveenko.

Stripes and Superconductivity in a One-Dimensional Self-Consistent Model¶

S. I. Matveenko

Landau Institute for Theoretical Physics, Russian Academy of Sciences, Moscow, 119334 Russia

e-mail: matveen@landau.ac.ru

Received August 14, 2003

We show that many observable properties of high-temperature superconductors can be obtained in the framework of a one-dimensional self-consistent model with included superconducting correlations. Analytical solutions for spin, charge, and superconductivity order parameters are found. The ground state of the model at low hole doping is a spin–charge solitonic superstructure. Increased doping leads to a transition to the superconducting phase. There is a region of doping where superconductivity, spin density wave, and charged stripe structure coexist. The charge density modulation appears in the vicinity of vortices (kinks in the 1D model) in the superconducting state. © *2003 MAIK "Nauka/Interperiodica".*

PACS numbers: 74.20.Mn; 75.30.Fv; 74.25.Qt; 72.15.Nj

Recently discovered stripe phases in doped antiferromagnets (cuprates and nickelates) [1] have attracted attention to the problem of coupled spin and charge order parameters in the electron systems. Theoretical [2–5] and experimental [6–10] evidences indicate the possibility that their ground state exhibits spin and charge density waves (SDW and CDW), either competing, or coexisting with superconductivity. Numerical mean-field calculations [2–4] suggest a universality of the spin–charge multimode coupling phenomenon in repulsive electronic systems of different dimensionalities. Families of the cuprate high-transition-temperature superconductors show antiferromagnetism and superconductivity. For the $La_{2-x}Sr_xCuO_4$ family, there is another ordering tendency—unidirectional charge–spin density waves, i.e., "stripes." The recent neutron scattering experiment of Lake *et al.* [6] shows that moderate magnetic field makes fluctuating stripes quasistatic. An important development in the theory of the cuprate superconductors is the prediction that, in addition to antiferromagnetism and superconductivity, there is a tendency toward stripe ordering [2–4]. This prediction is corroborated by experiments [1, 11]. A recent neutron scattering experiment shows that a moderate magnetic field can turn a fluctuating stripe order into a quasi-static one in optimum doped cuprates [7]. The vortex state can be regarded as an inhomogeneous mixture of a superconducting spin fluid and a material containing a nearly ordered antiferromagnet.

In this paper, we present the one-dimensional effective model describing stripe phase at low hole doping and superconductivity state at higher doping. An exact analytical solution of the Hartree–Fock problem at and away from the half-filling is found. Our theory predicts an amazing duality between the spin density wave and superconducting order, and implies the presence of stripes near a superconducting vortex, and superconductivity near a stripe dislocation.

The Hamiltonian $H = H_0 + H_s$ consists of two parts: the Hubbard Hamiltonian with on-site repulsion $U > 0$:

$$H_0 = -t\sum_{\langle i,j\rangle\sigma} c^\dagger_{i,\sigma}c_{j,\sigma} + U\sum_i \hat{n}_{i,\uparrow}\hat{n}_{i,\downarrow} - \mu\sum_{i,\sigma}\hat{n}_{i,\sigma}, \quad (1)$$

and the interaction part including superconducting correlations

$$H_s = \sum_i \Delta_s(i)c^\dagger_{i,\uparrow}c^\dagger_{i,\downarrow} + \text{h.c.}, \quad (2)$$

where Δ_s is the superconducting order parameter and μ is the chemical potential. The case of the Hubbard model (1) was considered in detail earlier [12]. The self-consistent analytical solution for the charge–spin solitonic superstructure was found to be a function of hole doping. It was shown that effects of commensurability led to a pinning of stripe structure at rational filling points $|\rho - 1| = m/n$.

In the continual self-consistent approximation, the effective Hamiltonian can be derived similarly [12]. We obtain

$$H = \int dx\left\{\Psi^\dagger_\sigma\left(-i\frac{\partial}{\partial x}\right)\hat{\sigma}_z\Psi_\sigma + \Delta(x)\Psi^\dagger_\sigma\hat{\sigma}_+\Psi_\sigma\right.$$

¶This article was submitted by the author in English.

0021-3640/03/7806-0384$24.00 © 2003 MAIK "Nauka/Interperiodica"

$$+\Delta^*(x)\Psi_\sigma^\dagger\hat{\sigma}_-\Psi_\sigma+\alpha\rho(x)\Psi_\sigma^\dagger\Psi_\sigma$$
$$+\Delta_s(-\Psi_{+,\uparrow}^\dagger\Psi_{-,\downarrow}^\dagger+\Psi_{-,\uparrow}^\dagger\Psi_{+,\downarrow}^\dagger) \quad (3)$$
$$+\Delta_s^*(-\Psi_{-,\downarrow}\Psi_{+,\uparrow}+\Psi_{+,\downarrow}\Psi_{-,\uparrow})$$

$$+\frac{|\Delta|^2}{\pi\lambda}+\frac{|\Delta|_s^2}{\pi\lambda_s}-\frac{\alpha}{2}\rho^2\Big\},$$

where $\lambda = 2\alpha/\pi$ is a dimensionless spin coupling constant, λ_s is a dimensionless superconductor coupling constant, $\hat{\sigma}_{z,x}$ are the Pauli matrices, $2\hat{\sigma}_\pm = \hat{\sigma}_x \pm \hat{\sigma}_y$, $\alpha = U/4t$; the Plank constant is taken as unity, and the length is measured in the units of the lattice (chain) period a. In these units, momentum and wave vector are dimensionless, and velocity and energy possess one and the same dimensionality. The vector $\Psi_\sigma^T \equiv (\Psi_{\sigma+}, \Psi_{\sigma-})$ is defined in terms of the right–left-moving $\Psi_{\sigma\pm}$, which constitute the wave function

$$\Psi_\sigma(x) = \Psi_{+,\sigma}e^{ik_Fx}+\sigma\Psi_{-,\sigma}e^{-ik_Fx}, \quad (4)$$

where $\sigma = \pm 1$ for a spin $\uparrow$ and $\downarrow$, respectively. The Fermi-momentum is $k_F = \pi\bar{\rho}/2$, where, in the case of half-filling, the average number of electrons per site equals $\bar{\rho} = 1$, i.e., $k_F = \pi/2$. The slowly varying real functions $\Delta(x)$ and $\rho(x)$ are defined as $\langle\hat{n}(x)\rangle = \rho(x)$, $\langle\hat{S}^z(x)\rangle = -\Delta(x)\cos(\pi x)/\alpha$. The continual approximation requires that $\alpha, \lambda, \lambda_s \ll 1$ (weak coupling limit). Note that the constraint $\lambda = 2\alpha/\pi$ for the Hubbard model is not necessary in a general case, our results remain valid for independent $\alpha, \lambda, \lambda_s \ll 1$.

Introduce $\bar{\rho}$ and $\tilde{\rho}$ as $\rho(x) = \bar{\rho} + \tilde{\rho}(x)$, $\int\tilde{\rho}(x)dx = 0$. Then, the term $\alpha\bar{\rho}\Psi^\dagger\Psi$ in Eq. (3) is the shift of the chemical potential or the energy, and the term $\alpha\tilde{\rho}\Psi^\dagger\Psi$ can be excluded by the unitary transformation (see [12, 13])

$$\Psi_\pm(x) \longrightarrow \exp\left(\mp i\alpha\int^x\tilde{\rho}dx'\right)\Psi_\pm(x).$$

Under this transformation, the spin order parameter modifies as $\Delta(x) \longrightarrow \exp(2i\alpha\int^x\tilde{\rho}dx')\Delta(x)$.

We can diagonalize the total Hamiltonian $H = H_0 + H_s$ by performing unitary Bogoliubov transformations

$$\Psi_\sigma(x) = \sum_n\gamma_{n,\sigma}u_{n,\sigma}(x)-\sigma\gamma_{n,-\sigma}^+v_{n,-\sigma}^*(x), \quad (5)$$

which have the form

$$\Psi_{\pm,\sigma} = \sum_n\gamma_{n,\sigma}u_\pm \pm \gamma_{n,-\sigma}^+v_\mp^* \quad (6)$$

in terms of right and left components $u_\pm$, $v_\pm$ defined as

$$f_\sigma(x) = f_{+,\sigma}e^{ik_Fx}+\sigma f_{-,\sigma}e^{-ik_Fx}, \quad f = u, v. \quad (7)$$

New operators γ, γ^+ satisfy the fermionic commutative relations $\{\gamma_{n,\sigma}, \gamma_{m,\sigma'}^+\} = \delta_{m,n}\delta_{\sigma,\sigma'}$. The transformations (5) must diagonalize the Hamiltonian H:

$$H = E_g + \sum_{\epsilon_n>0}\epsilon_n\gamma_{n,\sigma}^+\gamma_{n,\sigma}, \quad (8)$$

$$E_g = \sum_{\epsilon_n<0}\epsilon_n + \int dx\left(\frac{|\Delta|^2}{\pi\lambda}+\frac{|\Delta|_s^2}{\pi\lambda_s}-\frac{\alpha}{2}\rho^2\right),$$

where E_g is the ground state energy and $\epsilon_n > 0$ is the energy of excitation n.

Following [14], we obtain the eigenvalue equations

$$\hat{H}\chi = \epsilon\chi, \quad (9)$$

where

$$\hat{H} = \begin{pmatrix} -i\frac{\partial}{\partial x}+\alpha\rho & \Delta & \Delta_s & 0 \\ \Delta^* & i\frac{\partial}{\partial x}+\alpha\rho & 0 & \Delta_s \\ \Delta_s^* & 0 & i\frac{\partial}{\partial x}-\alpha\rho & \Delta \\ 0 & \Delta_s^* & \Delta^* & -i\frac{\partial}{\partial x}-\alpha\rho \end{pmatrix},$$

$\chi^T = (u_+, u_-, v_+, v_-)$, and self-consistent conditions

$$\rho(x) = 2\sum[(u_+^*u_+ + u_-^*u_-)f + (v_+^*v_+ + v_-^*v_-)(1-f)], \quad (10)$$

$$\Delta(x) = -4\lambda[\sum u_-^*u_+f - \sum v_-^*v_+(1-f)], \quad (11)$$

$$\Delta_s = 2\lambda_s\sum(1-2f)[v_+^*u_+ + v_-^*u_-], \quad (12)$$

where $f = 1/(\exp[\epsilon/T] + 1)$. We omitted spin indices since, in our representation for wave functions, all equations are diagonal over spin.

At first, consider homogeneous state with constant $\Delta = |\Delta|\exp[i\varphi]$, $\Delta_s = |\Delta_s|\exp[i\varphi_s]$, and $\rho(x) = \bar{\rho} \equiv N/L$. The average spin density has the form $\langle S_z\rangle \propto$

$\mathrm{Re}(\Delta\exp(2ik_Fx))$. Neglecting trivial dependence on $\bar{\rho}$, we obtain two branch spectrum $\epsilon_\pm^2 = k^2 + (|\Delta| \pm |\Delta_s|^2)^2$, with wave functions $u, v \propto \exp[ikx]$ satisfying the symmetry relations

$$\begin{aligned} v_+ &= \pm u_- \exp i[\varphi - \varphi_s], \\ v_- &= \pm u_+ \exp -i[\varphi + \varphi_s]. \end{aligned} \tag{13}$$

The self-consistent equations read

$$|\Delta| = \frac{\lambda}{L}[F_+ + F_-], \quad |\Delta_s| = \frac{\lambda_s}{L}[F_+ - F_-], \tag{14}$$

where $F_\pm = \sum_\epsilon [(|\Delta| \pm |\Delta_s|)/\epsilon_\pm]\tanh[\epsilon_\pm/T]$. At zero temperature, we obtain

$$\frac{2}{\lambda} = \log\frac{4\epsilon_F^2}{\left||\Delta|^2 - |\Delta_s|^2\right|} + \frac{|\Delta_s|}{|\Delta|}\log\left|\frac{|\Delta| - |\Delta_s|}{|\Delta| + |\Delta_s|}\right|. \tag{15}$$

The second equation is derived from the first one by substituting $\lambda \longrightarrow \lambda_s$, $\Delta \longleftrightarrow \Delta_s$. The minimum of the ground state energy E_g is achieved at the state $\Delta = 2\epsilon_F\exp[-1/\lambda]$, $\Delta_s = 0$ for the case $\lambda > \lambda_s$, and $\Delta_s = 2\epsilon_F\exp[-1/\lambda_s]$, $\Delta = 0$ for the case $\lambda < \lambda_s$.

In general, parameters λ, λ_s depend on the doping concentration $h = |\rho - 1|$. It is well known that the coupling constant λ monotonically decreases with doping from λ_0 at $\rho = 1$ to the value $\lambda_0/2$ in the limit $|\rho - 1| \gg \Delta/v_F$ (due to the absence of Umklapp scattering at $\rho \neq 1$) [15]. If we suppose that the superconducting part H_s comes from neighboring site repulsion (as considered for 2D CuO plane model) $H_s \sim V\rho_n\rho_{n\pm1}$, then the self-consistent equation becomes $\Delta_s \sim V\langle\Psi_{n,\downarrow}\Psi_{n\pm1,\uparrow}\rangle \longrightarrow 2V\cos k_F a\langle\Psi_\downarrow(x)\Psi_\uparrow(x)\rangle$ in the continual approximation. The coupling constant $\lambda_s \sim (2/\pi)V\cos(\pi\rho/2)$ increases with hole doping $h = 1 - \rho$. If the ground state of an undoped system is antiferromagnet state ($\lambda > \lambda_s$), phase transition to the superconducting state will take place at some doping h_c where $\lambda = \lambda_s$. Two phases (SDW and SC) with $\Delta = \Delta_s \neq 0$ can coexist at this point. For detailed investigation of the phase transition, more rigorous consideration of quantum fluctuations is necessary.

So far, we have considered the uniform state with Δ, Δ_s = const. Since symmetry relations between wave function components (13) are independent of absolute values ($|\Delta|$, $|\Delta_s|$), we assume that these relations are valid also in a general case of nonuniform order parameters. Substituting (13) to (9), we obtain, in the case of constant phases φ, φ_s, equations

$$\left[-i\sigma_z\frac{d}{dx} + \tilde{\Delta}\sigma_+ + \tilde{\Delta}^*\sigma_-\right]\mathbf{u} = \epsilon\mathbf{u}, \tag{16}$$

where $\mathbf{u}^T = \{u_+, u_-\}$, $\tilde{\Delta} = (\Delta \pm \Delta_s)\exp[i\varphi]$. These equations are eigenvalue equations for the Peierls model and were studied in [15, 16]. The dependence on ρ in (1) was excluded by means of wave function transformation $u_\pm$, $v_\pm \longrightarrow \exp\{\mp i\alpha\int\rho dx\}u_\pm$, $v_\pm$. The term $\alpha\int dx\rho^2/2$ in the total energy E_g is responsible for commensurate effects and pinning of the system at rational doping ($h = m/n$) points [12].

Consider the system with $\lambda > \lambda_s$. At $\bar{\rho} = 1$, the ground state is an antiferromagnet with constant $\Delta = \Delta_0$, $\rho = \bar{\rho}$, and $\Delta_s = 0$. As a result of doping, kink states are formed with local level $\epsilon = 0$ at the center of the gap 2Δ. The single kink solution of (1) is $\tilde{\Delta}_1 = \Delta + \Delta_s = \Delta_0\tanh(\Delta_0 x + a/2)$, $\tilde{\Delta}_2 = \Delta - \Delta_s = \Delta_0\tanh(\Delta_0 x - a/2)$ with arbitrary shift a. The wave functions and the excitation spectrum read

$$\begin{aligned} u_\pm &\propto (\pm\epsilon + k + i\Delta_0\tanh\xi)e^{ikx}e^{\pm i\pi/4}, \\ \epsilon^2 &= k^2 + \Delta_0^2, \end{aligned} \tag{17}$$

$$u_{0,\pm} \propto \frac{\exp[\pm i\pi/4]}{\cosh^2\xi}, \quad \epsilon = 0, \tag{18}$$

where $\xi = \Delta_0 x \pm a/2$. The order parameters Δ, Δ_s take form

$$\Delta_s = \frac{\Delta_0\sinh a}{2(\cosh^2\Delta_0 x + \sinh^2 a/2)},$$

$$\Delta = \frac{\Delta_0\tanh\Delta_0 x}{1 + \dfrac{\sinh^2 a/2}{\cosh^2\Delta_0 x}}.$$

For the case $a = 0$, we obtain $\Delta_s \equiv 0$, $\Delta = \Delta_0\tanh\Delta_0 x$, $\rho \propto 1/\cosh^2\Delta_0 x$. It is the one stripe solution found in [12]. The shift $0 < a \ll 1$ leads to the appearance in the region around the stripe of $\Delta_s \neq 0$, so that $\rho \propto 1/\cosh^2\Delta_0 x$, $\Delta_s \propto a/\cosh^2\Delta_0 x$. The quasiparticle spectrum is independent of a; therefore, the equilibrium position a is defined by minimization of the potential energy

$$\delta W(a) = \frac{\Delta_0}{\pi}\left|\frac{1}{\lambda_s} - \frac{1}{\lambda}\right|\frac{a}{\tanh a} + \frac{\Delta_0\alpha}{4}\frac{\dfrac{\alpha}{\tanh a} - 1}{\sinh^2 a}. \tag{19}$$

The minimum of energy (19) is reached at $a = 0$ for $\gamma \equiv \alpha\pi\lambda\lambda_s/4|\lambda - \lambda_s| - 2.5 < 0$. For small a, the inequality $\gamma < 0$ is possible if λ and λ_s are not very close to one another ($|\lambda - \lambda_s| \gtrsim \alpha\lambda\lambda_s$). The nontrivial minimum $a \neq 0$ exists only in the small region $|\lambda - \lambda_s| \lesssim \alpha\lambda\lambda_s$ around the transition point $\lambda = \lambda_s$, where $\gamma > 0$. Stripe and superconductivity phases coexist in this region: Δ_s, Δ, $\rho(x) \neq 0$. The equilibrium shift a is small—$a \propto \sqrt{\gamma}$ if $\gamma \ll 1$—but it logarithmically diverges $a \propto \log\gamma$ in the limit $\lambda_s \longrightarrow \lambda$.

So, we find that increased doping for the system with $\lambda > \lambda_s$, $\gamma < 0$ at $\rho = 1$ leads to the formation of a periodic structure of charged kinks $\Delta = \Delta_0 \tanh \Delta_0 x$, which acquires the form $h = |\rho - 1| \gg v_F/\Delta_0$ [12]

$$\Delta \sim \Delta_0 \sqrt{k}\,\mathrm{sn}[\Delta_0 x/\sqrt{k}, k], \quad \rho(x) - \bar{\rho} \propto \Delta^2 - \bar{\Delta}^2,$$

where $K(k)$ is the elliptic integral of the first kind, sn(., k) is the Jacobi elliptic function, $|\bar{\rho} - 1| = \Delta_0/2K(k)\sqrt{k}$.

The superconducting order parameter $\Delta_s \neq 0$ appears in the case considered at some higher doping level where γ becomes positive. In a small region, $|\lambda - \lambda_s| \lesssim \alpha\lambda\lambda_s$ around the transition point $\lambda = \lambda_s$, where $\gamma > 0$, superconductivity and spin/charge orders coexist: Δ_s, Δ, $\rho(x) \neq 0$. In the particular case of a model with $\alpha = 0$, this region is reduced to the point $h = h_c$. A more complicated analysis beyond the scope of the used mean field approximation is required at this point to take into account strong quantum fluctuations, including the zero mode due to the degeneration of the ground state with respect to the shift a of two sublattices.

The opposite region $\lambda < \lambda_s$ can be studied using the duality properties of the model. It is easy to see that eigenvalues ϵ_n of equations (9) are invariant under transformation $\Delta \longleftrightarrow \Delta_s$. Indeed, if we simultaneously exchange $\Delta \longleftrightarrow \Delta_s$ and $u_-(x) \longleftrightarrow v_+(x)$ in Eq. (9), the Hamiltonian (9) is not changed (without unimportant terms with $\rho(x)$). Therefore, the ground state energy E_g in (8) is invariant under the transformations $\Delta \longleftrightarrow \Delta_s$, $\lambda \longleftrightarrow \lambda_s$. Thus, we can apply solutions obtained above for the superconductivity phase. We find that, in the region $\gamma > 0$, the ground state is a superconductor with $\Delta_s = \text{const}$, $\Delta = 0$. The one-dimensional analogue of the vortex in a two- or three-dimensional systems is the kink: $\Delta_s = \Delta_0 \tanh \Delta_0 x$.

Due to the duality symmetry, the charge density $\rho(x)$ has the same expression as the kink in the spin density wave. Therefore, we obtain that the charge density is not zero in the vicinity of the kink

$$\rho(x) \sim \frac{1}{\cosh^2 \Delta_0 x} \cos(2\pi|\rho - 1|). \qquad (20)$$

Similar to the previous case ($\lambda > \lambda_s$), we find that, near the transition point ($\lambda \sim \lambda_s$, $\gamma > 0$), a stripe structure can arise. In the limit $0 < \gamma \ll 1$, $|\bar{\rho} - 1| \gg \Delta_0/v_F$, we obtain

$$\Delta(x) \propto \sin \pi|\bar{\rho} - 1|x, \quad \tilde{\rho}(x) \propto \cos 2\pi|\bar{\rho} - 1|x,$$
$$a \propto \sqrt{\gamma}.$$

To conclude, we have found the self-consistent mean-field analytical solution for the ground state structure of the quasi-one-dimensional electronic system with spin, charge, and superconducting correlations. We have found that, for an appropriate choice of parameters, the ground state is a striped charge/spin density wave structure with low hole doping. The stripe configuration is pinned at rational points $|\rho - 1| = m/n$ with the pinning energy $\propto \exp(-Cn)$ substantial for small n, which can lead to the stability of the stripe picture. The phase transition to the superconductivity state takes place at some doping level. Both superconductivity and spin/charge density wave order parameters can coexist in a small region near this point.

The model is self-dual: The eigenfunction equations are invariant with respect to transformations $\lambda \longleftrightarrow \lambda_s$, $\Delta \longleftrightarrow \Delta_s$. Therefore, properties of a superconducting state can be derived from the low doping consideration. In particular, we found that charge stripes can exist in low doping spin density wave state as in superconducting states, in the vicinity of spatially nonuniform configurations of Δ_s such as vertices (kinks in one dimension).

Though this one-dimensional model can be applied to quasi-one-dimensional systems rather than to high-temperature quasi-two-dimensional anisotropic superconductors, it shows some properties peculiar to high-temperature superconductors (one-dimensional stripe structure at low doping and superconductivity at a higher doping, etc.). Therefore, our results can be useful for understanding high-temperature phenomenon. For describing anisotropic properties of real systems, consideration of a two-dimensional model is required to take into account the important contributions from nodal quasiparticles.

I thank A.V. Balatsky, I. Martin, S.I. Mukhin, and J. Zaanen for stimulated discussions and K. Machida for pointing relevant references out.

The work was supported by the Russian Foundation for Basic Research, project no. 02-02-16354.

REFERENCES

1. S.-W. Cheong, G. Aeppli, T. E. Mason, *et al.*, Phys. Rev. Lett. **67**, 1791 (1991); C. H. Chen, S.-W. Cheong, and A. S. Cooper, Phys. Rev. Lett. **71**, 2461 (1993); J. Tranquada, B. J. Sternlieb, J. D. Axe, *et al.*, Nature **375**, 561 (1995).
2. J. Zaanen and O. Gunnarson, Phys. Rev. B **40**, 7391 (1989); V. J. Emery, S. A. Kivelson, and H.-Q. Lin, Phys. Rev. Lett. **64**, 475 (1990); C. Castellani, C. Di Castro, and M. Grilli, Phys. Rev. Lett. **75**, 4650 (1995).
3. K. Machida, Physica C (Amsterdam) **158**, 192 (1989); M. Kato, K. Machida, H. Nakanishi, and M. Fujita, J. Phys. Soc. Jpn. **59**, 1047 (1990).
4. H. J. Schulz, J. Phys. (Paris) **50**, 2833 (1989); Phys. Rev. Lett. **64**, 1445 (1990).
5. I. Martin, G. Ortiz, A. V. Balatsky, and A. R. Bishop, Int. J. Mod. Phys. B **14**, 3567 (2000).

6. J. M. Tranquada, J. D. Axe, N. Ichikawa, *et al.*, Phys. Rev. Lett. **78**, 338 (1997).
7. B. Lake, G. Appli, K. N. Clausen, *et al.*, Science **291**, 1759 (2001).
8. B. Lake, H. M. Rönnow, N. B. Christensen, *et al.*, Nature **415**, 299 (2002).
9. V. F. Mitrovic, E. E. Sigmund, M. Eschrig, *et al.*, Nature **413**, 501 (2001).
10. J. E. Hoffman, E. W. Hudson, K. M. Lang, *et al.*, Science **295**, 466 (2002).
11. Y. S. Lee, R. J. Birgeneau, M. A. Kastner, *et al.*, Phys. Rev. B **60**, 3643 (1999); H. Kimura, H. Matsushita, K. Hirota, *et al.*, Phys. Rev. B **61**, 14366 (2000).
12. S. I. Matveenko and S. I. Mukhin, Phys. Rev. Lett. **84**, 6066 (2000).
13. S. I. Mukhin, Phys. Rev. B **62**, 4332 (2000).
14. P.-G. de Gennes, *Superconductivity of Metals and Alloys* (Benjamin, New York, 1966; Mir, Moscow, 1968).
15. S. A. Brazovskii, Zh. Éksp. Teor. Fiz. **78**, 677 (1980) [Sov. Phys. JETP **51**, 342 (1980)]; S. A. Brazovskii, S. A. Gordyunin, and N. N. Kirova, Pis'ma Zh. Éksp. Teor. Fiz. **31**, 486 (1980) [JETP Lett. **31**, 456 (1980)].
16. S. A. Brazovskii and S. I. Matveenko, Zh. Éksp. Teor. Fiz. **87**, 1400 (1984) [Sov. Phys. JETP **60**, 804 (1984)].

JETP Letters, Vol. 78, No. 6, 2003, pp. 389–392. Translated from Pis'ma v Zhurnal Éksperimental'noĭ i Teoreticheskoĭ Fiziki, Vol. 78, No. 6, 2003, pp. 841–844.
Original Russian Text Copyright © 2003 by Bush, Gippius, Zalesskiĭ, Morozova.

^{209}Bi NMR Spectrum of $BiFeO_3$ in the Presence of Spatial Modulation of Hyperfine Fields

A. A. Bush[1], A. A. Gippius[2], A. V. Zalesskiĭ[3,] *, and E. N. Morozova[2]

[1] *Moscow State Institute of Radioengineering, Electronics, and Automation (Technical University), pr. Vernadskogo 78, Moscow, 117454 Russia*

[2] *Moscow State University, Vorob'evy gory, Moscow, 119899 Russia*

[3] *Shubnikov Institute of Crystallography, Russian Academy of Sciences, Leninskiĭ pr. 59, Moscow, 119333 Russia*

**e-mail: nmr@ns.crys.ras.ru*

Received August 18, 2003

A complicated spin-echo spectrum was observed for ^{209}Bi nuclei in a ferroelectric antiferromagnet $BiFeO_3$ in zero external field. This spectrum is the first example of nuclear quadrupole resonance of a system of diamagnetic atoms in a hyperfine magnetic field produced by the spatially modulated Fe^{3+} spin system and varying in orientation and magnitude. An attempt is undertaken to theoretically simulate the spectrum. © *2003 MAIK "Nauka/Interperiodica".*

PACS numbers: 76.60.Lz; 75.25.+z

Interest in bismuth ferrite $BiFeO_3$ is caused by several facts. First, in its properties, it is related to so-called ferroelectric magnets, i.e., to the materials simultaneously possessing long-range magnetic spin and electric-dipole orders [1]. The interaction between the electrical and magnetic subsystems renders $BiFeO_3$ an interesting object for studying the magnetoelectric effect [2–4]. Second, it possesses a unique magnetic structure with spatial spin modulation of the cycloid type, which is quite uncommon for weakly distorted cubic compounds with perovskite structure. The spin-modulated structure was observed by neutron diffraction in [5] and confirmed recently by the ^{57}Fe NMR studies [6–8]. The appearance of ferroelectricity and magnetic cycloid is in agreement with the symmetry of the $BiFeO_3$ unit cell, which, being "stretched" along one of the threefold axes of an ideal perovskite cube, transforms it into rhombohedron. The Fe^{3+} and Bi^{3+} cations are positioned in the cell in such a way that the center of symmetry disappears, so that spontaneous polarization can occur (Curie temperature $T_C \approx 1118$ K [9]). The magnetic antiferromagnetic order appears in the system of Fe^{3+} ions at a lower temperature (Néel temperature $T_N \approx 653$ K). At $T < T_N$, the unit-cell symmetry of $BiFeO_3$ is described by the space group $R3c$ and by the corresponding point-group symmetry $3m$ that contains a threefold symmetry axis (c axis) and three longitudinal symmetry planes. The room-temperature parameters of the bimolecular rhomohedral unit cell of $BiFeO_3$ are as follows: $a = 3.96$ Å and $\alpha = 89°28'$ in the hexagonal system with $a_{hex} = 5.5876$ Å and $c_{hex} = 13.876$ Å [10]. A free-energy analysis of the magnetic properties of $BiFeO_3$ with allowance for the symmetry of $BiFeO_3$ crystal suggests that the spatial cycloid-type spin-modulated wave propagating with equal probability in the longitudinal planes m with the wave vector perpendicular to the c axis can appear at $T < T_N$ [11, 12]. In such a magnetic structure, the spin system retains the G-type antiferromagnetic order in the nearest surroundings but changes along the cycloid propagation direction in such a way that the antiferromagnetic vector **L** turns in the longitudinal symmetry plane with a period $\lambda = 620 \pm 20$ Å (according to [5]) that is incommensurate with the lattice constant.

A change in the angle θ between **L** and the c axis directed along the cycloid preparation (x axis) has the form [11, 13]

$$\mu = \cos\theta(x) = \mathrm{sn}\left(\pm\frac{4K(k)}{\lambda}x, k\right), \qquad (1)$$

where $\mathrm{sn}(x, k)$ is the Jacobi elliptic function, k is its parameter, and $K(k)$ is the complete elliptic integral of the first kind. The spatial rotation of the local hf field at the ^{57}Fe nuclei obeys the same law. The rotation of spin system results in the hf-field anisotropy, which comprises about 1% of the total hf field at the ^{57}Fe nuclei (545 kOe at 4.2 K). The presence of this anisotropy and the specific features of the hf-field density distribution along the cycloid coordinate x (1) give rise to the ^{57}Fe NMR spectrum in a certain frequency interval with two asymmetric edge absorption peaks and a characteristic dip between them. The properties of this spectrum were studied in [6–8].

Apart from the system of magnetic Fe^{3+} ions, the $BiFeO_3$ structure contains nonmagnetic Bi^{3+} atoms. An

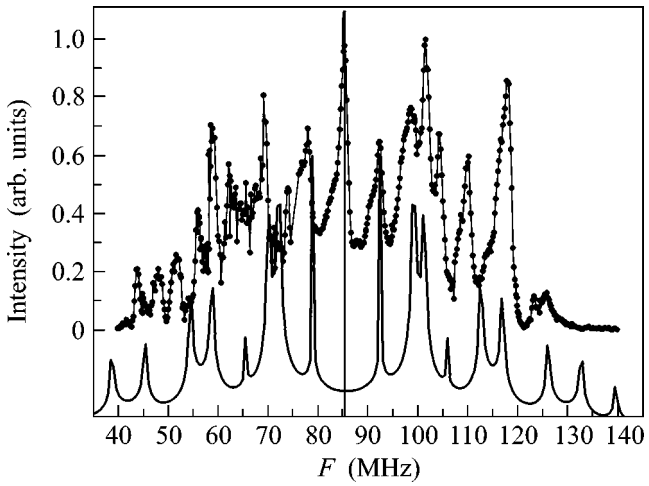

Fig. 1. The experimental ^{209}Bi spin echo spectrum in $BiFeO_3$ at 4.2 K (points) and its theoretical simulation (shifted to the bottom of the figure).

effort thus can be made to use the nuclei of the ^{209}Bi isotope, having 100% abundance and spin $I = 9/2$, as an additional microscopic probe for gaining new information about the spin-modulated structure in $BiFeO_3$. The data on such studies are lacking in the literature. In this paper, the first results on ^{209}Bi NMR in $BiFeO_3$ are presented and analyzed. The preliminary results were reported at the conference "Physics of Magnetism" on July 1–5, 2002 (Poznan, Poland [14]).

Spin echo in zero external magnetic field was observed using two radiospectrometers; one of them was of the coherent type with accumulation and point-by-point frequency scanning, and another was an ISSh-1-13M spectrometer of the superheterodyne type (designed at the Special Design Office of the Institute of Radio Engineering and Electronics, Russian Academy of Sciences) with a continuous record of the echo amplitude as a function of frequency. Three samples of crushed $BiFeO_3$ ceramics prepared by the same standard technique, though at different times, were studied. They differed only in the degree of ^{57}Fe-isotope enrichment: 95.43, 10.0, and 2.2 (natural abundance) wt % and were designed for studying the iron NMR spectra. All earlier iron NMR studies [6–8] were repeated on the sample with 95.43% of ^{57}Fe. More detailed data on the sample preparation and certification are presented in the cited works.

The ^{209}Bi spin echo spectrum of $BiFeO_3$ at 4.2 K is shown in Fig. 1. It spans a broad frequency range (40–130 MHz) and consists of many asymmetric lines. With a rise in temperature, the echo-signal intensity decreases rapidly, because the spectrum-averaged spin–spin relaxation time T_2 shortens from 36–50 μs at 4.2 K to 3–10 μs at 10 K. At higher temperatures, the spectrum becomes unobservable. Note that such a complicated structure of the spectrum was repeated exactly for all three $BiFeO_3$ samples prepared at different times and was confirmed by the independent measurements on both spectrometers.

If the ^{209}Bi nuclei are subjected to a uniformly directed local magnetic field H_{loc}, whose Zeeman energy far exceeds the quadrupole energy, the NMR (AFMR) spectrum of the ^{209}Bi nuclei with spin $I = 9/2$ must consist of nine lines: the most intense central line at the so-called Larmor frequency ν_L corresponding to the H_{loc} at the ^{209}Bi nuclei and eight side lines (four pairs situated to the right and left of the central line) with decreasing intensities. However, the observed spectrum obviously differs from this simplest situation. It is structurally much more complicated, which can naturally be explained by the spatial variation of the direction and magnitude of H_{loc} in $BiFeO_3$.

The local field H_{loc} at the ^{209}Bi nuclei was estimated from the frequency of maximal intensity in the middle portion of the spectrum near 85 MHz to give a value of 124 kOe (the gyromagnetic ratio of the ^{209}Bi nucleus is $\gamma/2\pi = 0.6842$ MHz/kOe).

To analyze the reasons for the appearance of a strong local field H_{loc} at the ^{209}Bi nuclei, we consider the structural data. In a rhombohedrally distorted perovskite, to which $BiFeO_3$ belongs, the ^{209}Bi nuclei can be subjected both to the inhomogeneous electric fields of the surrounding atoms (quadrupole interaction) and to the hf magnetic and dipole fields. The Fe environment of the Bi atom in $BiFeO_3$ is schematically shown in Fig. 2, according to the data from [15] (oxygen atoms are not shown). The Fe and Bi atoms form a chain along the *c* axis with alternating separation $k = 3.0617$ Å and $l = 3.872$ Å. The remaining six Bi–Fe distances are 3.3071 Å (three *m* bonds) and 3.5793 Å (three *n* bonds). The Fe atoms form layers perpendicular to the *c* axis, with the parallel spin orientation within each layer (at a given cycloid point) and the antiparallel orientation between the neighboring layers. Note that the magnetic contributions in an undistorted cubic perovskite are mutually compensated because of the perfect cubic Fe environment of the Bi atoms ($k = l = m = n$). For the same reason, the electric field gradient (EFG) should be zero. It follows from Fig. 2 that the low-symmetric arrangement of the neighboring magnetic Fe atoms in the $BiFeO_3$ structure provides not only a nonzero EFG at the ^{209}Bi nuclei, but also a nonzero contribution to the local field from both the dipolar interaction (H_d) and the direct hf-field transfer H_{tr}: $\mathbf{H}_{loc} = \mathbf{H}_d + \mathbf{H}_{tr}$. Since the dipole field in magnetic oxides usually does not exceed a few kOe, the experimentally observed high value $H_{loc} = 124$ kOe should be assigned mainly to the hf field H_{tr} appearing as a result of the uncompensated hf-field transfer due to the overlap between the orbitals of the neighboring Bi^{3+} and Fe^{3+} atoms along the *k*, *l*, *m*, and *n* bonds.

We will calculate the spectrum with allowance for the fact that the polar angle θ between the magnetic field H_{loc} and the EFG principal axis (c axis) in our case is not a constant value but changes following Eq. (1); i.e., it is a function of the coordinate x along the cycloid propagation direction. To simplify the calculation, we assume that the azimuthal angle between H_{loc} and the EFG axis and the EFG asymmetry parameter are zero. We also ignore the possible dependence of H_{loc} on the angle θ (H_{loc} anisotropy).

Under these conditions, the resonance $m \longleftrightarrow m-1$ transition frequency is equal, in the approximation of a high magnetic field and quadrupole perturbation, to

$$\nu = \nu_L + \frac{\nu_Q}{2}\left(m-\frac{1}{2}\right)(3\mu^2-1), \tag{2}$$

where ν_Q is the quadrupole frequency and m is the magnetic quantum number. From Eq. (2) it follows that

$$\mu = \pm\sqrt{(\nu-\nu_L+c)/b},$$
$$b = \frac{3}{2}\nu_Q\left(m-\frac{1}{2}\right), \quad c = \frac{1}{2}\nu_Q\left(m-\frac{1}{2}\right), \tag{3}$$
$$\nu_Q = \frac{3e^2q_{zz}Q}{2I(2I-1)h},$$

where eQ is the nuclear quadrupole moment (e is the electron charge), eq_{zz} is the EFG component along the axis $z \parallel c$, and h is the Planck's constant.

The line shape in the δ-function approximation is sought in the form

$$p(\nu) \propto \frac{dx}{d\mu}\frac{d\mu}{d\nu}. \tag{4}$$

From Eqs. (1) and (3) one obtains

$$\frac{dx}{d\mu} = \frac{\pm\lambda}{4K(k)}\frac{1}{\sqrt{(1-\mu^2)(1-k^2\mu^2)}}, \tag{5}$$

$$\frac{d\mu}{d\nu} = \frac{\pm1}{2\sqrt{(\nu-\nu_L+c)b}}. \tag{6}$$

Substitution of Eqs. (5) and (6) into Eq. (4) gives

$$P(\nu) \propto \frac{\pm\lambda\sqrt{b}}{4K(k)(\nu-\nu_L+c)^{1/2}} \times \frac{\pm1}{\{[(b-c)-(\nu-\nu_L)][(b-k^2c)-k^2(\nu-\nu_L)]\}^{1/2}}. \tag{7}$$

Function (7) has singularities at the following frequencies:

$$\nu_1 = \nu_L - \frac{1}{2}\nu_Q\left(m-\frac{1}{2}\right), \quad \nu_2 = \nu_L + \nu_Q\left(m-\frac{1}{2}\right),$$

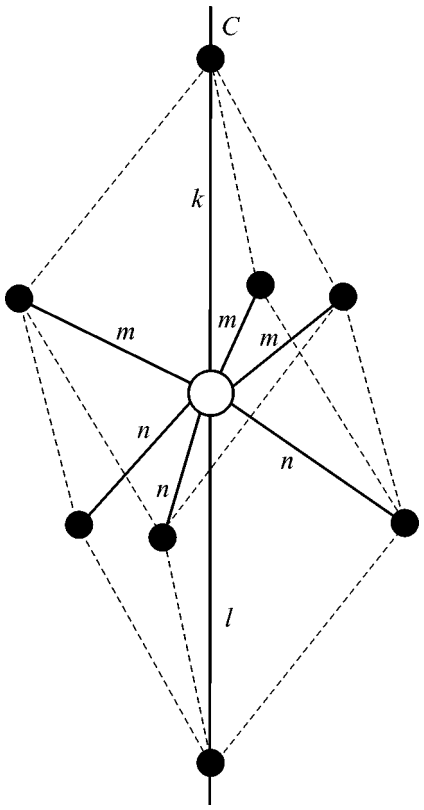

Fig. 2. The Bi atom (central circle) surrounded by the Fe atoms (black circles) in the $BiFeO_3$ structure.

$$\nu_3 = \nu_L + \frac{1}{2}\nu_Q\left(m-\frac{1}{2}\right)\left(\frac{3}{k^2}-1\right).$$

The theoretical spectrum shown by the solid line at the bottom of Fig. 1 is the superposition of spectra (7) corresponding to all $m \longleftrightarrow m-1$ transitions of spin $I = 9/2$. The spectrum was calculated in the reduced coordinates and superposed on the experimental spectrum so as to obtain approximate agreement with the experiment for the side peaks on both sides of the central peak at frequency $\nu_L \approx 85$ MHz corresponding to $H_{loc} = 124$ kOe. The best agreement between the experimental and theoretical spectra is achieved for the cycloid anharmonicity parameter $k = 0.95$, which coincides with the value obtained earlier from the iron NMR spectra [6–8].

In conclusion, we should state that, despite the apparent similarity of the spectra, the assumptions adopted in our calculations proved to be insufficient for the experimental and theoretical spectra of the ^{209}Bi nuclei in $BiFeO_3$ to be adequate. In particular, this refers to the neglect of the $H_{loc}(\theta)$ anisotropy, which plays an important part in the formation of the iron NMR spectrum. Recent ^{57}Fe NMR studies in $BiFeO_3$ have shown [8] that the spatial modulation of iron magnetic moments is accompanied by the modulation of the

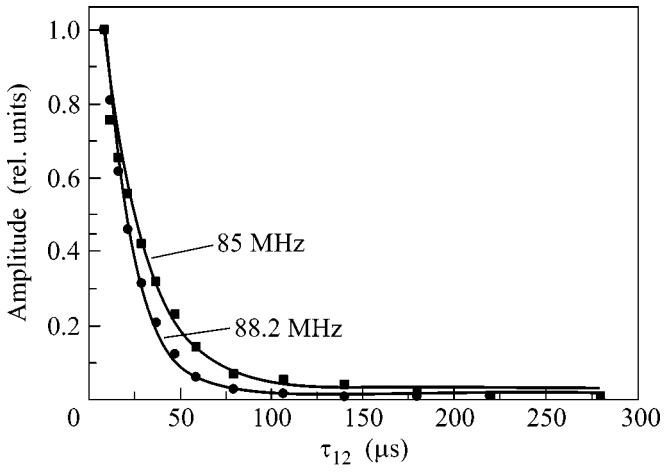

Fig. 3. Curves for echo decay with increasing the time interval τ_{12} between the pulses, as measured at frequencies of 85 and 88.2 MHz. The initial amplitudes are normalized to the same value.

spin–spin interaction and the local line width, indicating that these factors must be taken into account in the spectrum analysis. In this connection, we note that measurements of the ^{209}Bi spin–spin relaxation times in different spectral intervals at 4.2 K showed that the T_2 values differ substantially for peaks and dips (for example, $T_2 \approx 50$ μs at the maximum at 85 MHz and $T_2 \approx 36$ μs at the minimum at a frequency of 88.2 MHz; see Fig. 3). In addition, the dynamic interactions between nuclei should reveal themself at the temperature of liquid helium in systems with a 100% abundance of magnetic isotope, which also can affect the structure of the spectrum. These problems should be clarified in further studies.

This work was supported by the Russian Foundation for Basic Research, project no. 02-02-16369.

REFERENCES

1. Yu. N. Venevtsev, V. V. Gagulin, and V. N. Lyubimov, *Seignette-Magnetics* (Nauka, Moscow, 1982).
2. Yu. F. Popov, A. K. Zvezdin, G. P. Vorob'ev, *et al.*, Pis'ma Zh. Éksp. Teor. Fiz. **57**, 65 (1993) [JETP Lett. **57**, 69 (1993)].
3. Yu. F. Popov, A. M. Kadomtseva, G. P. Vorob'ev, and A. K. Zvezdin, Ferroelectrics **162**, 135 (1994).
4. A. M. Kadomtseva, Yu. F. Popov, G. P. Vorob'ev, and A. K. Zvezdin, Physica B (Amsterdam) **211**, 327 (1995).
5. I. Sosnowska, T. Peterlin-Neumaier, and E. Steichele, J. Phys. C: Solid State Phys. **15**, 4835 (1982).
6. A. V. Zalessky, A. A. Frolov, T. A. Khimich, *et al.*, Europhys. Lett. **50**, 547 (2000).
7. A. V. Zalesskiĭ, A. K. Zvezdin, A. A. Frolov, and A. A. Bush, Pis'ma Zh. Éksp. Teor. Fiz. **71**, 682 (2000) [JETP Lett. **71**, 465 (2000)].
8. A. V. Zalesskiĭ, A. A. Frolov, A. K. Zvezdin, *et al.*, Zh. Éksp. Teor. Fiz. **122**, 116 (2002) [JETP **95**, 101 (2002)].
9. J. D. Bucci, B. K. Roberston, and W. J. James, J. Appl. Cryst. **5**, 187 (1972).
10. J. M. Moreau, C. Michel, R. Gersdon, and W. J. James, J. Phys. Chem. Solids **32**, 1315 (1971).
11. I. Sosnowska and A. K. Zvezdin, J. Magn. Magn. Mater. **140–144**, 167 (1995).
12. Yu. F. Popov, A. K. Zvezdin, G. P. Vorob'ev, *et al.*, Pis'ma Zh. Éksp. Teor. Fiz. **57**, 65 (1993) [JETP Lett. **57**, 69 (1993)].
13. M.-M. Tehranchi, N. F. Kubrakov, and A. K. Zvezdin, Ferroelectrics **204**, 181 (1997).
14. A. A. Gippius, A. V. Zalessky, E. N. Morozova, *et al.*, Phys. Status Solidi A **196**, 221 (2003).
15. F. Kubel and H. Schmid, Acta Crystallogr. B **46**, 698 (1990).

Translated by V. Sakun

JETP Letters, Vol. 78, No. 6, 2003, pp. 393–397. From Pis'ma v Zhurnal Éksperimental'noĭ i Teoreticheskoĭ Fiziki, Vol. 78, No. 6, 2003, pp. 845–849.
Original English Text Copyright © 2003 by Brazhkin, Katayama, Inamura, Kondrin, Lyapin, Popova, Voloshin.

Structural Transformations in Liquid, Crystalline, and Glassy B_2O_3 under High Pressure¶

V. V. Brazhkin[1, *], Y. Katayama[2], Y. Inamura[2], M. V. Kondrin[1], A. G. Lyapin[1], S. V. Popova[1], and R. N. Voloshin[1]

[1] *Institute for High Pressure Physics, Russian Academy of Sciences, Troitsk, Moscow region, 142190 Russia*
[2] *Japan Atomic Energy Research Institute SPRING 8, 1-1-1 Kouto Mikazuki, Sayo, Hyogo, 679-5143, Japan*
**e-mail: brazhkin@hppi.troitsk.ru*
Received August 19, 2003

We present *in situ* (x-ray diffraction) and *ex situ* (quenching) structural studies of crystalline, liquid, and glassy B_2O_3 up to 9 GPa and 1700 K, drawing equilibrium and nonequilibrium phase diagrams of B_2O_3. Particularly, we have determined the melting curve, the stability regions for crystalline B_2O_3 I and B_2O_3 II modifications, the regions of transformations, such as densification or crystallization, for both the liquid and glassy states, including the region of sharp first-order-like transition in liquid B_2O_3 to a high-density phase near 7 GPa. Quenching experiments also show that the transition to the high-density liquid can occur at much lower pressures in nonstoichiometric melts with an excess of boron. B_2O_3 is the first glassformer whose transformations in the disordered state have been comparatively studied for both liquid and glassy phases. © *2003 MAIK "Nauka/Interperiodica".*

PACS numbers: 64.70.Kb; 62.50.+p; 61.43.-j; 61.50.Ks

1. In contrast to phase transitions in crystals, transformations in disordered condensed media, such as liquids and glasses, have not been adequately studied to date at broad variations of temperature and pressure [1]. There are very few examples of disordered substances with sharp structural changes and thermodynamic anomalies under pressure, e.g., the melts of P, Se, Bi, and Te, supercooled melts of Si and Ge, supercooled water and amorphous ices [1], which could be clearly associated with transformations similar or equivalent to the first-order transitions. For the amorphous ice H_2O [2] and liquid phosphorus [3], the macroscopic mixture of two amorphous or liquid phases, respectively, was observed at the transformation, which is direct evidence for the first-order phase transition. However, in the majority of simple liquids, such as melts of alkali metals, and in ordinary glasses, such as *a*-SiO_2 and *a*-GeO_2, broad transformations between two disordered states are observed under pressure [1, 4, 5]. Only for H_2O ice and water are the structural changes in liquid and disordered solid states clearly compared (e.g., see [1] and references therein). For glass-forming substances, there are still no examples of simultaneous comparative studies of phase transformations in the liquid and glassy states, due to high melting temperatures of readily glass-forming substances, like SiO_2 and GeO_2 and, on the other hand, due to low stability temperatures of elementary amorphous substances and glasses based on P, Se, Bi, and Te.

In the present work, boron oxide B_2O_3 is chosen for study of transformations in the disordered medium. This substance easily vitrifies and, at the same time, has low melting temperature $T_m \approx 750$ K at normal pressure. The glass and melt of B_2O_3 have network structures that in many respects makes them similar to archetypical glasses and melts, such as SiO_2 and H_2O [6]. Stable B_2O_3 I crystalline phase (sp. gr. $P3_1$, a = 4.336 Å, c = 8.340 Å, and density $\rho \approx 2.55$ g/cm^3) has a structure consisting of "ribbons" formed by B_2O_3 triangles [7]. The denser B_2O_3 II phase (sp. gr. $Ccm2_1$, a = 4.613 Å, b = 7.803 Å, c = 4.129 Å, and $\rho \approx 3.11$ g/cm^3 at normal conditions), with an orthorhombic structure based on distorted BO_4 tetrahedrons, can be synthesized at high pressures ($P > 4$ GPa) and temperatures ($T > 1000$ K) [8]. The threefold boron coordination 3 (by oxygen) and the twofold oxygen coordination 2 (by boron) in B_2O_3 I are changed to 4 and to an intermediate between 2 and 3, respectively, in B_2O_3 II [7, 8]. The pressure–temperature phase diagram of B_2O_3, including relative stability of these phases and the melting curve, has been rather scantly studied up until now [9–11]. Ordinary B_2O_3 glass is obtained from melt at very low cooling rates. This glass has the opened structure and low-density $\rho \approx 1.85$ g/cm^3 [6]. It is believed that the structure of this glass is based on low-coordinated boron atoms (Z = 3) and has a considerable fraction (~20%) of ring-shaped boroxol groups B_3O_6 [6, 11, 12]. The high-pressure treatment of B_2O_3 glass and quenching from melt under pressure allow one to obtain denser

¶ This article was submitted by the authors in English.

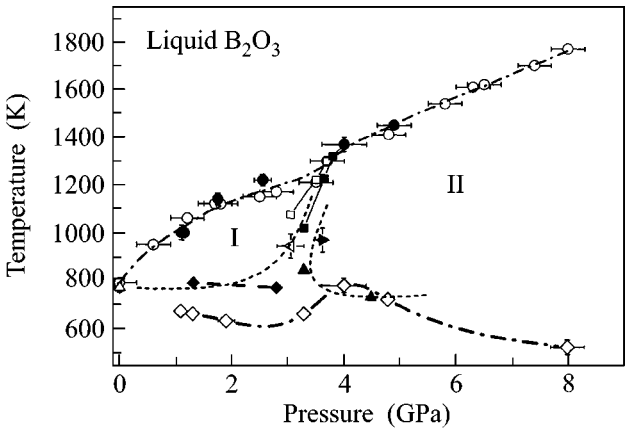

Fig. 1. The pressure–temperature phase diagram of B_2O_3, where symbols correspond to experimental points and lines are interpolations. The melting curve is shown by solid (*in situ* study) and open (DTA, TBA, and quenching experiments) circles and dash-and-dot line; the crystallization line (for times of the order of several minutes) of compressed ordinary glass, by open diamonds and thick dash-and-dot line; the crystallization line of quenched at high pressure glasses, by solid diamonds and thick dashed line; the I ⟶ II and II ⟶ I kinetic transition lines, by solid and open triangles, respectively, and thin dashed lines, where orientation of the triangle shows the direction of movement on the pressure–temperature plane. Open and solid squares correspond to points, where I and II crystalline phases, respectively, do not transit to each other, i.e., are experimentally stable nearby the triple point I–II-melt. When experimental bar is not shown, it is comparable or less than the size of the symbol.

glass with densities 10 to 20% higher than ordinary values [11, 13]. At normal pressure, the densified glass relaxes to its normal state at 300 to 600 K, depending on the history of its preparation [11, 13]. The study of the structure of densified B_2O_3 glass suggests that the densification was mainly associated with the breakup of boroxol groups and buckling of "ribbons" formed by B_2O_3 triangles [14, 15].

There are quite a few studies concerning the temperature dependence of the structure of B_2O_3 glass and liquid [16, 17]. The molecular dynamic simulation of B_2O_3 points to a possibility of structural coordination changes in the melt under pressure and acceleration of self-diffusion in a melt during compression [18]. Recently, we have found indirect experimental evidence for a decrease of viscosity and corresponding increase of diffusion in B_2O_3 melt under pressure [19]. The Raman and Brillouin study of B_2O_3 glass has been performed up to 14 GPa at room temperature [20, 21]. However, up to date, there were no in situ studies of the structures of liquid, glassy, or even crystalline B_2O_3 under pressure.

The purpose of the present work is the *in situ* high-pressure x-ray study of liquid, glassy, and crystalline B_2O_3, supported by quenching experiments, in order to study possible structural changes and phase transitions, to compare the behaviors of liquid and glassy states, to attain insight into the nature of B_2O_3 glass densification, and to examine the equilibrium and nonequilibrium phase diagrams of B_2O_3.

2. B_2O_3 ordinary glass, crystalline B_2O_3 I, and B_2O_3 II modifications (the last was specially obtained under pressure) were used as the starting phases for in situ experiments. Commercially available original B_2O_3 glasses contain, as a rule, several percent H_2O in the bound state (e.g., in H_3BO_3). Heat treatment of B_2O_3 glass at $T \approx 600$–700 K during 20 to 30 h or at $T \approx 800$ K during 5 to 10 h made it possible to obtain dehydrated specimens that were rapidly (<1 min) mounted into a high-pressure cell. The cylindrical specimens with diameter of 2 to 3 mm and height of 1 to 3 mm were placed into containers of BN, Pt, or Ta or directly into a graphite heater. Hermetic thick-wall Pt ampoules were used for the very high-temperature experiments (>1700 K) to avoid the partial decomposition of B_2O_3 compound and oxygen leakage. The "toroid" high-pressure chambers were used for the synthesis of crystalline phases and dense glasses, as well as for thermodynamic study by differential thermal and thermobaric analysis (DTA and TBA) up to 8 GPa and 2100 K. *In situ* structural experiments were carried out at the cubic multianvil press using the x-ray dispersive method (Spring-8, MAX-80 press, BL14B1 Beamline). The melt, crystalline phases, and glasses of B_2O_3 were studied to 5 GPa at high temperatures up to 1700 K and to 9 GPa at room temperature. *In situ* x-ray diffraction patterns were obtained at 11 pressure–temperature points for liquid B_2O_3, 44 points for glassy B_2O_3, and almost 100 points for the B_2O_3 I and B_2O_3 II crystalline phases. The structure of quenched glass at normal pressure was studied by x-ray diffraction (Bruker AXS). The density of the glasses was measured by the bottle method and by sinking the dense liquid mixtures. Hardness was measured using the PMT-3M microhardness tester. The index of refraction was studied by the immersion technique. The details of high-pressure experiments will be presented elsewhere.

3. The equilibrium phase diagram of B_2O_3 (Fig. 1) is one of the main results of this study. The positions of the melting curve and I–II transition line established here noticeably differ from those on the earlier versions of the phase diagram [9, 10]. We are the first who observed *in situ* the II ⟶ I transition in crystalline B_2O_3 during pressure release at high temperatures, which unambiguously confirms that B_2O_3 II is thermodynamically a high-pressure phase. Analysis of the *in situ* diffraction patterns for the crystalline phases allowed us to estimate their bulk moduli, $B \approx 55 \pm 15$ GPa for B_2O_3 I and $B \approx 90 \pm 15$ GPa for B_2O_3 II, and their expansion coefficients, $\alpha \approx (2 \pm 0.5) \times 10^{-5}$ K^{-1} for both the phases.

4. The *in situ* measured temperature of crystallization of the compressed ordinary B_2O_3 glass has a max-

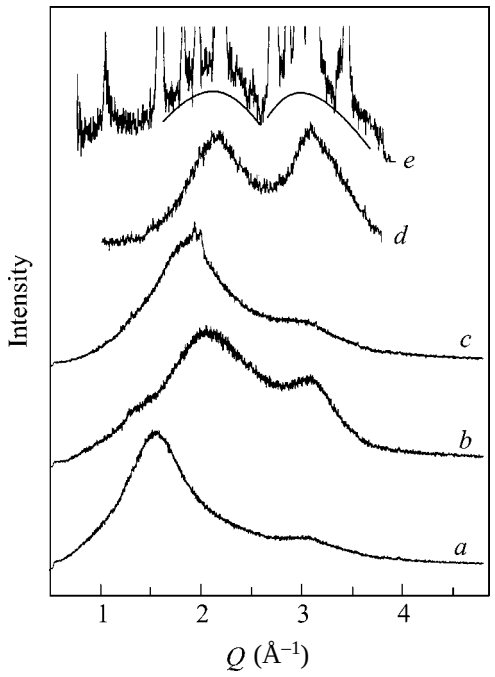

Fig. 2. X-ray diffraction patterns for ordinary B_2O_3 glass at $P = 10^{-4}$ GPa and $T = 300$ K (*a*), compressed ordinary glass at 8.42 ± 0.07 GPa and 300 K (*b*), liquid B_2O_3 at 4.0 ± 0.4 GPa and 1460 ± 20 K (*c*), high-density nonstoichiometric glass with the composition $B_2O_{2.6}$ quenched from the B_2O_3-based melt at 5.7 ± 0.4 GPa and 1800 ± 100 K in a graphite container (*d*), and high-density stoichiometric B_2O_3 glass mixed with new crystalline phase (its reflections are cut of), where the sample was quenched from the melt at 7.0 ± 0.5 GPa and 1900 ± 100 K in a thick Pt container (*e*).

imum at the pressures of 3.5 to 4.5 GPa (Fig. 1), which is possibly related to the attainment of a rigid and unstressed glassy state [22]. The activation energy for the glass crystallization process at $P = 1.3$ GPa is $E_{act} \approx 120 \pm 15$ kJ/mole. The crystallization temperatures of glasses prepared by quenching from melt under high pressure exceeds those for compressed pristine ordinary glass by 100 to 150 K (Fig. 1), indicating that the quenched high-pressure glasses are closer to the quasi-thermodynamic equilibrium state of glass at the corresponding pressures.

5. The typical x-ray diffraction patterns for the B_2O_3 glasses and liquid are shown in Fig. 2. The in situ structural study of liquid B_2O_3 displays diffuse transformation under pressure within the 0.5 to 2.5 GPa range, which is clearly supported by a noticeable growth of the residual densification of glasses obtained by quenching from melt (Figs. 3a, 3b). The compressed ordinary B_2O_3 glass at room temperature reveals noticeable partially irreversible changes of the short-range order structure (Figs. 2*a*, 2*b*), and the residual densification of quenched samples starts at pressure 5 to 6.5 GPa. At elevated temperatures $T > 500$ K, these irreversible changes start at 1 to 1.5 GPa. A comprehensive analysis

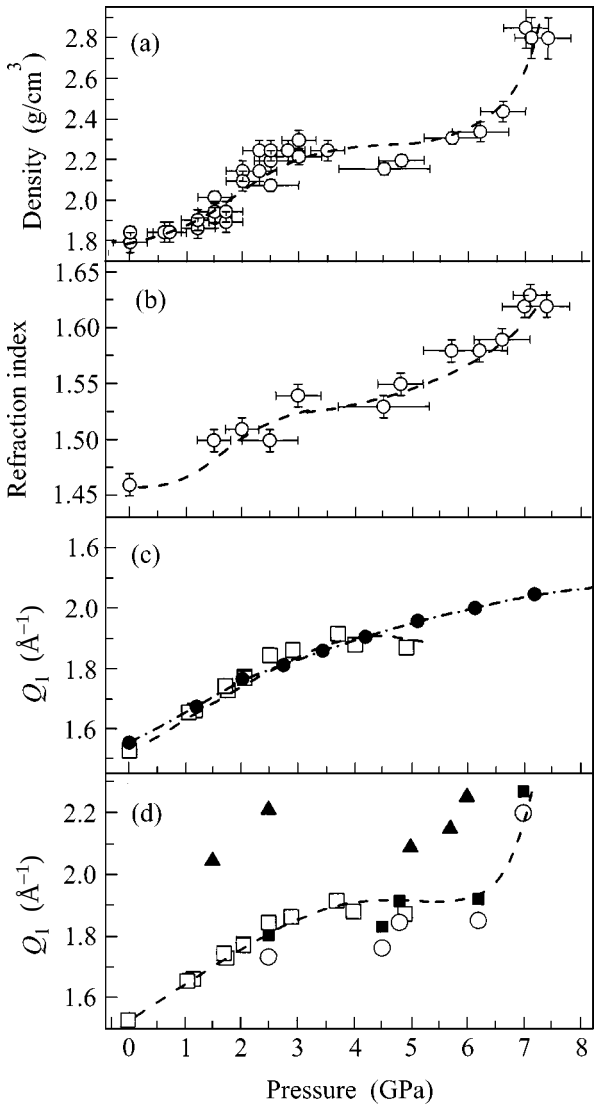

Fig. 3. Density (a) and refractive index (b) for B_2O_3 glasses quenched from the melt and position of the first x-ray diffraction peak for different cases (c) and (d) as functions of in situ pressure or pressure from which the sample was quenched (depending on the comments). (c) The in situ data for liquid near melting curve (open squares) and for compressed ordinary glass (solid circles) are compared. (d) The same data for liquid B_2O_3 as in (c) are compared with those for stoichiometric (open circles) and nonstoichiometric (solid triangles) glasses quenched from the melt to the normal conditions, where solid squares correspond to the extrapolation from the quenched glasses to in situ melt (see the text). All lines are guides to the eye.

of the structural data with the calculation of the radial distribution functions will be presented elsewhere.

The unusual pressure dependence of the position of the first x-ray diffraction peak at 3 to 5 GPa in the B_2O_3 liquid (Fig. 3c) shows that, besides the diffuse structural transformation at 0.5 to 2.5 GPa, one more liquid–liquid structural transformation is possible at higher

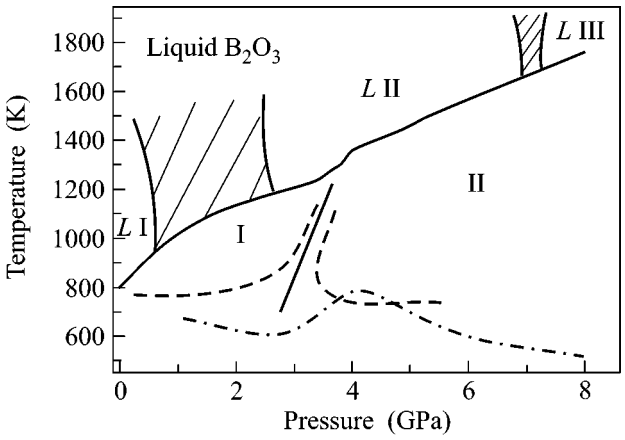

Fig. 4. Approximate regions of transformations in liquid B_2O_3 mapped on the pressure–temperature phase diagram of B_2O_3 (see details in Fig. 1).

pressures. To check this suggestion, we studied the structure and properties of B_2O_3 glasses prepared by quenching from melt at 1 to 7.5 GPa. The glasses obtained at 4.5 to 6.5 GPa have the density $\rho \approx 2.2$–2.4 g/cm^3, whereas the glasses obtained at $P > 7$ GPa have the density 2.8–2.9 g/cm^3, which exceeds the density of original glass by 55% (Fig. 3a). The x-ray diffraction study of these high-density glasses (Fig. 2*e*) points to substantial changes in the short-range order structure (Fig. 3d). Taking into account the compressibility of the glasses and their thermal expansion, it is possible to estimate the position of the first x-ray diffraction peak for the corresponding melts (Fig. 3d). The decrease of B_2O_3 melt viscosity under pressure [19] results in the formation of a crystal–glass mixture during quenching (10^3 K/s) instead of pure glass at $P >$ 4.5 GPa. At 4.5 to 6 GPa, the mixture of both crystalline modifications B_2O_3 I and B_2O_3 II together with glass was formed after rapid cooling, whereas at higher pressures the densest modification B_2O_3 II with a small part of glass admixture was obtained after melt quenching. The data obtained for the structure and density of the highly densified B_2O_3 glass strongly evidence the existence of one more sharp phase transition in liquid B_2O_3 at $P \approx 7 \pm 0.5$ GPa, accompanied by the volume anomaly $\Delta V/V \approx 20\%$ and a change in the short-range order structure. The high-density glass has a rather high index of refraction (Fig. 3b), $n \approx 1.61$–1.63 (the original glass has $n \approx 1.46$–1.47), which is in good agreement with the extrapolations of the refraction index vs. density dependence established in [23, 24]. This glass has unusually high stability at normal pressure, and upon heating it slowly transforms to the ordinary B_2O_3 melt at $T >$ 800 K. In this respect, the densified B_2O_3 glass obtained by pressure–temperature quenching from a solid state relaxes to the ordinary glassy state at temperatures 300 to 350 K at normal pressure, whereas the densified glasses prepared by quenching from melt at $P <$ 6.5 GPa lose their excessive density at 400 to 700 K. High stability of the high-density glass correlates with high thermal stability of the B_2O_3 II high-pressure phase at normal pressure, which also transforms to the B_2O_3 melt at $T \approx 800$ K without transition to the more stable B_2O_3 I phase.

6. If we use nonhermetic containers (graphite, *h*-BN, thin-wall Pt or Ta ampoules) for high temperature (>1700 K) experiments under pressure, a partial oxygen leakage results in nonstoichiometric composition of boron oxide. The composition of the quenched glasses in this case varies from B_2O_3 to B_2O with most reproducible composition around $B_2O_{2.5}$ (see example of x-ray diffraction in Fig. 2*d*). In *h*-BN and thin-wall Pt or Ta ampoules, oxygen leakage at heating occurs at $P > 5.5$ GPa, and in graphite containers it occurs at $P > 1.5$ GPa. Rapid quenching of the nonstoichiometric oxygen-depleted melt results in the formation of high-density glass with a density of 2.8 to 2.95 g/cm^3 and index of refraction of 1.62 to 1.65 in a wide region of synthesis pressure from 1.5 to 7 GPa. This glass has rather high hardness $H \approx 9.5$ GPa in comparison to that of the ordinary glass ($H \approx 3$ GPa). At normal pressure, this nonstoichiometric high-density glass is unusually stable; it crystallizes at $T \approx 1100$ K to new modifications and decomposes under melting at $T \approx 1250$ K. The results of the detailed study of the structure and properties of the nonstoichiometric high-density glasses and new boron oxide crystalline modifications will be presented elsewhere.

7. One can suppose that high-density B_2O_3 glass and the corresponding liquids contain a large fraction of fourfold coordinated boron atoms. Therefore, at least two structural transformations should occur in liquid and possibly in glassy B_2O_3 under compression (Fig. 4). The first diffuse transformation results in a decrease of the fraction of boroxol groups without noticeable changes in the first coordination spheres of B and O atoms. The second sharper transformation is accompanied by drastic changes in the short-range coordinations of B and O atoms. The influence of possible oxygen leakage for the second transition is not yet clear.

Thus, B_2O_3 is the first example of a substance, for which the in situ study was performed for both liquid and glassy states. The change of short-range order structure with the corresponding coordination increase seems to be a general phenomenon for crystalline, liquid, and glassy states. It would be of interest in the future to carry out an in situ structural study of liquid B_2O_3 up to 10 GPa and glassy B_2O_3 up to 20 GPa to elucidate the high-pressure structural transformations and to acquire quantitative information about coordination changes. These investigations, as well as comprehensive study of the structure and properties of high-density B_2O_3 glass, are now in progress.

The authors are grateful to Drs. R. Sadykov and T.I. Duyzheva for the help in structural study, to N.V. Kalyaeva and A.V. Gulyutin for their assistance in the synthesis and density measurements, Drs. Yu.M. Tsipenyuk and B.A. Chapyzhnikov for the chemical analysis of the oxygen content in B_2O_3 samples, as well as to Profs. O. Shimomura and S.M. Stishov for helpful discussions.

The work was supported by the Russian Foundation for Basic Research (project nos. 01-02-16557 and 02-02-16298), by JAERI project, and by JSPS.

REFERENCES

1. *New Kinds of Phase Transitions: Transformations in Disordered Substances*, Ed. by V. V. Brazhkin, S. V. Buldyrev, V. N. Ryzhov, and H. E. Stanley (Kluwer, Dordrecht, 2002), NATO Sci. Ser. II: Math. Phys. Chem., Vol. 81.
2. O. Mishima and Y. Suzuki, Nature **419**, 599 (2002).
3. Y. Katayama, *Gordon Research Conference on Research at High Pressure, Meriden, NH, USA* (2002), private communication.
4. O. B. Tsiok, V. V. Brazhkin, A. G. Lyapin, and L. G. Khvostantsev, Phys. Rev. Lett. **80**, 999 (1998).
5. F. S. El'kin, V. V. Brazhkin, L. G. Khvostantsev, *et al.*, Pis'ma Zh. Éksp. Teor. Fiz. **75**, 413 (2002) [JETP Lett. **75**, 342 (2002)].
6. J. Krong-Moe, J. Non-Cryst. Solids **1**, 269 (1969).
7. G. E. Gurr, P. W. Montgomery, C. D. Knutson, and B. T. Gorres, Acta Crystallogr. B **26**, 906 (1970).
8. C. T. Prewitt and R. D. Shannon, Acta Crystallogr. B **24**, 869 (1968).
9. J. D. Mackenzie and W. F. Claussen, J. Am. Ceram. Soc. **44**, 79 (1961).
10. F. Dachille and R. Roy, J. Am. Ceram. Soc. **41**, 78 (1959).
11. D. R. Uhlmann, J. F. Hays, and D. Turnbull, Phys. Chem. Glasses **8**, 1 (1967).
12. J. Swenson and L. Borjesson, Phys. Rev. B **55**, 11138 (1997).
13. J. D. Mackenzie, J. Am. Ceram. Soc. **46**, 461 (1963).
14. A. C. Wright, C. E. Stone, R. N. Sinclair, *et al.*, Phys. Chem. Glasses **41**, 296 (2000).
15. E. Chason and F. Spaepen, J. Appl. Phys. **64**, 4435 (1988).
16. Th. Gerber, B. Himmel, and J. Weigelt, J. Non-Cryst. Solids **126**, 35 (1990).
17. M. Misawa, J. Non-Cryst. Solids **122**, 33 (1990).
18. J. Diefenbacher and P. F. McMillan, J. Phys. Chem. A **105**, 7973 (2001).
19. V. V. Brazhkin and A. G. Lyapin, J. Phys.: Condens. Matter (in press).
20. M. Grimsditch, A. Polian, and A. C. Wright, Phys. Rev. B **54**, 152 (1996).
21. M. Grimsditch, R. Bhadra, and Y. Meng, Phys. Rev. B **38**, 7836 (1988).
22. K. Trachenko and M. T. Dove, J. Phys.: Condens. Matter **14**, 7449 (2002).
23. N. V. Surovtsev, J. Wiedersich, A. E. Batalov, *et al.*, J. Chem. Phys. **113**, 5891 (2000).
24. M. A. Ramos, J. A. Moreno, S. Vieira, *et al.*, J. Non-Cryst. Solids **221**, 170 (1997).

JETP Letters, Vol. 78, No. 6, 2003, pp. 398–401. From Pis'ma v Zhurnal Éksperimental'noĭ i Teoreticheskoĭ Fiziki, Vol. 78, No. 6, 2003, pp. 850–853.
Original English Text Copyright © 2003 by Yakovenko, Khodel.

Physics of the Insulating Phase in Dilute Two-Dimensional Electron Gas¶

V. M. Yakovenko[1, *] and V. A. Khodel[1, 2]

[1] *Condensed Matter Theory Center, Department of Physics, University of Maryland, College Park, Maryland 20742-4111, USA*

[2] *Russian Research Centre Kurchatov Institute, Moscow, 123182 Russia*

**e-mail: yakovenk@physics.umd.edu*

Received August 20, 2003

We propose to use the radiofrequency single-electron transistor as an extremely sensitive probe to detect the time-periodic ac signal generated by a sliding electron lattice in the insulating state of the two-dimensional electron gas. We also propose to use the optically-pumped NMR technique to probe the electron spin structure of the insulating state. We show that the electron effective mass and spin susceptibility are strongly enhanced by critical fluctuations of the electron lattice in the vicinity of the metal–insulator transition, as observed in experiment.© *2003 MAIK "Nauka/Interperiodica".*

PACS numbers: 73.20.-r; 85.35.Gv; 71.30.+h

Detecting electron lattice with the single-electron transistor. The metal–insulator transition (MIT) in the two-dimensional electron gas (2DEG) attracts considerable interest [1, 2]. In this paper, we focus on physics of the insulating phase. The great majority of experiments are transport measurements, and only a few are thermodynamic. Dultz and Jiang [3] measured compressibility κ of the 2DEG as a function of carrier concentration n and found that it tends to vanish in the insulating phase, i.e., the phase is incompressible. The experimental dependence $\kappa(n)$ was semiquantitatively reproduced within both the scenario of electron localization (E-LOC) in disordered potential [4] and the scenario of electron lattice (E-LAT) formation [5]. We use the term E-LAT to denote any state with local periodic modulation of electron density. The Wigner crystal (WC) and the charge-density wave (CDW) are the limiting cases of E-LAT, where the modulation amplitude is comparable to n and is much less than n, respectively. For simplicity, we call these carrier electrons, even though they may actually be holes.

Ilani *et al.* [6, 7] measured compressibility locally, using the single-electron transistor (SET) as a microscopic probe. They found that $\mu(n)$ has a series of quasirandom jumps, which become very strong in the insulating phase. These jumps were interpreted as single-electron charging events [6, 7] within the E-LOC scenario. Alternatively, the jumps can be interpreted as a manifestation of E-LAT [7]. When the average carrier concentration n is changed by the back gate, the period l of E-LAT must adjust, because it is proportional to the average distance between electrons $a = 1/\sqrt{n}$. However, because E-LAT is pinned by impurities, it cannot adjust its period continuously. Instead, E-LAT accumulates stress until it overcomes the pinning force and then makes a sudden local rearrangement of the lattice, which results in a jump of the local potential. Both the E-LOC and E-LAT scenarios are plausible, and it is difficult to decide between them on the basis of known experimental data. Here, we propose a modification of the experiments [6, 7], which may help to distinguish between the two scenarios.

In [8], Pudalov *et al.* observed a very nonlinear current–voltage (I–V) relation in the insulating phase of the 2DEG in Si-MOSFET. Almost no current I flows until electric field reaches the threshold field $\mathscr{E}_t$, and then I sharply surges at $\mathscr{E} > \mathscr{E}_t$, accompanied by broadband noise. Pudalov *et al.* interpreted their findings in terms of collective sliding of E-LAT depinned by the strong electric field $\mathscr{E} > \mathscr{E}_t$, which produces the large current I and generates the broadband noise due to local slip-stick motion. The I–V nonlinearity was found to be extremely sharp, with the differential conductivity increasing by a factor of 10^6, in the samples with the highest mobility and rounded in the samples with poor mobility [9]. These results suggest that the transition to the insulating state is not driven by disorder, as assumed by the E-LOC theories, but by E-LAT formation. The I–V nonlinearity was also observed in GaAs samples [10]. It was shown that the MIT deduced from the temperature dependence of resistivity is the same one as deduced from the I–V nonlinearity [11].

We propose to combine the SET experiment with the nonlinear I–V experiments. Suppose a strong pulling electric field $\mathscr{E} > \mathscr{E}_t$ is applied, and E-LAT slides.

¶ This article was submitted by the authors in English.

Then, the SET would register a time-periodic ac signal with the frequency $\nu = v/l$ produced by E-LAT of the spatial period l, which slides with the velocity v. This effect is nothing but the narrow-band noise (NBN), well-known for CDW in quasi-one-dimensional (Q1D) conductors [12]. Unlike in the Q1D conductors, attempts to observe the NBN in regular transport measurements in the 2DEG failed thus far [13]. We propose that the SET is a better tool for detecting the NBN, because of its very high sensitivity and because it is a local, microscopic probe, unlike the macroscopic current leads. In the experiment [7], the SET was situated at the distance $d = 400$ nm from the 2DEG. This distance is comparable to the average distance between the carriers $a = 1/\sqrt{n} = 100$ nm in the experiment [7] performed on p-GaAs with the typical hole concentration in the insulating phase $n = 10^{10}$ cm^{-2}. Because d and $l \sim a$ are comparable, the SET should experience a noticeable time-dependent signal when the periodically-modulated electron charge density slides past the SET. Reducing d and bringing the SET closer to the 2DEG would further increase sensitivity.

Let us estimate the frequency $\nu = v/l$ of the ac signal. The E-LAT period l is of the order of the average distance between the carriers $l \sim a = 1/\sqrt{n}$. The sliding velocity v is related to the current density $j = I/W = env$, where I is the total current and W is the transverse width of the sample. Thus, we find

$$\nu \simeq \frac{I}{e}\frac{1}{\sqrt{n}W} \simeq \left[6\ \frac{\text{MHz}}{\text{pA}}\right]\frac{I}{\sqrt{n}W}. \qquad (1)$$

For a crude estimate of the current density in the sliding regime, we use the data from [10] $j = I/W \simeq 0.4$ nA/0.4 mm = 1 nA/mm. (The data from [8] give a similar estimate.) Substituting these numbers into Eq. (1), we find $\nu \simeq 600$ kHz. The frequency scale is similar to that of the Q1D CDW [12]. Unfortunately, the frequency range of a typical SET is limited to less than 1 kHz. Thus, it is necessary to use the radiofrequency SET (RF-SET) [14], which can operate from dc up to 100 MHz. With this experimental setup, it should be possible to detect the ac signal at the frequency ν.

Equation (1) shows that ν is proportional to the current I carried by the sliding E-LAT, and the slope of that dependence is proportional to $1/\sqrt{n}$. An experimental observation of this effect would be the definitive proof of the existence of E-LAT in the dilute 2DEG. Periodicity in time is the direct consequence of periodicity in space, and the E-LOC scenarios cannot produce a periodic ac signal from the dc current. Although disorder destroys the long-range order of E-LAT [15, 16], the local periodicity is preserved and would produce the NBN peak in the Fourier spectrum. On the other hand, even if the RF-SET does not find a time-periodic signal, the measured time series would provide important microscopic information about electron conduction, such as the variable-range hopping. For example, uncorrelated single-electron hops would generate the Poisson stochastic process in the simplest case.

Probing spin order with the optically pumped NMR. Besides the question of charge ordering in the insulating state of the MIT, there is a question of spin ordering in that state. One of the great tools for obtaining information about electron spins is the nuclear magnetic resonance (NMR). In the quantum Hall regime, the optically-pumped NMR measurements on the ^{71}Ga nuclei in n-GaAs detected formation of skyrmions in the electron spin configuration for small deviations from the filling factor $\nu = 1$ [17]. In the $\nu = 1$ state, electrons are spontaneously spin-polarized and produce a significant effective magnetic field on the nuclei by means of hyperfine interaction. Thus, the NMR line of the nuclei in contact with the 2DEG experiences the measurable Knight shift proportional to the spontaneous spin polarization of electrons [17, 18].

We propose to use a suitable modification of the same method to study the spin properties of the 2DEG in the insulating state of a zero-effect magnetic field. A magnetic field is needed for NMR, but we want to eliminate its effect on electrons. This can be achieved by engineering a situation where the electron g-factor is zero. For example, this is the case for a magnetic field parallel to the [100] surface of p-GaAs [19, 20]. It is also possible to achieve $g = 0$ by applying hydrostatic pressure [21].

For the Wigner crystal, different types of spin ordering were proposed theoretically: ferromagnetic [22], antiferromagnetic [22], and various exotic orderings [15]. In the ferromagnetic state, the NMR line should experience a measurable Knight shift, detection of which would be the proof of spontaneous spin polarization of electrons. In the antiferromagnetic state, the NMR line would broaden, because the nuclei experience a staggered hyperfine field from the electrons. This method is routinely used to detect formation of spin-density waves (SDWs) in Q1D conductors [12]. On the other hand, when a strong electric field $\mathcal{E} > \mathcal{E}_t$ is applied, it forces SDWs or the E-LAT to slide. Then, the nuclei experience the time-averaged hyperfine magnetic field produced by electrons, and the NMR line becomes narrow again [23] (the so-called motion narrowing). An observation of these effects in NMR would provide a great deal of information about spin ordering of electrons in the insulating state and would put the ongoing theoretical discussion of the subject on firm experimental ground.

Enhancement of the effective mass and spin susceptibility. Experiments [2, 24–28] consistently show that the electron effective mass m^* and the effective spin susceptibility χ^* strongly increase when $n \longrightarrow n_c$ from the metallic side, where n_c is the critical density of the MIT. This phenomenon has a simple explanation within the E-LAT scenario. The theory was developed

in [29–31], and here we only briefly summarize the main physical idea.

The experiments [8, 9] show that the threshold field $\mathscr{E}_t$ and the thermal activation gap of resistivity continuously vanish at $n \longrightarrow n_c$. Thus, the phase transition between the metallic phase at $n > n_c$ and the insulating phase at $n < n_c$ is of the second order. More precisely, it was found to be slightly of the first order [32], as expected by the symmetry reasons for a triangular or hexagonal lattice [33]. These results are in qualitative agreement with the self-consistent Hartree–Fock calculations [5], which show that E-LAT continuously evolves from the CDW limit to the WC limit with the decrease of $n < n_c$.

Assuming that the system has a tendency to form E-LAT with the wave vector $q_c \sim 1/a$, we can write the charge response function $S_0(q) = S(q, w = 0)$ in the following form [33] in the vicinity of the phase transition for $n > n_c$:

$$S_0(q) \simeq \frac{C_1}{n - n_c + (q - q_c)^2}, \qquad (2)$$

where C_1 is a constant. Electrons can interact via exchange of the critical fluctuations (2). This interaction manifests itself in the Landau interaction function $f(\theta) \propto S_0(|\mathbf{p}_1 - \mathbf{p}_2|)$, where $\mathbf{p}_1$ and $\mathbf{p}_2$ are the momenta of the interacting electrons, and θ is the angle between $\mathbf{p}_1$ and $\mathbf{p}_2$. Substituting this formula in the Landau equation for the effective mass m^* [34], we find

$$\frac{1}{m^*} = \frac{1}{m} - C_2 \int \frac{\cos\theta d\theta}{n - n_c + (|\mathbf{p}_1 - \mathbf{p}_2| - q_c)^2}, \qquad (3)$$

where $C_2 \propto C_1$ is another constant. Taking into account that $|\mathbf{p}_1| = |\mathbf{p}_2| = p_F$, where p_F is the Fermi momentum, and assuming that $q_c \approx 2p_F$, we see that the integral in Eq. (3) is peaked around $\theta = \pi$, where $\cos\theta < 0$. Because of the Fermi statistics, the exchange interaction originating from the positive Coulomb repulsion is negative, so $C_2 < 0$. Thus, the interaction term in Eq. (3) causes an increase in the effective mass m^*, and this enhancement grows when $n \longrightarrow n_c$.

Specifically, taking $q_c = 2p_F$ we obtain

$$\frac{1}{m^*} = \frac{1}{m} - C_2 \int \frac{\cos\theta d\theta}{n - n_c + p_F^*(1 + \cos\theta)^2/4}. \qquad (4)$$

The integral in Eq. (4) diverges as $(n - n_c)^{-1/2}$ near $\theta \approx \pi$, and m^* diverges even earlier [29–31]:

$$\frac{m}{m^*} = 1 - \frac{C_3}{\sqrt{n - n_c}}, \qquad (5)$$

where $C_3 > 0$ is another constant. However, these divergences should not be taken too literally, because they would be cut off by the weakly first-order character of the phase transition [32]. Thus, m^* increases steeply when $n \longrightarrow n_c$, but does not necessarily go to infinity. The spin susceptibility is also enhanced via the standard relation $\chi^* = g^*m^*$. The qualitative agreement between the theory and experiment gives an argument in favor of the E-LAT scenario for the MIT in the 2DEG.

This theory is also applicable to other systems experiencing transition from a liquid to a crystalline phase. Such a transition is observed in the 2D ^{3}He, and the experiment [35] finds a very strong enhancement of m^* in the vicinity of the transition. Note that there is no disorder in liquid ^{3}He, so the E-LOC scenario is irrelevant in this case.

Conclusions. We propose to use the radiofrequency single-electron transistor (RF-SET) [14] as an extremely sensitive probe [6, 7] to detect the time-periodic ac signal generated by sliding E-LAT at $\mathscr{E} > \mathscr{E}_t$ in the insulating state of the 2DEG. An observation of this narrow-band-noise effect would be the definitive proof of E-LAT formation in the dilute 2DEG. We also propose to use the optically-pumped NMR technique [17] to probe the electron spin structure of the insulating state, which may have ferromagnetic, antiferromagnetic, or exotic types of spin ordering. NMR can be performed in a magnetic field without disturbing the electron spins in a situation where the electron g-factor is engineered to be zero [19, 21]. Within the Landau theory of Fermi liquids, we show that critical fluctuations of E-LAT near the MIT produce a strong enhancement of the effective mass m^* and spin susceptibility χ^* [29–31] in qualitative agreement with experiments in the 2DEG [24–28], as well as in the 2D ^{3}He [35]. This is an argument in favor of the E-LAT scenario.

Although we concentrated on physics of the 2DEG in zero magnetic field, the same ideas also apply to the Wigner crystal in a nonzero magnetic field perpendicular to the 2DEG [36, 37].

The authors are grateful to S. Das Sarma for critically reading the manuscript and giving many valuable comments and to V.M. Galitski for discussions. The authors thank the Kavli Institute for Theoretical Physics for the opportunity to start this collaboration. V.A.K. thanks the Condensed Matter Theory Center for arranging his visit to the University of Maryland.

This work was supported by NSF (grant nos. DMR-0137726 and PHY-0140316), by the McDonnell Center for Space Sciences, and by the Russian Ministry of Industry and Science (grant no. NS-1885.2003.2).

REFERENCES

1. E. Abrahams, S. V. Kravchenko, and M. P. Sarachik, Rev. Mod. Phys. **73**, 251 (2001).
2. S. V. Kravchenko and M. P. Sarachik, cond-mat/0309140.
3. S. C. Dultz and H. W. Jiang, Phys. Rev. Lett. **84**, 4689 (2000).
4. J. Shi and X. C. Xie, Phys. Rev. Lett. **88**, 086401 (2002).

5. S. Orozco, R. M. Méndez-Moreno, and M. Moreno, Phys. Rev. B **67**, 195109 (2003).
6. S. Ilani, A. Yacoby, D. Mahalu, and H. Shtrikman, Phys. Rev. Lett. **84**, 3133 (2000).
7. S. Ilani, A. Yacoby, D. Mahalu, and H. Shtrikman, Science **292**, 1354 (2001).
8. V. M. Pudalov, M. D'Iorio, S. V. Kravchenko, and J. W. Campbell, Phys. Rev. Lett. **70**, 1866 (1993).
9. V. M. Pudalov, J. Phys. IV **12**, Pr9-331 (2002).
10. J. Yoon, C. C. Li, D. Shahar, *et al.*, Phys. Rev. Lett. **82**, 1744 (1999).
11. A. A. Shashkin, S. V. Kravchenko, and T. M. Klapwijk, Phys. Rev. Lett. **87**, 266402 (2001).
12. G. Grüner, *Density Waves in Solids* (Addison-Wesley, New York, 1994).
13. Recently the NBN has been observed in the 2DEG in a high magnetic field in the quantum Hall regime, albeit with the frequency ν several orders of magnitude lower than given by Eq. (1); K. B. Cooper, J. P. Eisenstein, L. N. Pfeiffer, and K. W. West, Phys. Rev. Lett. **90**, 226803 (2003).
14. R. J. Schoelkopf, P. Wahlgren, A. A. Kozhevnikov, *et al.*, Science **280**, 1238 (1998).
15. S. Chakravarty, S. Kivelson, C. Nayak, and K. Voelker, Philos. Mag. B **79**, 859 (1999); K. Voelker and S. Chakravarty, Phys. Rev. B **64**, 235125 (2001).
16. B. Spivak, Phys. Rev. B **64**, 085317 (2001); Phys. Rev. B **67**, 125205 (2003).
17. S. E. Barrett, G. Dabbagh, L. N. Pfeiffer, *et al.*, Phys. Rev. Lett. **74**, 5112 (1995).
18. P. Khandelwal, N. N. Kuzma, S. E. Barrett, *et al.*, Phys. Rev. Lett. **81**, 673 (1998).
19. M. Rahimi, M. R. Sakr, S. V. Kravchenko, *et al.*, Phys. Rev. B **67**, 081302 (2003).
20. R. Winkler, S. J. Papadakis, E. P. De Poortere, and M. Shayegan, Phys. Rev. Lett. **85**, 4574 (2000).
21. W. Kang, J. B. Young, S. T. Hannahs, *et al.*, Phys. Rev. B **56**, R12 776 (1997); H. Cho, J. B. Young, W. Kang, *et al.*, Phys. Rev. Lett. **81**, 2522 (1998).
22. X. Zhu and S. G. Louie, Phys. Rev. B **48**, 13 661 (1993).
23. E. Barthel, G. Kriza, G. Quirion, *et al.*, Phys. Rev. Lett. **71**, 2825 (1993).
24. T. Okamoto, K. Hosoya, S. Kawaji, and A. Yagi, Phys. Rev. Lett. **82**, 3875 (1999).
25. A. A. Shashkin, S. V. Kravchenko, V. T. Dolgopolov, and T. M. Klapwijk, Phys. Rev. Lett. **87**, 086801 (2001); Phys. Rev. B **66**, 073303 (2002); cond-mat/0302004.
26. S. A. Vitkalov, M. P. Sarachik, and T. M. Klapwijk, Phys. Rev. B **65**, 201106 (2002).
27. V. M. Pudalov, M. E. Gershenson, H. Kojima, *et al.*, Phys. Rev. Lett. **88**, 196404 (2002).
28. O. Prus, Y. Yaish, M. Reznikov, *et al.*, Phys. Rev. B **67**, 205407 (2003).
29. V. R. Shaginyan, Pis'ma Zh. Éksp. Teor. Fiz. **77**, 104 (2003) [JETP Lett. **77**, 99 (2003)].
30. V. M. Galitski and V. A. Khodel, cond-mat/0308203.
31. V. A. Khodel, V. R. Shaginyan, and M. V. Zverev, Pis'ma Zh. Éksp. Teor. Fiz. **65**, 242 (1997) [JETP Lett. **65**, 253 (1997)].
32. V. M. Pudalov and S. T. Chui, Phys. Rev. B **49**, 14062 (1994).
33. S. A. Brazovskii, Zh. Éksp. Teor. Fiz. **68**, 175 (1975) [Sov. Phys. JETP **41**, 85 (1975)].
34. E. M. Lifshitz and L. P. Pitaevskiĭ, *Course of Theoretical Physics*, Vol. 9: *Statistical Physics* (Nauka, Moscow, 1978; Butterworth-Heinemann, Oxford, 1999), Part 2.
35. A. Casey, H. Patel, J. Nyéki, *et al.*, Phys. Rev. Lett. **90**, 115301 (2003).
36. H. W. Jiang, R. L. Willett, H. L. Stormer, *et al.*, Phys. Rev. Lett. **65**, 633 (1990); V. J. Goldman, M. Santos, M. Shayegan, and J. E. Cunningham, Phys. Rev. Lett. **65**, 2189 (1990); Y. P. Li, T. Sajoto, L. W. Engel, *et al.*, Phys. Rev. Lett. **67**, 1630 (1991); F. I. B. Williams, P. A. Wright, R. G. Clark, *et al.*, Phys. Rev. Lett. **66**, 3285 (1991); H. W. Jiang, H. L. Stormer, D. C. Tsui, *et al.*, Phys. Rev. B **44**, 8107 (1991).
37. B. G. A. Normand, P. B. Littlewood, and A. J. Millis, Phys. Rev. B **46**, 3920 (1992); X. Zhu, P. B. Littlewood, and A. J. Millis, Phys. Rev. B **50**, 4600 (1994).

JETP Letters, Vol. 78, No. 6, 2003, pp. 402–404. Translated from Pis'ma v Zhurnal Éksperimental'noĭ i Teoreticheskoĭ Fiziki, Vol. 78, No. 6, 2003, pp. 854–856.
Original Russian Text Copyright © 2003 by Zakharov, Zverev, Izotov.

Nature of EPR Line Asymmetry in $La_{0.70}Ca_{0.25}Ba_{0.05}MnO_3$

D. V. Zakharov*, D. G. Zverev, and V. V. Izotov

Kazan State University, Kazan, 420008 Tatarstan, Russia

**e-mail: Dmitri.Zakharov@ksu.ru*

Received August 21, 2003

It was pointed out in some works that asymmetry of an electron paramagnetic resonance (EPR) line is generally caused by both the electrical conduction and the nondiagonal elements of the dynamic susceptibility of a magnetic subsystem. Direct measurements of the temperature dependences of the conductivity and the EPR line shape in a $La_{0.70}Ca_{0.25}Ba_{0.05}MnO_3$ sample showed that the conduction makes the predominant contribution to the EPR line asymmetry © *2003 MAIK "Nauka/Interperiodica".*

PACS numbers: 75.47.Lx; 76.30.Fc; 76.30.Kg

Manganites, i.e., substances with the general formula $Ln_{1-x}A_xMnO_3$, where Ln is a rare-earth ion, and A is an alkaline-earth ion, have drawn much attention from researchers [1] because of their unusual electrical and magnetic properties. Another interesting feature of manganites is that some characteristics of their conduction are identical to those observed in the normal phase of cuprate-based high-temperature superconductors. However, particular interest in manganites arose when it was found that their isotope composition and an external magnetic field had an exceedingly strong effect on the electrical conduction in the vicinity of the Curie point [2, 3]. Electron paramagnetic resonance (EPR) is one of the effective methods for the investigation of manganites. It was shown in a number of works [4, 5] that the EPR line of manganites is asymmetric. Two alternative causes of this asymmetry were suggested: skin effect and the effect of the nondiagonal elements of dynamic susceptibility [8]. The goal of this work is to consider this alternative for a $La_{0.70}Ca_{0.25}Ba_{0.05}MnO_3$ single crystal.

The sample under study was provided by Professors J.-P. Clerc and J.-C. Grenet (France). It was prepared from a mixture of MnO_3, La_2O_3, $CaCO_3$, and $BaCO_3$. The concentration of MnO_3 in the mixture exceeded by 10% the required value to compensate Mn sublimation during heating. The mixture was heated for 12 h to 1450°C and then slowly cooled at a rate of 0.2 K/min. Then, a cylindrical sample was grown by zone melting. X-ray structural analysis revealed a single pseudocubic phase with slight monoclinic distortions. The lattice parameters were: $a = 7.783 \pm 0.001$ Å, $b = 7.787 \pm 0.001$ Å, $c = 7.782 \pm 0.001$ Å, and $\beta = 89.838 \pm 0.002°$. The sample under study had the shape of a disk 3.9 mm in diameter and 0.8 mm thick. It was cut so that one of the crystallographic axes was perpendicular to the disk plane.

Experiment. Constantan plates were deposited on parallel faces of the cylindrical sample. A pair of wires were soldered on each plate to create a four-wire resistance measuring circuit. Magnetoresistance (MR) and dc resistivity were measured using a B7-34A universal digital voltmeter. The results of measuring the dc resistivity at 1 mA in a temperature range from 77 to 460 K are given in Fig. 1. The temperature dependences of electrical resistivity in a magnetic field of 15 kOe and of the magnetoresistance are also shown in Fig. 1. It can be seen that, at temperatures $T > 230$ K, the resistivity is independent of the magnetic field. Thus, the asymmetry of the EPR line in the field $H_{res} \cong 3.4$ kOe can be calculated using the value of zero-field resistivity.

The EPR spectra of the sample under study were measured using a Bruker ESP 300 commercial 3-cm-range spectrometer. Measurements in a temperature

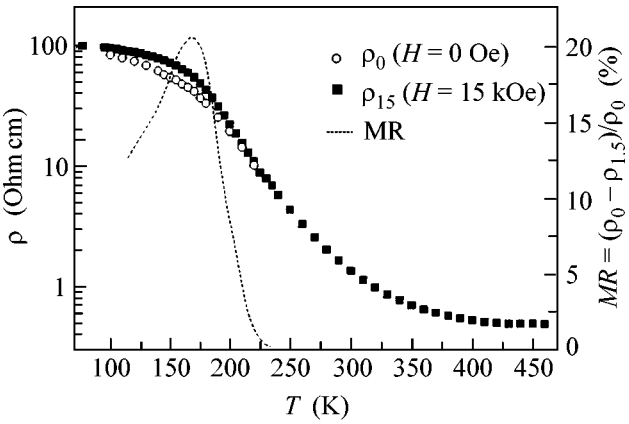

Fig. 1. Temperature dependence of the dc resistivity of $La_{0.70}Ca_{0.25}Ba_{0.05}MnO_3$ at 1 mA in a magnetic field of 15 kOe and in zero magnetic field. The dot line is the temperature dependence of the magnetoresistance.

0021-3640/03/7806-0402$24.00 © 2003 MAIK "Nauka/Interperiodica"

range from 100 to 460 K were made in an ER 4111 VT EPR nitrogen cryostat with a temperature accuracy of ±0.5 K. The sample was glued to a high-purity quartz rod. The EPR spectrum reflects the dependence of the absorbed microwave energy P on the external static magnetic field H. Usually, spectrometers record the derivative dP/dH to increase the signal-to-noise ratio. Typical EPR spectra for the compound under consideration are shown in Fig. 2.

Results and discussion. A broad exchange-narrowed absorption line was observed in the paramagnetic range $T > 230$ K. This line is well described by the Dyson equation [6, 7]:

$$\frac{dP}{dH} \propto \frac{d}{dH}\left\{\frac{\Delta H + \alpha(H - H_{res})}{(H - H_{res})^2 + \Delta H^2}\right\}. \quad (1)$$

This is an asymmetric line of Lorentz shape. Equation (1) takes into account the energy dispersion in the sample: α is the dispersion-to-absorption ratio (D/A).

Such asymmetric line shapes are usually observed in metals, where, due to the skin effect, dispersion is admixed to the absorption spectra. For samples small compared to the skin depth $\delta \cong \sqrt{\rho/\mu_o w}$, a symmetric absorption line ($\alpha = 0$) is expected. On the contrary, if a sample is large compared to the skin depth, absorption and dispersion are of equal strength ($\alpha \approx 1$), leading to the strong asymmetry of the resonance line. The second possible cause of asymmetry (especially typical for insulators) is due to the effect of nondiagonal elements of the dynamic susceptibility, which leads to a characteristic distortion of the absorption line shape. This distortion depends on the frequency and orientation of the exciting microwave field [8] and can be approximated using Eq. (1).

The EPR line of the compound under study is isotropic; the resistivity of the crystal varies from 4.73 Ω cm at 245 K to 0.49 Ω cm at 450 K, which corresponds to the skin depth $\delta \cong 0.8$–0.26 mm. Thus, to reveal the correlation between the resistivity and the EPR line asymmetry, EPR spectra were measured in an external microwave field H_1 applied parallel and perpendicular to the plane of the sample. In the first case, the size of the sample is 5 times greater than the skin depth, which should lead to a considerable EPR line asymmetry without any significant temperature dependence. Experiments showed that the ratio α was indeed close to unity over the entire temperature range and slowly increased with increasing temperature. In the second case (H_1 perpendicular to the plane of the 0.8-mm thick disk sample), the skin depth becomes comparable to the sample size at 245 K; as the temperature increases, the skin depth is reduced by a factor of ~3. The correlation between the sample resistivity and the EPR line asymmetry can be revealed by comparing their temperature dependences. Taking into account that $\alpha \sim 1/\delta \sim 1/\sqrt{\rho}$, the comparison was performed between the temperature dependences of these two values (Fig. 3). This allows one to conclude that the absorption line becomes asymmetric due to the skin effect.

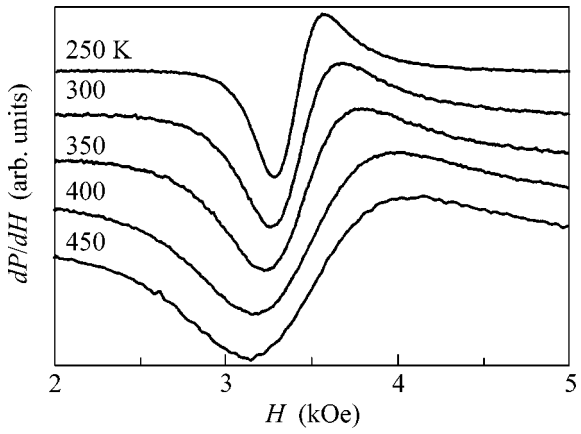

Fig. 2. Typical EPR spectra for $La_{0.70}Ca_{0.25}Ba_{0.05}MnO_3$ at different temperatures.

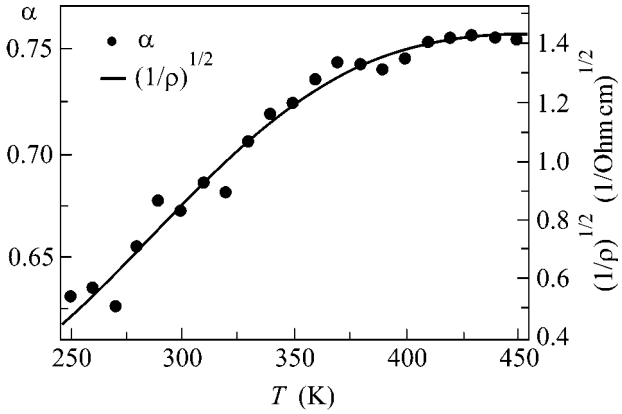

Fig. 3. Comparison of the temperature dependences of the EPR line asymmetry parameter α and $\sqrt{1/\rho(H_{res})}$ for $La_{0.70}Ca_{0.25}Ba_{0.05}MnO_3$.

It should be noted that the nondiagonal elements of the dynamic susceptibility probably also have an effect on the absorption line asymmetry. However, this effect is weaker and manifests itself only in very broad lines ($H_{res} \approx \Delta H$). It can be observed, for example, in $La_{0.95}Sr_{0.05}MnO_3$, where the asymmetry parameter D/A assumes, in some cases, negative values, which cannot be explained by the skin effect.

We are grateful to Professors J.-P. Clerc and J.-C. Grenet for the single-crystal sample, Yu.K. Rosenzweig for assistance in preparation of the sample for measuring resistivity, and M.V. Eremin and E.A. Gan'shina for stimulating discussion.

This work was supported by the State Program "Universities of Russia" (project no. UR.01.01.023)

and the Russian Foundation for Basic Research (project no. 03-02-17430). D.V. Zakharov is grateful to the Civilian Research and Development Foundation (grant no. BRHE REC-007) for support.

REFERENCES

1. E. Dagotto, T. Hotta, and A. Moreo, Phys. Rep. **344**, 1 (2001).
2. É. L. Nagaev, Usp. Fiz. Nauk **166**, 833 (1996) [Phys. Usp. **39**, 781 (1996)].
3. J. M. D. Coey, M. Viret, and S. von Molnar, Adv. Phys. **48**, 167 (1999).
4. V. A. Ivanshin, J. Deisenhofer, H.-A. Krug von Nidda, *et al.*, Phys. Rev. B **61**, 6213 (2000).
5. J. Deisenhofer, M. V. Eremin, D. V. Zakharov, *et al.*, cond-mat/0108515 (2001).
6. F. J. Dyson, Phys. Rev. **98**, 349 (1955).
7. S. E. Barnes, Adv. Phys. **30**, 801 (1981).
8. H. Benner, M. Brodehl, H. Seitz, and J. Wiese, J. Phys. C **16**, 6011 (1983).

Translated by K. Chamorovskiĭ

JETP Letters, Vol. 78, No. 6, 2003, pp. 405–407. Translated from Pis'ma v Zhurnal Éksperimental'noĭ i Teoreticheskoĭ Fiziki, Vol. 78, No. 6, 2003, pp. 857–859.
Original Russian Text Copyright © 2003 by Sekatskiĭ.

Preparation of Entangled Spin States for a Free Electron and Nucleus by Resonance Laser Photoionization

S. K. Sekatskiĭ

Institut de Physique de la Matière Condensée, Université de Lausanne, BSP, CH 1015 Lausanne–Dorigny, Switzerland
Institute of Spectroscopy, Russian Academy of Sciences, Troitsk, Moscow region, 142190 Russia
e-mail: Sergey. Sekatskii@ipmc.unil.ch

Received July 31, 2003

The method of preparing entangled quantum spin states of a free electron and nucleus by laser resonant step photoionization of free atoms is proposed and analyzed. *© 2003 MAIK "Nauka/Interperiodica".*

PACS numbers: 03.65.Ud; 32.80.Fb; 32.10.Fn; 03.67.-a

In recent years, quantum information science has been intensively studied, because it provides, in principal, the possibility of computing ("computability") the problems that cannot be solved in a reasonable time by any classical algorithm, allows the creation of information channels that are fundamentally protected from eavesdropping, etc. (see, e.g., [1–3]). For many applications of quantum information, an important role is played by the nonlocal entangled states of many-particle quantum systems—the states whose wave function cannot be represented as a direct product of the wave functions of their subsystems (a good review can be found in [4]). One classical example of such states is given by the famous Einstein–Podolsky–Rosen's pair of particles flying apart [5] and its spin modification analyzed by Bohm in [6]: two particles with spins 1/2 in a singlet state with the total spin equal 0. However far these particles fly apart in space, they are still described by the nonlocal collective wave function

$$|S = 0\rangle = \frac{1}{\sqrt{2}}(|s_1 = 1/2\rangle|s_2 = -1/2\rangle - |s_1 = -1/2\rangle|s_2 = 1/2\rangle),$$

for which neither of the particles can be assigned a certain spin projection s_1 or s_2.

Apart from quantum computers, the nonlocal entangled states are used in teleportation, in checking Bell's inequalities, etc., and many schemes of generating such states have been suggested and practically implemented [1–4]. The purpose of this paper is to propose and analyze the methods of preparing the entangled states for two spins of different nature, namely, nuclear and electron spins. It will be shown that these states can be efficiently produced by using an appropriate scheme of laser resonant multistep atomic-beam photoionization with allowance for hyperfine splitting.

The experimental scheme for creating the indicated entangled states is a conventional scheme of high-resolution laser resonant multistep atomic photoionization. A particular example of such experiments is given, e.g., in our work [7]; see also monograph [8] for a review of the whole method.

We first consider the stable thallium $^{203,\,205}$Tl isotopes, both having nuclear spin $I = 1/2$. At the first photoionization step, it is natural to use the resonance $6^2P_{1/2}$–$7^2S_{1/2}$ transition at a wavelength of 377.6 nm that is well mastered by the present-day laser technique. At this step, neither the polarization nor the narrow-band (high-resolution) laser radiation is required; i.e., all hf components of the upper $7^2S_{1/2}$ level are equally occupied. At the second resonant-photoionization step, light polarization is again immaterial, but the spectral line should be rather narrow for the optical transition to terminate at the $n^2P_{1/2}$ (n = 8, 9, …) state on its $F = 0$ hfs sublevel (conventional notation $F = I + J$ is used; since the 0–0 transition is known to be forbidden, the atom should initially be in the $F = 1$ state. The desired laser wavelengths for these and the other transitions discussed in this work can be found from the literature and, thus, are omitted for brevity). To my knowledge, the data on the hf splitting of the corresponding upper $n^2P_{1/2}$ (n = 8, 9, …) levels are lacking in the literature; however, based on the $6^2P_{1/2}$ hf splitting (12.2 and 12.3 GHz for the ^{203}Tl and ^{205}Tl isotopes, respectively; see, e.g., [9] and references cited therein), together with the well-known trend toward a decrease in the hf splitting with increasing principal quantum number n (see, e.g. [10]) and the characteristic spectral resolution (on the order of 100 MHz [7, 8]) of the photoionization experiment in the geometry of a perpendicular atomic beam, one can anticipate that this excitation should present no problems.

As a result of this procedure, an atom occurs in the $n^2P_{1/2}$ ($F = 0$) state, which, being a combination of the I and J states, is the entangled Bell's (as well as Bohm's)

state of a nuclear spin and the total angular momentum of valence electron:

$$h1 = \frac{1}{\sqrt{2}}(|m_J = 1/2\rangle|m_I = -1/2\rangle - |m_J = -1/2\rangle|m_I = 1/2\rangle),$$

The next step consists in using the linearly polarized laser radiation for inducing the atomic transition to the Rydberg $N^2S_{1/2}$ level (N is on the order of twenty to thirty) followed by its ionization in a (quasi)static electric field [8]. The hf interaction in this highly excited state is negligible [10]; in other words, the I–J coupling is broken: the optical transition does not change nuclear spin and its projection and only changes J and m_J (this situation is quite analogous to the production of polarized electrons in photoionization: if the L–S coupling in the continuum or autoionizing state is inefficient, only the electron orbital moment L, and not its spin S, changes upon the corresponding optical transition (see, e.g., [11])). The linearly polarized laser radiation changes the projection m_J by ±1, and, hence, the $m_J = -1/2$ state undergoes a transition to $m_J = +1/2$. Since $L = 0$ and $J = S$ for the $N^2S_{1/2}$ level, $m_J = +1/2$ implies that $m_s = +1/2$. Similarly, the initial $m_J = +1/2$ state undergoes transition to $m_s = -1/2$. In turn, the subsequent electric-field-induced atomic ionization does not change spins (both nuclear and electron) and changes only the electron orbital moment.

Therefore, after the above-mentioned procedures, one obtains a free electron and a free ion whose spin state is described by the entangled wave function

$$h2 = \frac{1}{\sqrt{2}}(|m_s = -1/2\rangle|m_I = -1/2\rangle - |m_s = 1/2\rangle|m_I = 1/2\rangle).$$

This function is not an eigenfunction of the operator $I + S$ of the total spin, but has all characteristic features of a nonlocal state described by Einstein–Podolsky–Rosen–Bohm in [5, 6]; an individual particle cannot be assigned any certain spin projection, while the measurement of this projection changes the state of the other particle.

The entangled state for the nuclear spin 3/2 can be produced in a similar way. In this respect, the stable gallium ^{69,71}Ga isotopes are a suitable system. The hf-splitting data for the gallium isotopes can be found in [12–14]. Without specifying the situation, we recall that the hf splitting and spectral resolution of a laser multistep photoionization experiment in the geometry of perpendicular atomic beam are such that the hf- resolved transitions in gallium atoms can occur at the first two photoionization steps.

In this case, a circularly polarized (for definiteness, σ^+) narrow-band radiation inducing the $F = 1 - F = 1$ transition must be used even at the first $4^2P_{1/2}$–$5^2S_{1/2}$ photoionization step at a wavelength of 403.4 nm. Taking into account the selection rules $\Delta m_F = +1$ for the F projection, one has $m_F = 0, +1$ in the excited state. Next, at the second photoionization step we also use the σ^+ laser radiation to induce the $F = 1 - F = 1$ transition between the $5^2S_{1/2}$ and $n^2P_{1/2}$ ($n = 6, 7, \ldots$) levels, resulting in a state with $m_F = +1$. In I and J terms, this is an entangled state of a nuclear spin and the total electron angular momentum

$$h3 = \frac{\sqrt{3}}{2}|m_J = -1/2\rangle|m_I = 3/2\rangle - \frac{1}{2}|m_J = 1/2\rangle|m_I = 1/2\rangle$$

(the coefficients are the corresponding Clebsch–Gordan factors). Similar to the above-mentioned thallium isotopes, the following entangled spin state of a free electron and nucleus is obtained upon the linearly polarized radiation inducing the transition to the Rydberg $N^2S_{1/2}$ state followed by the electric-field-induced ionization:

$$h4 = \frac{\sqrt{3}}{2}|m_s = 1/2\rangle|m_I = 3/2\rangle - \frac{1}{2}|m_s = -1/2\rangle|m_I = 1/2\rangle.$$

The generation of entangled states for the nuclear spin $I = 1$ can be illustrated by the example of stable ^{6}Li isotope. In this case, one can use a two-step laser resonant photoionization scheme. At the first step, the σ^+-polarized laser radiation induces the $2^2S_{1/2}$–$2^2P_{1/2}$, $F = 1/2 \longrightarrow F = 1/2$ transition. For the indicated levels, the lithium hf splitting is small (228 and 26 MHz; see [15] and references therein), but, as was demonstrated experimentally in [15], it is quite sufficient for the spectral resolution of all hfs components in the geometry of well-collimated perpendicular atomic beam.

After the first photoionization step, lithium atoms occur in a state with projection $m_F = +1/2$, which can be written in I and J terms as

$$h5 = \frac{\sqrt{2}}{\sqrt{3}}|m_J = -1/2\rangle|m_I = 1\rangle - \frac{1}{\sqrt{3}}|m_J = 1/2\rangle|m_I = 0\rangle.$$

The second quantum of the linearly polarized laser radiation carries it to the Rydberg $N^2S_{1/2}$ state, whose ionization by a quasi-static electric field gives rise to

the following entangled spin state of an electron and nucleus:

$$h6 = \frac{\sqrt{2}}{\sqrt{3}}|m_s = 1/2\rangle|m_I = 1\rangle - \frac{1}{\sqrt{3}}|m_s = -1/2\rangle|m_I = 0\rangle.$$

Thus, I have demonstrated that the entangled spin states of a free electron and nucleus can be efficiently created without difficulty by laser resonant step atomic ionization. Of course, the examples presented in this work cover neither the list of atoms suitable for creating the appropriate entangled states nor the corresponding photoionization schemes. These schemes can be used similarly to the other entangled states that are actively elaborated today. In particular, due to the nonlocality (the uncoupled electron and ion rapidly fly apart at macroscopically large distances), the nuclear spin-state (a system much more complicated than a photon) teleportation using the corresponding entangled electron as an ancila (auxiliary quantum system) is of considerable interest; cf. [1–4].

REFERENCES

1. M. Nielsen and I. Chuang, *Quantum Computation and Quantum Communication* (Cambridge Univ. Press, Cambridge, 2000).
2. C. H. Bennet and D. P. DiVincenzo, Nature **404**, 247 (2000).
3. *Quantum Computation and Quantum Information*, Ed. by C. Macchiavello, G. M. Palma, and A. Zeilinger (World Sci., Singapore, 2001).
4. I. V. Bargatin, B. A. Grishanin, and V. N. Zadkov, Usp. Fiz. Nauk **171**, 625 (2001) [Phys. Usp. **44**, 567 (2001)].
5. A. Einstein, B. Podolsky, and N. Rosen, Phys. Rev. **47**, 777 (1935).
6. D. Bohm, *Quantum Theory* (Prentice Hall, Englewood Cliffs, N.J., 1951; Nauka, Moscow, 1965).
7. V. I. Mishin, S. K. Sekatskiĭ, V. N. Fedoseev, *et al.*, Zh. Éksp. Teor. Fiz. **93**, 410 (1987) [Sov. Phys. JETP **66**, 235 (1987)].
8. V. S. Letokhov, *Photoionization Laser Spectroscopy* (Nauka, Moscow, 1986).
9. D. S. Richardson, R. N. Lyman, and P. K. Majumder, Phys. Rev. A **62**, 012510 (2000).
10. L. Armstrong, *Theory of the Hyperfine Structure of Free Atoms* (Wiley, New York, 1971).
11. J. Kessler, *Polarized Electrons* (Springer, Berlin, 1976; Mir, Moscow, 1988).
12. S. Krenn, W. Scherf, O. Khait, *et al.*, Z. Phys. D **41**, 229 (1997).
13. J. H. M. Neijzen and A. Doenszelmann, Physica C (Amsterdam) **98**, 235 (1980).
14. A. Lurio and A. G. Prodell, Phys. Rev. **101**, 79 (1956).
15. J. Walls, R. Ashby, J. J. Clarke, *et al.*, Eur. Phys. J. D **22**, 159 (2003).

Translated by V. Sakun

JETP Letters, Vol. 78, No. 6, 2003, pp. 408–412. Translated from Pis'ma v Zhurnal Éksperimental'noĭ i Teoreticheskoĭ Fiziki, Vol. 78, No. 6, 2003, pp. 860–864.
Original Russian Text Copyright © 2003 by Balykin.

Atom Nanoprobe with a Single Photon

V. I. Balykin

Institute of Spectroscopy, Russian Academy of Sciences, Troitsk, Moscow region, 142190 Russia
Institute for Laser Science, University of Electro-Communications, Chofu-Shi, 182 8585 Tokyo, Japan
e-mail: balykin@isan.troitsk.ru, balykin@ils.uec.ac.jp

Received August 12, 2003

The possibility of detecting an atom by a single photon with nanometer spatial resolution and nanosecond time resolution is studied. © *2003 MAIK "Nauka/Interperiodica".*

PACS numbers: 39.25.+k; 81.16.Ta

The use of a photon for the detection of a single quantum object in gedanken experiments was discussed by Heisenberg and von Neumann [1, 2] as early as in the 1920s in the context of quantum mechanical restrictions on the action of quantum mechanical measurement on a measured object. Owing to the recent development of optical and laser technologies, experiments on the investigation of the action of a single photon (localized in the cavity mode) on a single atom have become possible [3]. The light field in the mode of a high-Q cavity with energy on the order of one photon makes it possible to detect and localize single atoms [4, 5]. There are several proposals for using the light field in the high-Q cavity for the detection of an atom with a spatial resolution better than the light wavelength [6–10]. The position of an atom in the standing light wave of a high-Q cavity closely correlates with the wave phase, because the atom is polarized in the light field which, in turn, changes the light-wave phase. The measurement of a change in the light-wave phase when the atom passes through the light field provides information about the atomic position with respect to the standing-wave antinode. Spatial overlap of the atomic wave packet with the light-field mode restricts the spatial resolution of this method [11].

In this work, we analyze the possibility of using the light field with single-photon energy for the detection of a single atom with nanometer spatial resolution and nanosecond time resolution. Figure 1 shows the layout of such an atom nanoprobe. A high-Q optical cavity is formed by two mirrors M_1 and M_2. Laser radiation enters into the cavity through the mirror M_2. The mirror M_1 has a hole with diameter $2a$, which is much smaller than the wavelength of radiation entering the cavity. Such a hole is called the Bethe hole [12]. As will be shown below, it does not noticeably change the cavity Q factor. The atom can penetrate into the cavity through this hole and interact with the light field of the cavity mode. The atom inside the cavity mode changes the resonant properties of the cavity, and a fraction of laser radiation is reflected from the cavity. The reflected radiation is detected by a photodetector. A photodetector signal carries information about the atom inside the cavity mode. The spatial resolution of such an atom probe is determined by the hole size, whose minimum size is limited by the atomic size and the characteristic length of interatomic interaction; i.e., it lies in the nanometer range. The time resolution of the atom nanoprobe is no worse than the atomic time of flight through the cavity and lies in the nanosecond range for the cavity length $l_r = \lambda/2$ and thermal atomic velocities. The volume of atomic localization is $V \simeq -\pi a^2 l \ll \lambda^3$. As will be shown below, the light-field energy of one photon is sufficient for the reliable detection of an atom in the nanoprobe.

The behavior of the system atom + cavity is primarily determined by four parameters: (i) the coupling constant g_0 (single-photon Rabi frequency), (ii) the radiative width 2γ of atomic transition, (iii) the cavity decay rate κ, and (iv) the time of interaction between the atom and the cavity-field mode. A single atom can noticeably change the resonant properties of the cavity

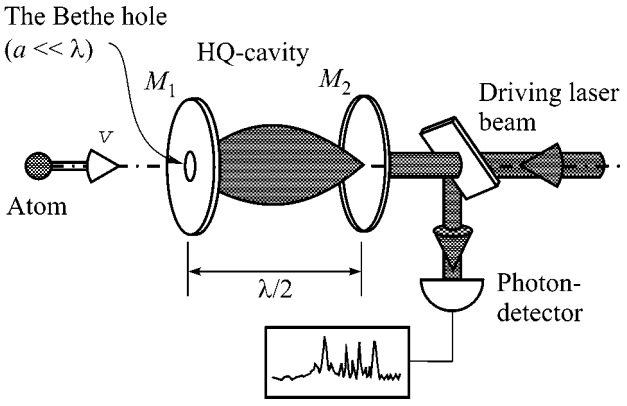

Fig. 1. Layout of an atom nanoprobe.

0021-3640/03/7806-0408$24.00 © 2003 MAIK "Nauka/Interperiodica"

only in the so-called good cavity limit and in the strong-coupling regime ($g_0 \gg \gamma, \kappa$) [13]. When the frequency of laser radiation coincides with the cavity-mode frequency, the cavity is transparent to the radiation and, therefore, the reflected radiation on the photodetector is absent. The presence of the atom in such a cavity noticeably changes the resonant frequency and, as a result, laser radiation is reflected from the cavity.

Let us consider the qualitative dynamics of interaction between a two-level atom and the light field of the cavity mode. The cavity-field mode is assumed to be in the coherent state $|\alpha_0\rangle$, which has complex amplitude $\alpha_0 = |\alpha_0|e^{i\varphi_0}$ and is excited by an external laser. In this case, the Hamiltonian of interaction between the atom and field has the form [14]

$$\hat{H} = \frac{1}{2}\hbar\omega_a\sigma_z + \hbar\omega_c a^+ a + iv(t)g(a^+\sigma_- - a\sigma_+) + \hat{H}_R + \hat{H}_D. \quad (1)$$

Here, ω_a and ω_c are the atomic-transition frequency and eigenfrequency of the cavity mode, respectively; $\sigma_z = |e\rangle\langle e| - |g\rangle\langle g|$, where $|e\rangle$ and $|g\rangle$ are the eigenstates of the Hamiltonian of the unperturbed atom; they correspond to the excited and ground atomic levels, respectively; a^+ and a are the creation and annihilation operators of the cavity-field mode, respectively; and $g = g_0 f(r)$ is the coupling constant of the cavity mode, where the function $f(r)$ describes the spatial distribution of the cavity-field mode in the standing light wave with the Gaussian transverse profile and allowance for a change in the standing-wave field on the Bethe hole [15], and

$$g_0 = \frac{\mu\varepsilon_0}{\hbar} = \mu\sqrt{\frac{\omega_c}{2\hbar\epsilon_0 V}}.$$

Here, μ is the matrix element of the dipole atomic transition moment, ϵ_0 is the permittivity of free space, and ε_0 is the so-called vacuum electric field. The Hamiltonian $\hat{H}_R$ describes the coupling of the atom with other modes through spontaneous radiation. The Hamiltonian H_D describes the mode excitation by the external laser. The function $v(t) = \begin{cases} 1, & 0 \le t \le t_{\text{fl}} \\ 0, & t_R \le t \le 0 \end{cases}$ describes the switching-on and switching-off of the interaction between the atom and the field mode, where t_{fl} is the time of flight of the atom through the cavity. For the very short cavity ($l = \lambda/2$) under consideration, the interaction time is much shorter than both the atomic excited-state spontaneous lifetime and the characteristic cavity decay time ($t_r = 1/\kappa$). In this case, the spontaneous decay of the excited atomic state can be ignored, and the role of external laser radiation reduces to the formation of the initial state for the cavity-field mode before the atom enters the cavity. Thus, the dynamics of the system atom + cavity is fully determined by the first three terms in Hamiltonian (1). The time evolution of the system is described by the Schrödinger equation [14]

$$i\hbar\frac{\partial|\Psi\rangle}{\partial t} = \hat{H}|\Psi\rangle \quad (2)$$

with the state vector

$$|\Psi\rangle = \sum_n [c_{e,n}(t)|e, n\rangle + c_{g,n}(t)|g, n\rangle], \quad (3)$$

where $|e, n\rangle$ is the state of the system with an atom in the excited state $|e\rangle$ and n photons in the field mode. The state $|g, n\rangle$ is the state of the system with an atom in the ground state $|g\rangle$ and n photons in the field mode. The equations for the amplitudes $c_{e,n}$ and $c_{g,n}$ can be obtained by substituting Hamiltonian (1) into Eq. (3) [14]; in the interaction representation, they take the form

$$\dot{c}_{e,n} = -ig\sqrt{n+1}e^{+i\delta t}c_{g,n+1}, \quad (4.1)$$

$$\dot{c}_{g,n+1} = -ig\sqrt{n+1}e^{-i\delta t}c_{e,n}, \quad (4.2)$$

where $\delta = \omega_a - \omega_c$. Under the assumption that the atom is initially in the ground state, the solution to Eqs. (4) has the form

$$c_{e,n}(t) = -c_{n+1}(0)\frac{2ig\sqrt{n+1}}{\Omega_n}\sin\left(\frac{\Omega_n t}{2}\right)e^{i\delta t/2}, \quad (5.1)$$

$$c_{g,n+1}(t) = c_{n+1}(0)\left[\cos\left(\frac{\Omega_n t}{2}\right) + \frac{i\delta}{\Omega_n}\sin\left(\frac{\Omega_n t}{2}\right)\right]e^{-i\delta t/2}, \quad (5.2)$$

where $\Omega_n = \sqrt{4g^2(n+1) + \delta^2}$ is the generalized Rabi frequency.

The probability of the presence of n photons in the cavity modes in the presence of the atom is determined by the expression

$$P(n, t) = |c_{e,n}(t)|^2 + |c_{g,n}(t)|^2 = |c_{n+1}(0)|^2\frac{4g^2(n+1)}{\Omega_n^2}\sin^2\left(\frac{\Omega_n t}{2}\right) + |c_n(0)|^2\left[\cos^2\left(\frac{\Omega_{n-1}t}{2}\right) + \frac{\delta^2}{\Omega_{n-1}^2}\sin^2\left(\frac{\Omega_{n-1}t}{2}\right)\right]. \quad (6)$$

The average number of photons in the cavity at time t is equal to

$$\langle n(t)\rangle = \sum_{n=0}^{\infty} nP(n, t). \quad (7)$$

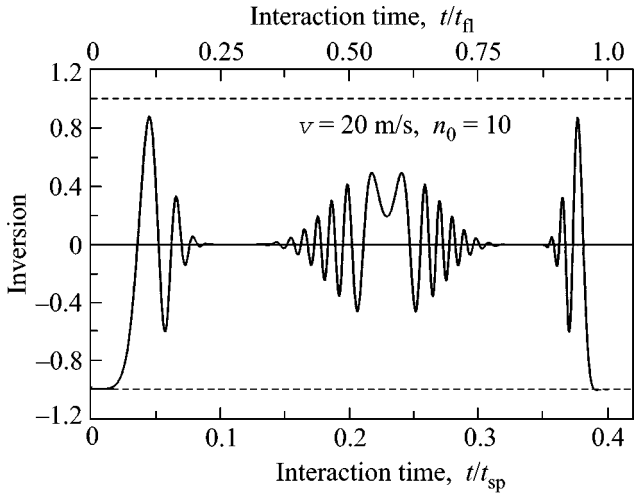

Fig. 2. Time evolution of the inverse population of an atom passing with the velocity $v = 20$ m/s through the cavity with the average number of photons $\langle n_0 \rangle = 10$ before the atom enters the cavity. The lower time scale is in units of spontaneous lifetime τ_{sp} of the excited atomic state. The upper time scale is in units of atomic time of flight through the cavity.

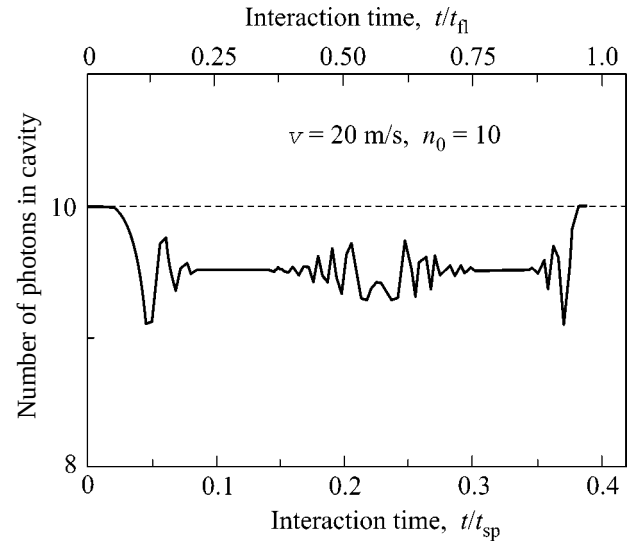

Fig. 3. The same as in Fig. 2, but for the average number of photons in the cavity.

If the cavity-field mode (without atom) is prepared in the coherent state, the coefficients $|c_n(0)|^2$ in expression (6) are specified by the Poisson distribution

$$|c_n(0)|^2 = \frac{\langle n_0 \rangle^n e^{-\langle n_0 \rangle}}{n!}, \tag{8}$$

where the average number $\langle n_0 \rangle$ of photons in the cavity mode in the absence of an atom is determined by the external laser radiation.

The field and atom exchange energy in the cavity mode. The inverse population of the atom is determined by the expression

$$w(t) = \sum_{n=0}^{\infty} [|c_{e,n}(t)|^2 - |c_{g,n}(t)|^2]. \tag{9}$$

Figures 2 and 3 illustrate the time evolution of the inverse population of atomic levels and the average number of photons in the cavity mode, respectively, when the atom passes with the velocity $v = 20$ m/s through the cavity with a comparatively large number of photons $\langle n_0 \rangle = 10$. The complex temporal dynamics of cavity-field mode and inverse population are explained by the fact that the Rabi frequency depends on the number n of photons. This dynamics lead to the well-known collapse effect and to restoring the inverse population of the atomic levels [16, 17], which is clearly demonstrated in Fig. 2, where the effect of atomic interaction time at a relatively low atomic velocity is seen. The presence of an atom changes the cavity properties. The transmittance T and, therefore, reflectance R of the cavity become time-dependent [13]:

$$T(t) = \left|\frac{X(t)}{Y}\right|^2, \tag{10}$$

where $X(t)$ is the amplitude of cavity-field mode and Y is the amplitude of the pumping laser field. In the atom nanoprobe scheme under consideration, information about the atom is carried by the radiation reflected from the cavity, which depends on the atomic and cavity parameters as

$$|Y_{refl}(t)|^2 = \left(1 - \pi\frac{\langle n(t) \rangle}{n_{ph} VF}\right) n_{ph} cS, \tag{11}$$

where the average number $\langle n(t) \rangle$ of photons in the cavity mode is given by Eq. (7), n_{ph} is the average number of photons in the cavity before the atom enters it, V is the cavity-mode volume, S is the mode cross section, F is the cavity finesse, and c is the speed of light.

Figure 4 shows the time dependence of the photon flux reflected from the cavity containing one photon ($\langle n_0 \rangle = 1$), having finesse $F = 5 \times 10^5$, and through which the atom passes with velocities $v = 20$, 50, and 100 m/s. The oscillatory behavior of the reflected photon flux is caused by the fast energy exchange between the atom and the cavity field. Figure 5 shows the time dependence of the integral signal

$$N_{refl} = \int_0^t |Y_{refl}(t)|^2 dt \tag{12}$$

of reflected photons for atomic velocities $v = 20$, 50, and 100 m/s and $\langle n_0 \rangle = 1$. As is seen, the number of reflected photons reaches 5 even for a sufficiently high atomic velocity of 100 m/s. In this case, the detection time is $t_{det} = -0.08\tau_{sp}$.

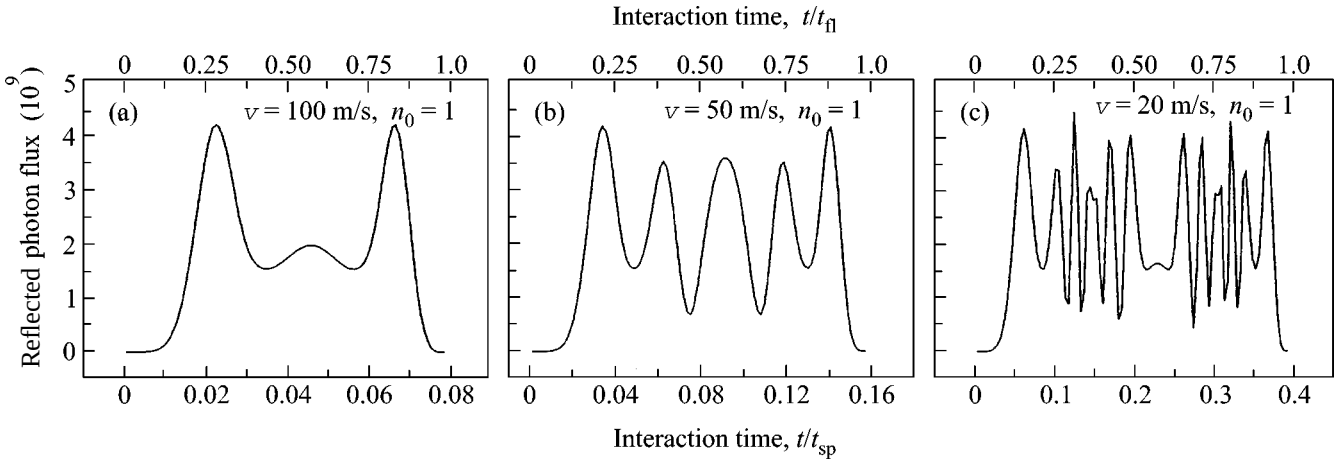

Fig. 4. Time dependence of the photon flux reflected from the cavity containing one photon on average ($\langle n_0 \rangle = 1$) and through which the atom passes with the velocities v = (a) 100, (b) 50, and (c) 20 m/s.

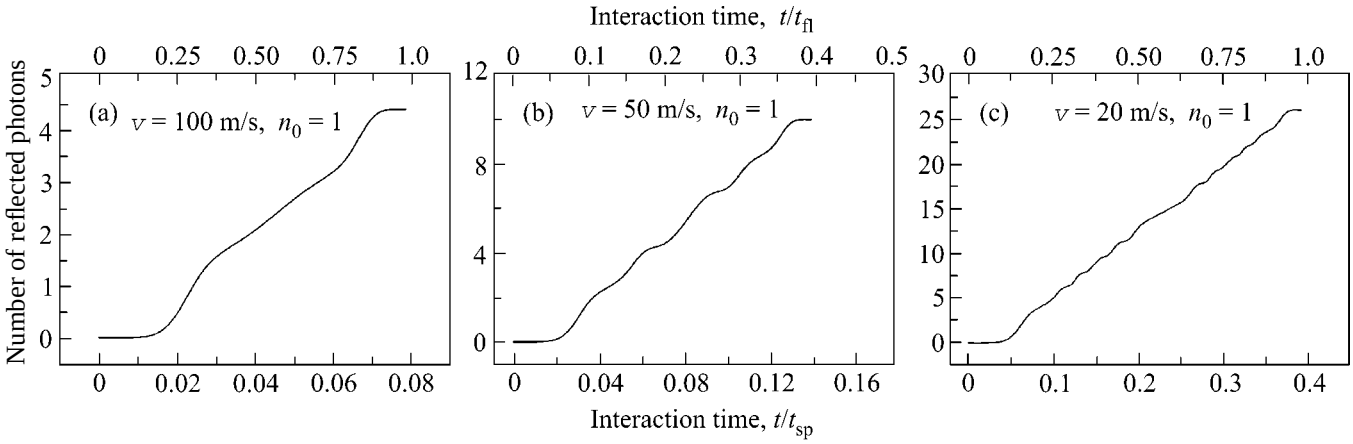

Fig. 5. The same as in Fig. 4, but for the number of photons reflected from the cavity.

In conclusion, we discuss the possibility of practical realization of the atom nanoprobe discussed above. To estimate the effect of a small hole on the cavity Q factor, we use the calculations of radiation transmittance through a screen with a small hole [12, 15, 18]. Transmittance through a hole for the black screen (which is maximal compared to other screen types) is [18]

$$T_{tr} \simeq \left(\frac{1}{8\pi^2}\right)[1 + \tau_2(ka)^2 + \ldots], \qquad (13)$$

where $\tau_2 = 11.07$. Transmittance through a small hole ($ka \ll 1$) is independent of the hole size and is $T_{tr} \approx 1/8\pi^2$. Power passing through the hole is determined by the ratio of the hole size a to the cavity-mode size ω_0:

$$P_{tr} = P_{in}\frac{a^2}{w_0^2}T_{tr}, \qquad (14)$$

where P_{in} is the laser radiation power incident on the screen. Therefore, the transmittance of a mirror with a hole is

$$T = P_{tr}/P_{in} = T_{tr}(a^2/w_0^2). \qquad (15)$$

The corresponding cavity finesse is determined by the expression

$$F = \frac{\pi\sqrt{R}}{1-R} \simeq \frac{\pi}{T} = 8\pi^2\frac{w_0^2}{a^2}. \qquad (16)$$

For the cavity-mode radius $\omega_0 = 10\lambda$ and $a = 0.1\lambda$, the cavity finesse is no worse than $F = 8 \times 10^5$, which corresponds to the Q factor of the best available cavities [4, 5]. Thus, a small hole does not change noticeably the cavity Q factor in the atom nanoprobe.

The production of a nanometer hole in the cavity mirror is a difficult problem. The atom nanoprobe scheme based on a three-mirror cavity can be more efficient. A metallic foil having a small hole parallel to one

of the cavity mirrors and located at a distance of half-wavelength from the mirror can serve as the third mirror. In this scheme, the size of the light field interacting with the atom is determined by the distance between the foil and the cavity mirror. A small size of the cavity ensures a large coupling constant $g \gg \gamma_{sp}$. The requirements on the Q factor of the basic cavity are not too stringent in the three-mirror scheme. The total finesse of a three-mirror cavity [19] for the same reflectances of all mirrors is

$$F^* \cong \frac{2\pi(1-R)\sqrt{R}}{(1-R)^2} \tag{17}$$

and can be high even for moderate mirror reflectances. In particular, $F = 1.2 \times 10^5$ for $R = 0.99$. The use of metallic foil with the reflectance $R \simeq 0.96$–0.98 would make it possible to achieve the required total finesse of the composite cavity ($g_0 \gg \kappa$) and, therefore, to realize the necessary condition for a noticeable reflection from the cavity.

I am grateful to V.P. Yakovlev, V.G. Minogin, and F. Shimizu for stimulating discussions. This work was supported by the Russian Foundation for Basic Research (project nos. 02-17014, 02-16337a), the INTAS (grant no. INFO-00-479), and the Ministry of Education, Culture, Sport, Science, and Technology of Japan.

REFERENCES

1. W. Heisenberg, Z. Phys. **43**, 172 (1927); W. Heisenberg, *Die Physikalischen Prinzipien der Quanten Theorie* (Hirzel, Leipzig, 1930), p. 15.
2. J. von Neumann, *Matematische Grundlagen der Quanten Mechanik* (Springer, Berlin, 1932; Princeton Univ. Press, Princeton, N.J., 1955; Nauka, Moscow, 1964).
3. *Cavity Quantum Electrodynamics*, Ed. by P. R. Berman (Academic, Boston, 1994).
4. C. J. Hood, T. W. Lynn, A. C. Doherty, *et al.*, Science **287**, 1447 (2000); J. Ye, W. Vernooy, and H. J. Kimble, Phys. Rev. Lett. **83**, 4987 (1999).
5. P. W. H. Pinkse, T. Fischer, P. Maunz, and G. Rempe, Nature **404**, 365 (2000); P. Münstermann, T. Fischer, R. Maunz, *et al.*, Phys. Rev. Lett. **82**, 3791 (1999).
6. M. J. Holland, D. F. Walls, and P. Zoller, Phys. Rev. Lett. **67**, 1716 (1991).
7. M. Marte and P. Zoller, Appl. Phys. **54**, 477 (1992).
8. J. Gardner, M. L. Marable, G. R. Welch, and J. E. Thomas, Phys. Rev. Lett. **70**, 3404 (1993).
9. G. Rempe, Appl. Phys. B: Lasers Opt. **60**, 233 (1995).
10. A. M. Herkommer, H. J. Carmichael, and W. P. Schleich, Quantum Semiclassic. Opt. **8**, 189 (1996).
11. Young-Tak Chough, Sun-Hyun Youn, Hyunchul Nha, *et al.*, Phys. Rev. A **65**, 023810 (2002).
12. N. A. Bethe, Phys. Rev. **66**, 163 (1944).
13. Changxin Wang and Reeta Vyas, Phys. Rev. A **55**, 823 (1997).
14. H.-I. Yoo and J. H. Eberly, Phys. Rep. **118**, 24 (1985).
15. V. V. Klimov and V. S. Letokhov, Opt. Commun. **106**, 154 (1994); V. I. Balykin, V. V. Klimov, and B. S. Letokhov, Pis'ma Zh. Éksp. Teor. Fiz. **59**, 219 (1994) [JETP Lett. **59**, 235 (1994)].
16. J. H. Eberly, N. B. Narozhny, and J. J. Sanches-Moudragon, Phys. Rev. Lett. **44**, 1323 (1980).
17. G. Rempe and G. Walther, Phys. Rev. Lett. **58**, 353 (1987).
18. E. W. Marchang and E. Wolf, J. Opt. Soc. Am. **60**, 1501 (1970).
19. M. Born and E. Wolf, *Principles of Optics*, 4th ed. (Pergamon Press, Oxford, 1969; Nauka, Moscow, 1973).

Translated by R. Tyapaev

JETP Letters, Vol. 78, No. 6, 2003, pp. 413–420. Translated from Pis'ma v Zhurnal Éksperimental'noĭ i Teoreticheskoĭ Fiziki, Vol. 78, No. 6, 2003, pp. 865–873.
Original Russian Text Copyright © 2003 by Al'tshuler, Bresler.

Electron Paramagnetic Resonance in Kondo Insulators

T. S. Al'tshuler* and M. S. Bresler**

* *Zavoiskii Physicotechnical Institute, Russian Academy of Sciences, Kazan, 420061 Russia*

** *Ioffe Physicotechnical Institute, Russian Academy of Sciences, St. Petersburg, 194021 Russia*

Received August 18, 2003

This review is devoted to the application of electron paramagnetic resonance (EPR) in the study of fluctuating-valence materials, which are characterized by a narrow gap in the electron energy spectrum (Kondo insulators or Kondo semiconductors). The authors' papers on studying classical objects of this field of solid-state physics, SmB_6 and YbB_{12}, are considered as an illustration of the potentiality of the EPR method. Temperature dependences of the gap width in these materials were obtained, the static and dynamic Jahn–Teller effects on Sm^{3+} ions in SmB_6 were detected, and the formation of Yb^{3+} ion pairs and the spontaneous breaking of cubic symmetry in YbB_{12} were observed. The results obtained indicate that preference should be given to the exciton–polaron model developed by Kikoin *et al.* for the ground state of Kondo insulators. © *2003 MAIK "Nauka/Interperiodica".*

PACS numbers: 75.30.Mb; 76.30.-v

1. Introduction. Electron paramagnetic resonance (EPR) is a very informative and highly sensitive method of studying spin correlations in solid state. Therefore, it was natural to turn to this technique in studying materials with a fluctuating valence, so-called Kondo insulators, in which electron correlations—in particular, spin-dependent ones—play a decisive role.

Kondo insulators with a narrow gap in the energy spectrum (Kondo semiconductors) have been drawing researchers' attention for several decades due the properties of their ground state, which at low temperatures is a coherent, that is, macroscopic quantum state. Rare-earth ions in Kondo insulators exhibit a nonintegral valence due to its fluctuations with a frequency of 10^{12}–10^{13} Hz between the states $M^{2+} \longleftrightarrow M^{3+}$, where the M^{3+} state is magnetic (in thulium compounds, the valence fluctuates between two magnetic states $M^{3+} \longleftrightarrow M^{4+}$).

The best known compounds of this class are samarium hexaboride SmB_6 (with a mean valence of samarium of 2.6), ytterbium dodecaboride YbB_{12} (with a mean valence of ytterbium of 2.9), and the golden phase of samarium sulfide SmS (with a mean valence of samarium of 2.6). SmB_6 is a classical object of investigations; YbB_{12} is considerably less understood; and the golden phase of SmS is still less understood, apparently because of the difficulties of obtaining it. All these materials form crystals with a cubic structure. Samarium hexaboride has the CsCl-type lattice constructed of samarium ions and boron octahedra connected to each other with homopolar bonds into a firm skeleton, whereas ytterbium dodecaboride is crystallized in the NaCl-type structure in which ytterbium ions and boron cuboctahedra alternate. More recently, studies of numerous cerium-based Kondo insulators (CeNiSn, CeRhSb, etc.) have been started.

At present, the nature of the ground state of Kondo insulators cannot be considered to be completely understood. Therefore, it is useful to apply the whole variety of known experimental methods to its investigation. Among these, magnetic spectroscopy techniques, particularly EPR, turned out to be very informative. In this review, the potentialities of EPR in solving the problems of the ground state of Kondo insulators, as well as their interesting properties discovered with the use of EPR in the last six years, are demonstrated by the examples of SmB_6 and YbB_{12}.

The valence in Kondo insulators fluctuates with a frequency of 10^{12}–10^{13} Hz; transitions between the magnetic and nonmagnetic states of the system proceed with the same frequency. Because the frequency of an EPR spectrometer (10^{10} Hz) is significantly lower than the fluctuation frequency of the magnetic moment, the EPR signal on these rare-earth ions cannot be observed. Therefore, EPR in Kondo insulators is commonly studied by the spin marker technique, by introducing paramagnetic ions with a stable valence (Gd^{3+}, Eu^{2+}, Er^{3+}, etc.) into the crystal lattice. The observation of EPR on these ions allows one to determine their g factor and line width; to study the dependence of these parameters on temperature, dopant concentrations, and other factors; and to judge the properties of the matrix into which spin markers were doped, that is, the properties of the Kondo insulator. In general, it is not necessary to introduce a paramagnetic impurity. We managed to observe EPR signals on crystal-lattice samarium Sm^{3+} ions in SmB_6 [1] and ytterbium Yb^{3+} ions in YbB_{12} [2]. Any crystal, even the most perfect one, always contains

0021-3640/03/7806-0413$24.00 © 2003 MAIK "Nauka/Interperiodica"

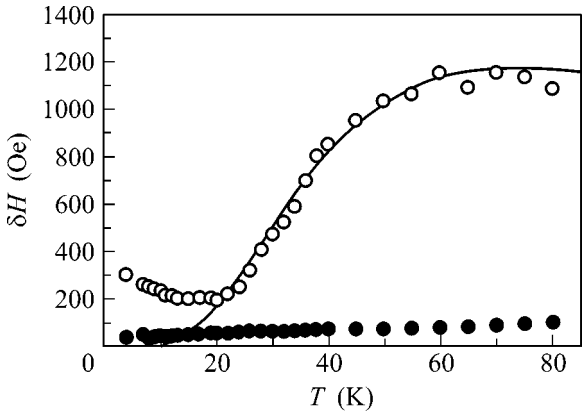

Fig. 1. Temperature dependence of the line width of EPR on the gadolinium Gd^{3+} ions in (○) YbB_{12} and (●) LuB_{12}. The concentration of Gd^{3+} ions is 1 at. %. Theoretical calculations are shown by the solid line.

defects or an uncontrolled impurity, which stabilizes the valence of some of the lattice ions [3].

2. On the nature of the energy gap. The nature of the energy gap in Kondo insulators was one of the problems in studying these materials that was solved by the EPR method. As a result of intensive studies by various methods, including EPR [4–6], it was found that samarium hexaboride SmB_6 [7–10] and ytterbium dodecaboride YbB_{12} [11–14] are fluctuating-valence compounds with an energy gap of 10–25 meV at low temperatures. However, while the fact that a narrow gap exists in Kondo insulators is beyond doubt, the question of its nature, or, fundamentally, the question of the ground state of Kondo insulators, remains debatable. Various theories were proposed to account for the origin of the gap. The gap was related to *df* hybridization [15], Wigner crystallization [16], and excitonic coupling of *d* electrons with *f* holes [17]. There is a substantial discrepancy between theoretical results at finite temperatures. Thus, the hybridization gap does not vary with temperature, and the excitonic gap arises as a collective effect and disappears at temperatures on the order of the gap itself.

Experimental data that point to the disappearance of the gap at high temperatures, that is, to the collective nature of the gap, were first obtained in [6, 18] in studying SmB_6. Recently, the same measurements were carried out for another classical object of the physics of Kondo insulators, YbB_{12} [19].

The measurements were performed in SmB_6 powders containing paramagnetic gadolinium Gd^{3+}, europium Eu^{2+}, and erbium Er^{3+} ions with various concentrations and in YbB_{12} samples doped with Gd^{3+} ions. For comparison, LaB_6 and LuB_{12} powders containing Gd^{3+} ions were also prepared. The investigations were carried out in the temperature range 1.7–150 K for SmB_6 and 1.7–80 K for YbB_{12} at the frequency ν = 9.4 GHz.

Gd^{3+} ions exhibit purely spin magnetism (the ground state is $4f^7$, $^8S_{7/2}$); therefore, their *g* factor is close to 2.00 and, because of long relaxation times, the EPR signal can be seen up to relatively high temperatures (see Fig. 1).

The measurements showed that there are more similarities between the temperature dependences of the EPR line width for rare-earth ions in SmB_6 and YbB_{12} Kondo insulators than between the corresponding characteristics in hexaborides (SmB_6 and LaB_6) and dodecaborides (YbB_{12} and LuB_{12}). The shape of $\delta H(T)$ in lanthanum and lutetium borides is linear, which is characteristic of metals, and is determined by the Korringa relaxation mechanism. The temperature dependence of the line width in Kondo insulators (samarium and ytterbium borides) demonstrates completely different behavior. From the viewpoint of studying the ground state of Kondo insulators, the behavior of the EPR signal at $T > 15$–20 K, where the resonance line is broadening almost exponentially with increasing temperature and then goes to saturation, seems to be most interesting. This behavior is caused by the existence of a gap in the spectrum of electronic excitations of these semiconductors. However, calculations in the model of *f–d* hybridization with a constant gap did not lead to a satisfactory description of $\delta H(T)$. At the same time, the behavior of $\delta H(T)$ somewhat resembled the behavior of the line width in superconductors; there were also theoretical arguments in favor of the collective nature of the gap in SmB_6 [17].

To interpret the results, a specific model, namely, the model of an excitonic insulator with large-radius (Mott–Wannier) excitons composed of a *d* electron and an *f* hole was assumed for the origination of the gap in [18]. In general terms, the Khaliullin–Khomskiĭ calculations followed the model of electron pair correlations in superconductors. It is natural that, as in the theory of superconductivity, a temperature-dependent gap in the spectrum of an excitonic insulator arises in this model. A comparison with the experiment allows one to determine this dependence. For the spin relaxation rate, the following equation was obtained:

$$\begin{aligned} T_2^{-1} &= 2\pi T f(\Delta)(b_d^2 + b_f^2) \\ &\times \{1 + \alpha[1 - f(\Delta)](\Delta/2T)\ln 2\Delta\tau\}, \\ f(\Delta) &= [1 + \exp(\Delta/T)]^{-1}, \quad b_i = J_i N_i, \\ \alpha &= (b_d + b_f)^2/(b_d^2 + b_f^2), \end{aligned} \tag{1}$$

where $\Delta = \Delta(T)$ is the excitonic gap, J_d and J_f are the exchange integrals of the interaction of Gd with a *d* electron and an *f* hole, N_d and N_f are the densities of states of the corresponding bands at the Fermi level, τ is the momentum relaxation time (correlation decay time). Good agreement with the experiment was

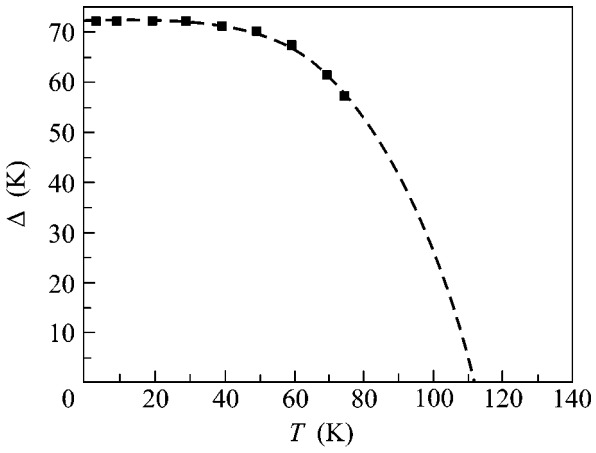

Fig. 2. Temperature dependence of the energy gap $\Delta(T)$ in YbB_{12}.

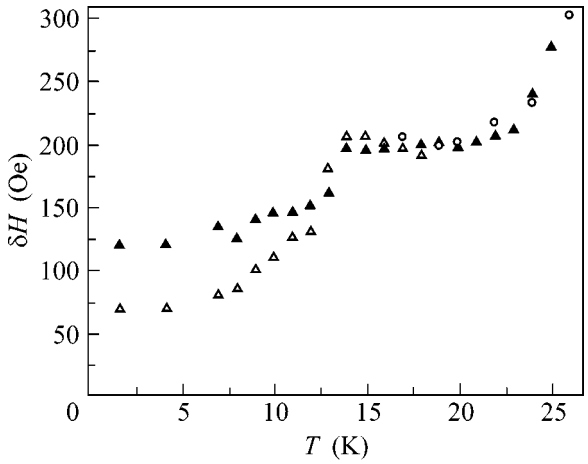

Fig. 3. Temperature dependence of the line width of EPR on the Gd^{3+} ions in YbB_{12}. The concentrations of Gd^{3+} ions are (△) 0.1 at. %, (▲) 0.5 at. %, and (○) 1 at. %.

obtained, and quite reasonable values were found for the parameters (J_d, J_f, N_d, and N_f) and for the shift of the g factor Δg. The gap at low temperatures in SmB_6 equals $2\Delta = 100$ K and remains almost constant up to 50–70 K, then it starts to decrease sharply and disappears at 150 K. The gap in YbB_{12} at low temperatures equals $2\Delta = 140$ K, it remains almost constant up to 40 K and disappears at 115 K (see Fig. 2). The magnitude of the gap is close to the critical temperature $T_c \approx$ 115 K in agreement with theoretical expectations.

Beginning in the mid-1980s, the model of an excitonic insulator has been advantageously developed by Kikoin and Mishchenko [20, 21] for the description of the ground state of a Kondo insulator with a fluctuating valence. As a result, an exciton–polaron model has emerged that is based on the idea that the ground state of the system represents a superposition of an f^6 state and an f^5p state. The f^6 state corresponds to a Sm^{2+} ion, and the f^5p state corresponds to an intermediate-coupling exciton in which the hole belongs to the f shell of the samarium ion (Sm^{3+}) and the electron occupies an orbital that represents a linear combination of p states of the boron atoms surrounding the samarium ion (in the first coordination sphere). As a whole, this combination has the same symmetry as the hole state. The exciton resides in the singlet (that is, nonmagnetic) state. Valence fluctuations can be described as quantum beating between the two configurations of the system described above. Correlation in the states of excitons at different sites is due to the exchange interaction of excitons, which is absent in the mean-field approximation. Thus, a macroscopically coherent state forms. The gap in the electronic spectrum in the Kikoin–Mishchenko model appears as a result of the renormalization of the purely hybridization gap through the Coulomb interaction of electrons and holes, which leads to the appearance of excitons.

The exciton–polaron model allowed its authors to explain the anomalies in the phonon spectrum [20] and the dispersion of magnetic excitations [22] studied by inelastic neutron scattering, as well as the optical absorption and dispersion in the submillimeter range [23] in SmB_6 (also see the studies of transport properties [24, 25]). Unfortunately, the spin relaxation rate in a Kondo insulator was not calculated in the Kikoin–Mishchenko model; therefore, in our work [19], we again had to use the Khaliullin–Khomskiĭ theory in order to interpret the experimental results. Based on good agreement with the experiment, it may be suggested that the difference between the effects of the intermediate-coupling excitons and the Mott–Wannier excitons on the relaxation rate T_2^{-1} of the Gd^{3+} spins introduces no crucial changes in the comparison between the theory and the experiment. Emphasize that it was already noted in [18] that the experimental dependence is only slightly sensitive to the preexponential factor in Eq. (1). The essential feature required for the achievement of agreement between the theory and the experiment was the introduction of a temperature-dependent gap.

At low temperatures, a characteristic kink is observed in the temperature dependence of the EPR line width for all levels of doping YbB_{12} samples with gadolinium (Fig. 3) [19]. It is interesting to note that we also observed a similar kink in SmB_6 at the same temperatures. It was also independent of the concentration of the impurity [18]. Apparently, the increase in the line width at a temperature of 13–14 K is associated with the properties of the ground state of the system, for example, with the formation of a bound polaron whose existence was considered in the paper by Curnoe and Kikoin [21]. The states inside the energy gap in SmB_6 were observed in [25]. Their origination is related in this work with correlation between exciton–polaron

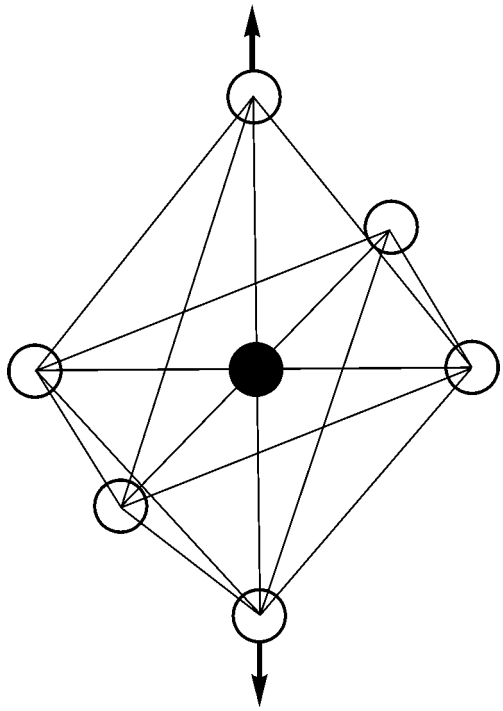

Fig. 4. Deformation of a cluster of fluctuating samarium ions surrounding a paramagnetic ion with a stabilized valence (Sm^{3+}) in the case of the Jahn–Teller effect in SmB_6. There are three types of distorted clusters corresponding to displacements along the *x*, *y*, and *z* axes.

complexes arising at various lattice sites. Magnetic excitations with energies lying inside the energy gap of SmB_6 were also observed in this Kondo insulator in [26]. These states were assigned to the interaction of the ground state of the Sm^{3+} ion with mixed phonon modes and valence fluctuations (Jahn–Teller effect).

3. The Jahn–Teller effect on SmB_6 ions in samarium hexaboride. It is known that the Jahn–Teller effect consists of spontaneous breaking of the symmetry of a high-symmetry configuration of a molecule or a cluster (in solid state). This leads to splitting of the degenerate state and to a decrease in the energy of the system. A cluster, in this case, means a particular ion and its nearest surroundings—most frequently the ions of the first coordination sphere whose displacement just leads to the breaking of symmetry. This breaking is due to the interaction of the ion in a degenerate state with the eigenmodes of the cluster atoms whose symmetry is lower than the symmetry of the identical representation (totally symmetric mode).

However, it was commonly assumed that the Jahn–Teller effect could not be observed in EPR of rare-earth ions [27]. The reason for this statement was the opinion that the symmetric configuration is stabilized in rare-earth ions because of strong spin–orbit interaction. Therefore, the observation of the dynamic Jahn–Teller effect in SmB_6 by a group of physicists from the Darmstadt Technical University was a complete surprise; this effect was not observed in materials with stable valences like BaB_6, CaB_6, and YbB_6 [28].

Recall what the static and dynamic Jahn–Teller effects are. The Jahn–Teller effect in SmB_6 consists of a spontaneous deformation of the octahedron (cluster) composed of the fluctuating Sm ions surrounding the spin marker, which was in a degenerate state before the rise of the deformation (Fig. 4). The spin markers were the Er^{3+} ion in [28, 29], the Gd^{3+} ion in [30], and the Sm^{3+} ion in our work [1]. The boron atoms form a firm skeleton bound by covalent bonds and do not participate in the Jahn–Teller effect. The deformation of the octahedron represents compression (or extension) along one of the principal cubic axes, which results in the splitting of the symmetric quartet state Γ_8 of the trivalent ion into two doublets Γ_6 (or Γ_7) with parameters determined by the parameters of the starting quartet. The states corresponding to deformations along the *x*, *y*, and *z* axes are degenerate; therefore, anisotropic doublets of three types must be observed in the EPR spectrum at low temperatures. The degenerate states are separated from each other by potential barriers, which hinder the free rearrangement of the cluster at low temperatures from configuration *x* to configuration *y* or *z*. This spontaneous breaking of symmetry is called the static Jahn–Teller effect. With increasing temperature, the oscillations of the metal ions near their new (displaced) equilibrium positions become stronger, and the system that consists of the paramagnetic ion and its distorted environment starts to tunnel between the states corresponding to deformations along the different cubic axes. The sixfold degenerate vibronic state (three equivalent doublets) is split upon tunneling into the quartet Γ_8 (with parameters that, generally speaking, differ from those of the starting quartet) and the doublet Γ_6 (or Γ_7). The experiment shows that the quartet state lies below the doublet state and is separated from it. This phenomenon averaging the previous doublet states is referred to as the dynamic Jahn–Teller effect. The quartet state Γ_8 of the Er^{3+} ion was observed in [28] with parameters that were considerably less anisotropic than could be expected, which was interpreted as a manifestation of the dynamic Jahn–Teller effect. The observation of the dynamic Jahn–Teller effect in [28, 30] was a remarkable result; however, a certain dissatisfaction remained associated with the fact that the static Jahn–Teller effect, which must predominate at low temperatures, was not observed. This puzzle was resolved in [1], in which we managed to observe both the static and the dynamic Jahn–Teller effects on Sm^{3+} ions.

The measurements of EPR were performed in the *X* range of frequencies (10^{10} Hz) at $T = 1.6$–4.2 K. Pure single crystals of samarium hexaboride and crystals doped with rare-earth paramagnetic impurities of different valences (Gd^{3+}, Er^{3+}, and Eu^{2+}) with concentra-

tions $c \sim 0.01$–0.05 at. % were used. EPR signals were observed for both the paramagnetic impurities and trivalent samarium ions.

All the lines were narrow, which provided indirect evidence of the high quality of the crystals. However, even such a crystal contains defects. These defects were the reason for the transformation of some ($c \sim 0.04$ at. %) of the fluctuating samarium ions to the stable trivalent state. The stabilization of the valence of samarium Sm^{3+} in doped crystals ($c \sim 0.1$ at. %) is also due to the introduced impurity.

Depending on the direction of the magnetic field with respect to the crystal axes in the (100) plane, three lines *E*, *F*, and *G* (Fig. 5) from the doublets Γ_{6x}, Γ_{6y}, and Γ_{6z} were observed in all the studied crystals at the temperature $T = 1.6$ K. Apart from these lines, two more lines from the quartet Γ_8 (*A* and *B* in Fig. 5) are seen in the pure SmB_6 crystal and in the crystal doped with bivalent europium. The remaining positions of the quartet lines are shown in the figure in a dashed line. Transition *C* is forbidden or semiforbidden at all the angles θ. Transition *D* was outside the available region of magnetic fields (more than 16 kOe). For the same reason, it was possible to observe transition *A* only in a narrow region of angles θ (from 30° to 60°) between the direction of the magnetic field and the [100] crystal axis.

An analysis of the parameters of the EPR spectrum showed that the doublet states (corresponding to the static Jahn–Teller effect) originate from the quartet states (described by the dynamic Jahn–Teller effect), which are split by the deformation.

The ratio of intensities of the quarter I_4 and the doublet I_2 transitions (the most intense lines were chosen) is proportional to the statistical weights of quartets I_4 and doublets I_2 and to the probability of the tunnel transition between the doublet states separated by the potential barrier E_b

$$I_4/I_2 \sim (N_4/N_2)\exp(-E_b/kT). \quad (2)$$

The experiment showed that the relative amount of quartets with respect to doublets increases with increasing temperature up to 4.2 K, as should be expected under conditions of the Jahn–Teller effect. The height of the barrier between the deformation wells separating the doublet states can be estimated from the variation of the ratio of concentrations of quartets and doublets N_4/N_2 with temperature. It was found to be approximately 2 K. The ratio N_4/N_2 and the barrier height only slightly differed in the cases of the doped and undoped samples. This indicates that the observed phenomena are correctly explained by the Jahn–Teller mechanism rather than random deformations for which the number of doublets and quartets in different crystals could differ rather strongly.

The interpretation of the results in the paper [28] and in the dissertation [29] was based on the conventional theory of the Jahn–Teller effect, which takes into account the interaction of the trivalent ion with cluster vibrations. A somewhat different mechanism of the dynamic Jahn–Teller effect observed in [28] was considered in [31]. The mechanism in [31] was based on the effect of valence fluctuations on the symmetric state of the ion. However, because the static Jahn–Teller effect arises only in the conventional theory presented in [29], it was this theory that we used for the description of our results.

When a trivalent ion interacts with cluster vibrations, these modes become coupled because the frequencies of the lattice vibrations and the valence fluctuations are close to each other. At the same time, the force constants responsible for lattice vibrations become softer [20]. It is this mode softening that is apparently the main reason for the occurrence of the Jahn–Teller effect in SmB_6 and its absence in stable-valence materials. Because the model in [29] was con-

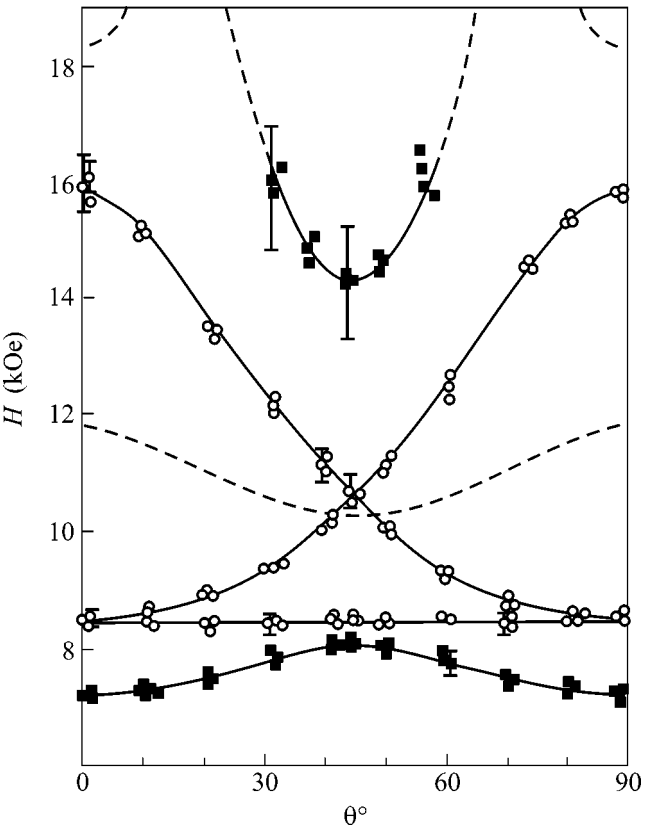

Fig. 5. Angular dependence of the resonance line positions for the Sm^{3+} ion in a SmB_6 single crystal with respect to a rotation of the magnetic field in the (100) plane. $T = 1.6$ K. Experimental line positions are designated by black squares for undoped SmB_6, black circles for SmB_6 doped with Eu^{2+}, and triangles and light circles for SmB_6 doped with Gd^{3+} and Er^{3+}, respectively. Lines *A*, *B*, *C*, and *D* are the line positions theoretically calculated for the Γ_8 quartet; lines *E*, *F*, and *G* are the line positions theoretically calculated for the Γ_x, Γ_y, and Γ_z doublets.

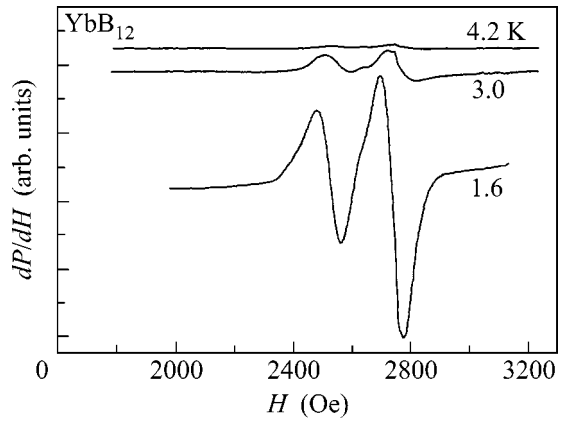

Fig. 6. EPR spectrum in an YbB_{12} single crystal at various temperatures for the magnetic field directed along the [001] axis in the (110) plane.

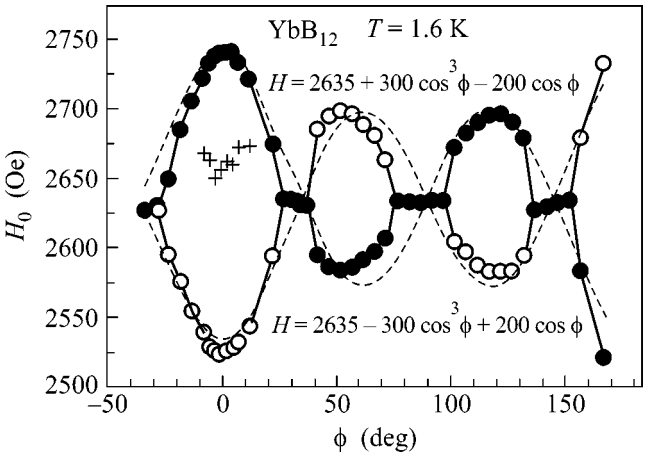

Fig. 7. Angular dependence of the resonance line positions in a YbB_{12} single crystal with respect to a rotation of the magnetic field in the (110) plane. $T = 1.6$ K. Black and white circles indicate the positions of the extreme spectral lines (pairs), crosses indicate the position of the weak isotropic line related to the Γ_6 doublet. Theoretical calculations are shown in dashed lines.

structed by the invariant method with regard to only the symmetry of the normal cluster vibrations, we believe that it is not actually related to the conventional lattice vibrations but is also valid in the case of mixed lattice–electronic modes. From the viewpoint of the exciton–polaron model, the manifestation of the Jahn–Teller effect can be interpreted as the existence of "spin polarons," that is, spin states of an impurity ion dressed with a cloud of mixed exciton–polaron excitations of the matrix. In more common terms of the Jahn–Teller effect, these are vibronic states of the cluster at whose center a Sm^{3+} ion is located.

The results of EPR studies that we carried out on the Er^{3+} and Gd^{3+} ions coincided with those reported in [28, 30]; that is, the EPR spectra of these ions are described by the dynamic Jahn–Teller effect. On the Sm^{3+} ions in SmB_6 doped with trivalent ions, we observed the static Jahn–Teller effect, whereas both the static and dynamic Jahn–Teller effects were simultaneously observed on the Sm^{3+} ions in pure SmB_6 and in SmB_6 doped with bivalent europium. Thus, the EPR of the trivalent ions (Er^{3+}, Gd^{3+}, and Sm^{3+}) in SmB_6 can be described from a unified viewpoint if the Jahn–Teller effect is taken into account. At the same time, if bivalent Eu^{2+} ions are doped into SmB_6, the Jahn–Teller effect is not observed on these ions. The mean valence of the fluctuating Sm ion in SmB_6 equals +2.6; that is, it is closer to the valence of the Er^{3+} and Gd^{3+} ions than to that of the bivalent Eu^{2+}. However, it is the insertion of the erbium and gadolinium ions (and the appearance of Sm^{3+} ions) that perturbs the state of the lattice more strongly than the insertion of the Eu^{2+} ions with a larger ionic radius. As was shown in the excitonic model of a fluctuating-valence semiconductor (Kondo insulator), the fluctuating Sm ion retains an electron in the nearest coordination sphere even when the electron leaves the *f* shell, that is, when the formal valence of the samarium ion equals +3. Actually, a small-radius exciton is formed in this case, and its size can be close to the radius of an ion with a valence of +2. Thus, the excitonic model of a Kondo insulator explains the tendency of the ions with a valence of +3 to break the local symmetry of the lattice (Jahn–Teller effect), whereas the Eu^{2+} ion retains the cubic symmetry of the environment (that is, its unperturbed state).

Summing up the first two sections of the review, we may state that the results of the EPR studies described above provide convincing evidence in favor of the exciton–polaron model of a Kondo insulator.

4. Formation of pairs and the spontaneous breaking of cubic symmetry in YbB_{12}. For a long time, the properties of another classical representative of Kondo insulators, YbB_{12}, have been studied in polycrystalline samples. Only the synthesis of high-quality YbB_{12} crystals by the Japanese physicists Iga, Shimizu, and Takabatake [12] allowed EPR to be studied in a single crystal of this semiconductor. EPR signals on the Yb^{3+} ions in a specially undoped YbB_{12} single crystal were detected in [2] at temperatures of 1.6–4.2 K. It was inferred that, as in SmB_6, a certain concentration of ions with a stabilized valence of 3+ is present in the crystal. A comparison of the EPR signal in the YbB_{12} single crystal with a standard showed that the concentration of the Yb^{3+} ions reached approximately 0.3 at. %. The investigation of EPR in YbB_{12} revealed three unusual facts: (1) two closely spaced intense lines and a weak line between them were detected (Fig. 6) rather than the expected single line of the EPR signal (similar to the results [32, 33], the Yb^{3+} ion can occur in the Γ_6 doublet state); (2) whereas the Γ_6 doublet must give an

isotropic EPR signal (with respect to a rotation of the magnetic field in the (110) plane), the observed extreme EPR lines in fact exhibited a complicated angular dependence described by the third-order Legendre polynomial $Y_{30}(\cos\phi)$ (Fig. 7); only the weak central line gives an isotropic signal from the Γ_6 doublet; (3) because of relatively long relaxation times, the EPR spectra from the Yb^{3+} ion have been observed up to the temperature of liquid nitrogen (–77 K); the intensity of the EPR signal in YbB_{12} drops on heating from 1.6 to 4.2 K by almost two orders of magnitude, so it is hardly seen at liquid-helium temperature (Fig. 6).

An analysis of the results showed that intense lines arise from the splitting of a state with a *g* factor of approximately 2.6 and with a weak anisotropic interaction characteristic of the Γ_6 state. The splitting of a single line into two ones pointed to the existence of two similar interacting oscillators, that is, the existence of pairs of Yb^{3+} ions. However, the isotropic exchange interaction of two Sm^{3+} ions does not lead to the splitting of the frequencies of the triplet state of the ion pair [34]. At the same time, anisotropic exchange gives an angular dependence of the positions of resonance lines described by the first rather than the third Legendre polynomial. Therefore, the Hamiltonian that took into account the ion pair interaction

$$H = g\mu H_z T_z + (1/2)\Im\{T(T+1) - 3/2\} \qquad (3)$$

should be supplemented with the term

$$a(3T_{1z}T_{2z} - \mathbf{T}_1\mathbf{T}_2)(\mathbf{T}_2\mathbf{H}) - (3a/2)(\mathbf{T}_1\mathbf{T}_2)(\mathbf{T}_2\mathbf{H}), \quad (4)$$

which describes the experimental angular dependence. Here, $\mathbf{T} = \mathbf{S}_1 + \mathbf{S}_2$ is the total spin of the pair, and T_z is its *z* projection. The anisotropic part of interaction is thus associated with the dipole–dipole (the first term) and the exchange (the second term) pair interactions. Thus, the formation of ion pairs and a spontaneous breaking of cubic symmetry were found in a Kondo insulator: all the pairs were aligned in the same direction, as a result of which the cubic symmetry of the crystal lowered to the axial symmetry. The reasons for such a peculiar phase transition are unclear at present; it could be associated with both dipole–dipole ordering that resembles the emergence of nuclear ordering [35] or with the properties of the ground state of a Kondo insulator considered in the Kasuya model with Wigner crystallization [16].

A strong (close to exponential) temperature dependence of the EPR intensity was also observed in [2] (Fig. 6). At the same time, neither the behavior of the magnetic susceptibility nor the temperature-independent angular dependence of the resonance-line positions allows the conclusion that a magnetic or structural phase transition takes place in the studied temperature range. Therefore, the obtained temperature dependence of the EPR intensity should be assigned to a variation of the concentration of the EPR-active centers, that is, the concentration of the Yb^{3+} ions with a stabilized valence. The experimental data obtained can be explained by the liberation of electrons captured by traps with a binding energy of 12 K as the temperature increases; the liberated electrons compensate the charge of Yb^{3+} ions, transforming them into fluctuating-valence ions, which are inactive in EPR.

The results of the study of EPR in YbB_{12} are reported in more detail in [36].

5. Conclusions. The results obtained by the authors and described in this review demonstrate ample potentialities of the EPR technique in studying Kondo insulators—materials with strong electron correlations—especially in studying the most puzzling of their properties, namely, their ground state. Unfortunately, the papers on EPR in this area are small in number; as other examples, we indicate papers on studying cerium-based Kondo insulators [33, 37].

The results cited in this review were obtained within the projects supported by the Russian Foundation for Basic Research, project nos. 97-02-16235 and 00-02-16080. The writing of this review was also supported by the Russian Foundation for Basic Research, project no. 03-02-17453.

REFERENCES

1. T. S. Al'tshuler and M. S. Bresler, Zh. Éksp. Teor. Fiz. **115**, 1860 (1999) [JETP **88**, 1019 (1999)].
2. T. S. Al'tshuler, M. S. Bresler, Yu. V. Goryunov, *et al.*, Fiz. Tverd. Tela (St. Petersburg) **44**, 1469 (2002) [Phys. Solid State **44**, 1536 (2002)].
3. M. Kasaya, H. Kimura, Y. Isikawa, *et al.*, in *Valence Fluctuations in Solids*, Ed. by L. M. Falicov, W. Hanke, and M. B. Maple (North-Holland, Amsterdam, 1981), p. 251.
4. T. S. Al'tshuler, M. M. Zaripov, and V. N. Mironov, in *Abstracts of VII All-Union Symposium on Spectroscopy of Crystals Activated by Ions of Rare-Earth and Transition Metals* (Leningrad, 1982), p. 11.
5. C. M. Jackson, K. Y. M. Wong, M. Hardiman, *et al.*, Bull. Am. Phys. Soc. **28**, 270 (1983).
6. T. S. Al'tshuler, V. N. Mironov, G. G. Khaliullin, and D. I. Khomskiĭ, Pis'ma Zh. Éksp. Teor. Fiz. **40**, 28 (1984) [JETP Lett. **40**, 754 (1984)].
7. J. W. Allen, B. Batlogg, and P. Wachter, Phys. Rev. B **20**, 4807 (1979).
8. G. Guntherodt, W. A. Thompson, F. Holtzberg, and Z. Fisk, Phys. Rev. Lett. **49**, 1030 (1982).
9. I. Frankowski and P. Wachter, Solid State Commun. **41**, 885 (1982).
10. P. Travaglini and P. Wachter, Phys. Rev. B **29**, 893 (1984).
11. T. Takabatake, F. Iga, T. Yoshino, *et al.*, J. Magn. Magn. Mater. **177–181**, 277 (1998).
12. F. Iga, N. Shimizu, and T. Takabatake, J. Magn. Magn. Mater. **177–181**, 337 (1998).
13. F. Iga, S. Hiura, J. Klijn, *et al.*, Physica B (Amsterdam) **259–261**, 312 (1999).

14. H. Okamura, S. Kimura, H. Shinozaki, *et al.*, Phys. Rev. B **58**, R7496 (1998); H. Okamura, S. Kimura, H. Shinozaki, *et al.*, Physica B (Amsterdam) **259–261**, 317 (1999).
15. N. F. Mott, Philos. Mag. **30**, 403 (1984).
16. T. Kasuya, J. Phys. Soc. Jpn. **65**, 2548 (1996).
17. D. I. Khomskii, in *Quantum Theory of Solids*, Ed. by I. M. Lifshits (Mir, Moscow, 1982), p. 70.
18. T. S. Al'tshuler, G. G. Khaliullin, and D. I. Khomskiĭ, Zh. Éksp. Teor. Fiz. **90**, 2104 (1986) [Sov. Phys. JETP **63**, 1234 (1986)].
19. T. S. Al'tshuler, A. E. Al'tshuler, and M. S. Bresler, Zh. Éksp. Teor. Fiz. **120**, 127 (2001) [JETP **93**, 111 (2001)].
20. K. A. Kikoin and A. S. Mishchenko, Zh. Éksp. Teor. Fiz. **104**, 3810 (1993) [JETP **77**, 828 (1993)]; J. Phys.: Condens. Matter **7**, 307 (1995).
21. S. Curnoe and K. A. Kikoin, Phys. Rev. B **61**, 15714 (2000).
22. P. A. Alekseev, A. S. Ivanov, B. Dorner, *et al.*, Europhys. Lett. **10**, 457 (1989); P. A. Alekseev, J.-M. Mignot, J. Rossat-Mignot, *et al.*, J. Phys.: Condens. Matter **7**, 289 (1995).
23. N. Sluchanko, V. V. Glushkov, B. Gorshunov, *et al.*, Phys. Rev. B **61**, 9906 (2000).
24. B. Gorshunov, N. Sluchanko, A. Volkov, *et al.*, Phys. Rev. B **59**, 1808 (1999).
25. N. E. Sluchanko, A. A. Volkov, V. V. Glushkov, *et al.*, Zh. Éksp. Teor. Fiz. **115**, 970 (1999) [JETP **88**, 533 (1999)].
26. T. P. Nyhus, S. L. Cooper, Z. Fisk, and J. Sarrao, Phys. Rev. B **55**, 12488 (1997).
27. S. A. Al'tshuler and B. M. Kozyrev, *Electron Paramagnetic Resonance in Compounds of Transition Elements* (Nauka, Moscow, 1972; Halsted, New York, 1975), p. 97.
28. H. Sturm, B. Elschner, and K. H. Hoeck, Phys. Rev. Lett. **54**, 1291 (1985).
29. H. Sturm, Dissertation (Darmstadt, 1985).
30. G. Wiese, H. Schaeffer, and B. Elschner, Europhys. Lett. **11**, 791 (1990).
31. C. Weber, E. Sigmund, and M. Wagner, Phys. Rev. Lett. **55**, 1645 (1985).
32. W. Low and R. S. Rubins, Phys. Rev. **131**, 2527 (1963).
33. G. B. Martins, M. A. Pires, G. E. Barberis, *et al.*, Phys. Rev. B **50**, 14822 (1994).
34. A. Abragam and B. Bleaney, *Electron Paramagnetic Resonance of Transition Ions* (Clarendon Press, Oxford, 1970; Mir, Moscow, 1973).
35. A. Abragam and M. Goldman, *Nuclear Magnetism: Order and Disorder* (Clarendon Press, Oxford, 1982; Mir, Moscow, 1984).
36. T. S. Altshuler, Yu. V. Goryunov, M. S. Bresler, *et al.*, Phys. Rev. B **68**, 014425 (2003).
37. C. Mair, H. A. Krug von Nidda, M. Lohmann, and A. Loidl, Phys. Rev. B **60**, 16409 (1999).

Translated by A. Bagatur'yants

JETP Letters, Vol. 78, No. 6, 2003, p. 421.

ERRATA

Erratum: "Trapping of Plasmons in Ion Holes" [JETP Lett. 77 (12), 647 (2003)]

P. K. Shukla and B. Eliasson

PACS numbers: 52.35.Hr

Equation (6) should read

$$\tau\frac{\partial^2\phi}{\partial\xi^2} - \exp[\tau(\phi - W^2)] + b\exp\left(-\frac{M^2}{2}\right) \times\left\{I[-(\phi-\phi_{\max})] + K\left(\frac{M^2}{2}, -(\phi-\phi_{\max})\right) + \frac{2}{\sqrt{\pi|\alpha|}}W_D[\sqrt{\alpha(\phi-\phi_{\max})}]\right\} = 0. \quad (6)$$

Equation (7) should read

$$H(W, \phi, \lambda, M) = 3\left(\frac{\partial W}{\partial\xi}\right)^2 - \frac{\tau}{2}\left(\frac{\partial\phi}{\partial\xi}\right)^2 - (\lambda-1)W^2 + \frac{1}{\tau}\{\exp[\tau(\phi-W^2)]-1\} + b\exp\left(-\frac{M^2}{2}\right)\left[P(\phi_{\max}-\phi, \alpha) + h\left(\frac{M^2}{2}, 0, \phi_{\max}-\phi\right) - 1\right] - H_0 = 0. \quad (7)$$

On page 649, second column, second paragraph, the expression $3(d^2W/d\xi^2) + [1 - \exp(\phi) - \lambda]W = 0$ should be replaced by $3(d^2W/d\xi^2) + [1 - \exp(\tau\phi) - \lambda]W = 0$.

0021-3640/03/7806-0421$24.00 © 2003 MAIK "Nauka/Interperiodica"

JETP Letters, Vol. 78, No. 6, 2003, p. 422.

Erratum: “On the Depolarization of Ultracold Neutrons in Traps” [JETP Lett. 76 (3), 131 (2002)]

Yu. N. Pokotilovski

PACS numbers: 14.20.Dh; 13.88.+e; 25.40.Dn

The first of Eqs. (2) should read

$$\ddot{\phi} + (\omega^2 - ia + a^2 t^2)\phi = 0,$$

Equation (11) should be

$$|\phi(+\infty)|^2 \simeq \frac{9}{4}(\xi^2 + \xi'^2).$$

In Fig. 2, the legends for curves *1* and *2* correspond, respectively, to curves *3* and *4*, and vice versa. These misprints does not change the main result of the work: the probability of neutron depolarization in traps increases appreciably upon neutron reflection from the walls positioned in a nonuniform magnetic field.

0021-3640/03/7806-0422$24.00 © 2003 MAIK “Nauka/Interperiodica”